

# Dispersion Control of Surface Plasmons

## Dissertation

zur Erlangung des

**Doktorgrades der Naturwissenschaften**

**(Dr. rer. nat.)**

der

Naturwissenschaftlichen Fakultät II-

Chemie, Physik und Mathematik

der Martin-Luther-Universität Halle-Wittenberg

vorgelegt von

Frau Neha Sardana

geb. am 05 Juni 1986

**Gutachter:**

Prof. Dr. Joerg Schilling (Betreuer, Martin-Luther-Universität Halle-Wittenberg)

Prof. Dr. Georg Woltersdorf (Martin-Luther-Universität Halle-Wittenberg)

Prof. Dr. Markus Schmidt (Leibniz Institute of Photonic Technology, IPHT Jena)

**Tag der Verteidigung: 29.10.2015**



# Abstract

Over the past few decades, a new class of plasmonic metamaterials has arisen for its lucrative functionality. Even the traditional metals like gold and silver have been successfully tailored at the nanoscale to show large variations in optical response when compared to the bulk, hence leading to wide range of applications in sensing, non-linear optics, and imaging to name just a few.

It is known that the resonances of surface plasmons crucially depend on the permittivities of the metal and the dielectric, so, when the traditional noble metals gold or silver are combined with dielectrics of moderate refractive index, then these surface plasmon resonances usually appear within the visible spectral range. However, to use the plasmonic effects in conjunction with silicon photonics the frequency range of the surface plasmon resonances has to be shifted into the near IR to photon energies  $< 1.1\text{ eV}$ . This is the motivation of this thesis and it specifically focuses on the possibility to tailor the dispersion relation of the surface plasmon polariton (SPP) by using different structures supporting either propagating surface plasmon resonance (SPR) or localized surface plasmon resonance (LSPR).

The first part of this work focuses to gain control over the SPP dispersion relation by the introduction of (ordered and disordered) porosity in gold films using etching and dealloying methods. The SPPs propagating on these nanoporous structures are investigated by using reflection spectroscopy in Kretschmann configuration (KC) and leakage radiation microscopy (LRM). The data show a clear red shift (up to  $0.85\text{ eV}$ ) in the dispersion relation with increasing porosity.

The second part of the thesis deals with the possibility to tailor plasmonic nanoantennas and to shift their localized surface plasmon resonance towards the near infra red in far field using transmission microscopy technique. The nanoantennas fabricated using e-beam

---

lithography show a red shift in the single particle spectra (from  $800\text{ nm}$  to  $1050\text{ nm}$ ) for increasing sizes and/or increasing aspect ratios. The similar red shift has been observed around  $1400\text{ nm}$  in emission peaks, during the micro-photoluminescence measurement, when nanoparticles with the same resonance frequency as the nanoantennas are placed in their vicinity. Finally, an emission enhancement ratio of upto 3.4 times has been observed for the gold nanoantennas.

The final results from all the samples of this thesis show great potential for tailor-made SPPs that will enable optical engineers to easily design plasmonic devices, that employ optical antenna structures for wave guiding and enhanced photo-emission in the near infra red regime.

# Contents

|   |           |
|---|-----------|
| <b>Abstract</b>   | <b>i</b>  |
| <b>1. Introduction</b>  | <b>1</b>  |
| <b>2. Propagating Surface Plasmons at Solid and Nanoporous Metal-Air Interface</b>                              | <b>4</b>  |
| 2.1. Theoretical background . . . . .   | 4         |
| 2.1.1. Surface plasmon solutions . . . . .  | 4         |
| 2.1.2. Effective medium theory . . . . .  | 9         |
| 2.2. Experimental details . . . . .   | 15        |
| 2.2.1. Fabrication and structural characterization of nanoporous Au films                                       | 15        |
| 2.2.2. Experimental setups for optical excitation of SPs . . . . .  | 22        |
| 2.3. Results and discussions on propagating surface plasmons on nanoporous<br>metal films . . . . .             | 29        |
| 2.3.1. Angle resolved spectroscopy . . . . .  | 29        |
| 2.3.2. Theoretically derived SP dispersion relation from EMTs . . . . .   | 33        |
| 2.3.3. Leakage radiation microscopy . . . . .   | 38        |
| 2.3.4. Comparison of wave vectors by two different experimental methods   | 43        |
| 2.3.5. Photoluminescence characterization . . . . .   | 46        |
| 2.4. Summary of Part I . . . . .  | 51        |
| <b>3. Localized Surface Plasmons on Metal Nanoantenna Arrays</b>  | <b>54</b> |
| 3.1. Theoretical background . . . . .   | 54        |
| 3.1.1. Calculation of extinction for spherical Au nanoantennas embedded<br>in $n = 1.5$ by Mie theory . . . . . | 55        |
| 3.1.2. Plasmonic nanoantennas arranged in a regular array . . . . .   | 56        |
| 3.1.3. State of the Art . . . . .   | 61        |
| 3.2. Fabrication and structural characterization of nanoantennas . . . . .                                      | 63        |
| 3.2.1. Overview of fabricated samples . . . . .   | 65        |
| 3.2.2. Change in size . . . . .   | 65        |
| 3.2.3. Change in period . . . . .   | 66        |
| 3.2.4. Change in elongation . . . . .   | 66        |

|   |            |
|---|------------|
| 3.3. Optical characterization by transmission measurements . . . . .            | 69         |
| 3.3.1. Embedding the nanoantenna arrays in 1.5 refractive index . . . . .       | 69         |
| 3.3.2. Transmission measurement setup for nanoantennas . . . . .                | 69         |
| 3.3.3. Array of nanoantenna disks with 250 nm diameter . . . . .                | 70         |
| 3.3.4. Effect of change in size of Au disk nanoantennas . . . . .               | 75         |
| 3.3.5. Effect of change in periodicity of Au disk nanoantenna arrays . . . . .  | 77         |
| 3.3.6. Effect of change in aspect ratio of Au nanoantennas . . . . .            | 80         |
| 3.4. Optical characterization by photoluminescence measurements . . . . .       | 82         |
| 3.4.1. Embedding in PMMA containing PbS quantum dots . . . . .                  | 82         |
| 3.4.2. $\mu$ -Photoluminescence setup . . . . .                                 | 82         |
| 3.4.3. Effect of change in size of disk shaped antennas . . . . .               | 84         |
| 3.4.4. Effect of change in aspect ratio antennas . . . . .                      | 86         |
| 3.5. Summary of Part II . . . . .   | 88         |
| <b>4. Overall Summary and Outlook</b>   | <b>89</b>  |
| <b>Appendices</b>   | <b>91</b>  |
| <b>A. Wave equation to surface plasmon equation</b>                             | <b>92</b>  |
| A.1. TM or P modes . . . . .  | 93         |
| A.2. TE or S modes . . . . .  | 95         |
| <b>B. Dispersion relation in MATLAB</b>   | <b>96</b>  |
| B.1. Angle resolved simulation by Bruggeman and Maxwell-Garnett Model . . . . . | 96         |
| B.2. Wave vector by Bruggeman and Maxwell-Garnett Model . . . . .               | 99         |
| B.3. Transmission Calculation . . . . .   | 101        |
| <b>Bibliography</b>   | <b>103</b> |
| <b>List of Figures</b>  | <b>111</b> |
| <b>List of Tables</b>   | <b>116</b> |
| <b>Acknowledgments</b>  | <b>117</b> |
| <b>Curriculum vitae / Lebenslauf</b>  | <b>119</b> |
| <b>List of Publications</b>   | <b>120</b> |
| <b>Self declaration / Eidesstattliche Erklärung</b>                             | <b>121</b> |

# 1. Introduction

Rapid developments in nanotechnology with structuring, tailoring and recording on the nanometer scale [1–4] has lead to the rejuvenation of many fields including plasmonics [5–8]. Nanostructured metals have shown very special optical properties by supporting surface plasmons (electronic oscillations propagating at metal-dielectric interface [9]). Surface plasmons have shown strong field confinement at metal-dielectric interface which in-turn enhance non-linear effects at the interface. Furthermore, the surface plasmons can exhibit small group velocities, i.e. large photonic density of states which have been used for enhancement in light emission. These special properties of surface plasmons are being used in many nanophotonic applications like waveguides [10–16], ring resonators [17], lasers and LEDs [18], optical-electronic circuits in lab on a chip systems [19, 20], super resolution lenses [21–23], sensors [24, 25], etc. Okamoto et al. specifically reported the enhancement of luminescence of GaN-quantum wells in contact with rough Ag-layers. An analysis of the dispersion relation of the surface plasmons at the GaN/Ag interface revealed that this was actually caused by the Purcell effect: For the material combination GaN/Ag the spectral range of low group velocity/high photonic density of surface plasmon states close to the limiting frequency  $\omega_{sp}$  just coincided with the emission range of the GaN-quantum well.

To harvest the possibilities of plasmonics for silicon photonics, requires a frequency shift of the plasmonic resonances towards the near IR (photon energies  $< 1.1 eV$ ), where Si is transparent and Si-photonics operates. This frequency shifting can be done in two ways, either by searching for new plasmonic materials or by bringing morphological changes in the existing noble metals on the nanoscale. Recently under the first approach, several new plasmonic materials (e.g. TiN, Al: ZnO) have been introduced which show a less negative dielectric constant but similar low losses [26–29] as the traditional metals. While, in the second approach the morphology of conventional plasmonic metals (Ag and Au) have also been tailored on nanoscale by creating voids, inclusions, nanopores or surface topographies [30–33] to increase their existing functionality. Both approaches have received a lot of interest over the past decade. However, this thesis focuses on the latter of the two methods with gold being the plasmonic metal under consideration.

The aim of this thesis is to gain control over the SP dispersion relation changing the metal morphology and using metal nanostructures. This will be applied to shift surface plasmon resonances to the Near-Infra Red (NIR) regime. As an example of the obtained functionality the luminescence enhancement in the NIR will be investigated. Conceptually, this approach is inspired by the creation of designer plasmons. The formation of collective designer surface plasmons [34–36] on metal surfaces, which are deliberately structured on the sub-wavelength scale. However, they have been investigated experimentally only in the microwave region up to now.

This thesis is divided into two parts, based on the types of surface plasmons (SPs) supported by the structures created. Part one deals with the propagating surface plasmons on continuous nanoporous films. Here, the nanoporous films form an effective media (so called “meta-metals”), whose effective permittivity can be controlled by changing its porosity. Part two describes the investigation of periodic nanoantenna arrays. Special interest is paid to the diffractive coupling of the local particle plasmons on these arrays which results in the appearance of sharp surface lattice resonances. Finally, the characteristics, advantages and disadvantages of both strategies are summarized and an outlook on possible future topics of investigation concludes the work.

# PART I

Propagating surface plasmons at solid and nanoporous metal-air interface

## 2. Propagating Surface Plasmons at Solid and Nanoporous Metal-Air Interface

Surface plasmons (SPs) or Surface plasmons polaritons (SPPs) are electromagnetic oscillations propagating and confined at metal ( $\epsilon_m$ ) - dielectric ( $\epsilon_d$ ) interface [8, 9, 37]. They exist in the spectral region where  $\epsilon_m < 0$  which is the case occurring below plasma frequency ( $\omega_p$ ) as shown in figure 2.1(a) [7, 38]. These surface waves originate from the coupling of the electromagnetic fields with the oscillations of an electron plasma and are confined to the surface of a translational invariant layer (at least in one dimension). The field of the SPPs decay evanescently along the propagation direction at the surface due to ohmic losses within the metal and/or also possible due to scattering at surface roughnesses. Propagating SP has a well-defined  $\omega - k$  (or E - k) relation which is studied in this part of the thesis.

### 2.1. Theoretical background

Dispersion relation of surface plasmons follows directly from the solution of Maxwell equations at metal-dielectric interfaces shown in Appendix A. Some important properties which show the effect of wave propagation direction and metal thickness on SP propagation are discussed in this chapter.

#### 2.1.1. Surface plasmon solutions

##### 2.1.1.1. Solid metal interface

First a single, infinite and flat interface between non-absorbing dielectric half space (having a real and positive  $\epsilon_d > 0$  for  $z > 0$ ) and conducting metal (having a complex dielectric function  $\epsilon_m(\omega)$  for  $z < 0$ ), is considered as shown in figure 2.1(b).

Let us consider a transverse magnetic (TM or p-polarized) wave that propagates in x-direction. In this polarization, the magnetic vector is perpendicular to the plane of incidence (the plane defined by the direction of propagation and the normal to the surface).

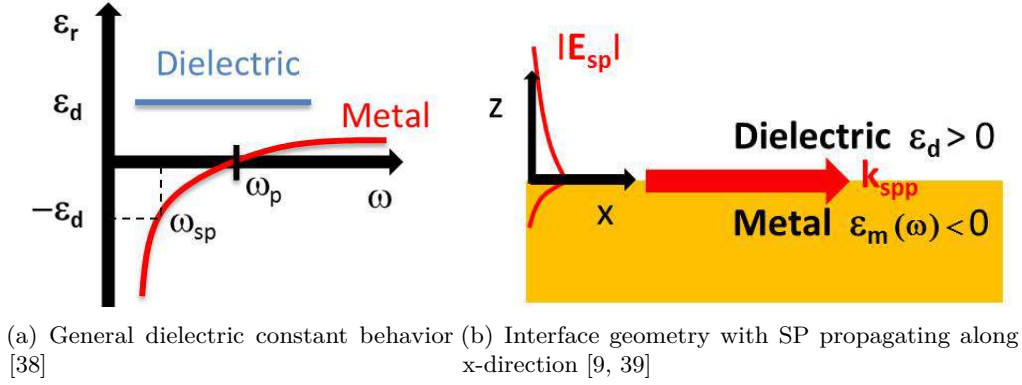


*Figure 2.1.: Schematic of surface plasmons at metal-dielectric interface*

A SP is formed that propagates at the interface and whose field decays exponentially perpendicular to z-direction. From the continuity of  $H_y$  and  $E_x$  at the interface, the dispersion relation of SPs at the interface follows as [9]:

$$k_x = \frac{\omega}{c} \sqrt{\frac{\varepsilon_m * \varepsilon_d}{\varepsilon_m + \varepsilon_d}} = \frac{2\pi E}{hc} \sqrt{\frac{\varepsilon_m * \varepsilon_d}{\varepsilon_m + \varepsilon_d}}. \quad (2.1)$$

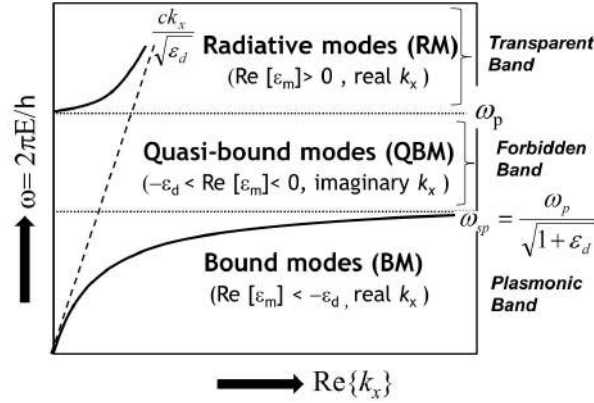
where,  $\varepsilon_m$  is permittivity of the metal which is, for example given as  $\varepsilon_m(\omega) = 1 - \frac{\omega_p^2}{\omega^2}$  and shown in figure 2.1(a). The above defined equation 2.1 is valid for all metals, that is, even for complex permittivity  $\varepsilon_m = Re(\varepsilon_m) + Im(\varepsilon_m)$ .

The dispersion of the dielectric constants of some metals can be explained reasonably well by using only the real part of permittivity  $\varepsilon_m$  (i.e.  $Im(\varepsilon_m) = 0$ ) i.e. a simple Drude model. Substituting the value of  $\varepsilon_m(\omega)$  in equation 2.1, the following relation is derived [40]:

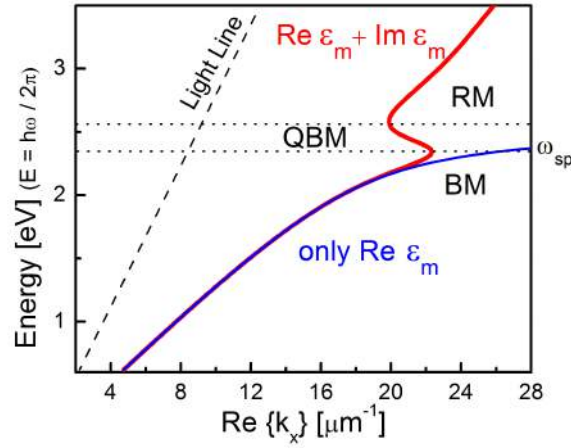
$$k_x = k_{sp} = \frac{\omega}{c} \sqrt{\frac{(\omega^2 - \omega_p^2) * \varepsilon_d}{(1 + \varepsilon_d) \omega^2 - \omega_p^2}} \quad (2.2)$$

From this equation, it is clear that the wave propagation in a medium defined by the Drude model assumes distinct behavior below and above  $\omega_p$  [7]. Hence, the SPs can be explained by different modes [7, 8] in a  $\omega - Re(k_x)$  graph, i.e. the dispersion relation (as in figure 2.2(a)): **Bound modes (BM)** occur for all  $\omega \leq \omega_{sp}$ . These bound modes define the usual surface plasmons that occur at the interface, especially when the  $Re(\varepsilon_m) < -\varepsilon_d$ , and when  $k_x$  is completely real. This spectral band is also called the plasmonic band. The next of the modes which lies in the region  $\omega_{sp} < \omega < \omega_p$  is the **Quasi-bound mode**

## 2. Propagating Surface Plasmons at Solid and Nanoporous Metal-Air Interface



(a) Schematic showing dispersion relation of SPs for Drude Model and the different modes [7]



(b) Theoretically calculated SP dispersion relation at Gold-air interface using real part of  $\epsilon_m$  (blue) and using both real and imaginary parts of  $\epsilon_m$  (red)

**Figure 2.2.:** Dispersion relation of surface plasmons at metal-dielectric interface

**(QBM)**. It is the frequency gap region with purely imaginary  $k_x$  and  $-\epsilon_d < \text{Re}(\epsilon_m) < 0$ . Hence, prohibiting the propagation of SPs i.e. the wave decays exponentially with distance inside the metal and therefore, called as the forbidden band [7]. Finally, the last of the three modes is the **Radiative mode (RM)**, where  $\omega > \omega_p$ , and occur for all the  $\text{Re}(\epsilon_m) > 0$  and the real  $k_x$ . The wave propagates through the metal without any decay i.e. the metal is transparent to the electromagnetic wave (transparent band). Summing

up, the Drude model states that for frequencies above plasma frequency metals should become transparent to electromagnetic radiation.

Now, taking a closer look at the dispersion relation (figure 2.2(a)) and looking specifically at the boundaries of the bound mode. The origin of the dispersion relation happens when  $\omega$  value is very small, i.e.  $\omega \rightarrow 0$  then  $\varepsilon_m \rightarrow -\infty$  to get the value  $k_x = \frac{\omega}{c} \sqrt{\varepsilon_d}$ .

When, the dispersion relation flattens,  $\omega \rightarrow \omega_{sp}$ ,  $\varepsilon_m \rightarrow -\varepsilon_d$ , then  $k_x \rightarrow \infty$ , which gives  $\omega \rightarrow \omega_{sp} = \frac{\omega_p}{\sqrt{1+\varepsilon_d}}$ . This shows a better confinement of the SPP at the interface but small propagation length (i.e. increased damping).

Furthermore, this flattening of dispersion relation also gives the tendency of the group velocity which is defined as [7–9]:

$$\nu_g = \partial\omega/\partial k \rightarrow 0 \quad (2.3)$$

i.e. the slope of the tangent to the curve goes to zero. This mode hence acquires an electrostatic character i.e. a bound surface plasmon.

In real metals,  $Im(\varepsilon_m) \neq 0$  i.e.  $\varepsilon_m = Re(\varepsilon_m) + Im(\varepsilon_m)$ . Now, the modes mentioned for the Drude Model are still existent with the same names but show different behavior. To show this comparison a calculated dispersion relation of bulk Au is plotted by using only the real part of  $\varepsilon_m$  (which follows Drude Model) and is shown as a blue curve in figure 2.2(b). This blue curve flattens at  $\omega_{sp}$ . But, when the same calculation is done using both the real and imaginary parts of  $\varepsilon_m$  the curve no longer flattens but proceeds as the red curve in figure 2.2(b). The quasi bound mode, which gave no real solutions in the Drude model, now results in a complex mode with  $Im(k_x)$ , this results in a propagating component even in the forbidden band by incorporating the  $Im(\varepsilon_m)$  and also involves lot of absorption into the metal due to the imaginary part.

This  $Im(\varepsilon_m)$  causes Ohmic damping of the conduction electrons by intraband and interband damping in the metal. Such a complex permittivity in equation 2.1 results in a complex  $k_x = Re(k_x) + Im(k_x)$ , where  $Re(k_x)$  defines the wavelength of the SPPs and the  $Im(k_x)$  defines the propagation length of the SPs. This complex propagation constant, also results in the damping term  $exp(-Im(k_x)x)$  which leads to the well known surface plasmon propagation length which is defined as  $L_{spp} = \frac{1}{2Im(k_x)}$  [9, 41, 42]. Furthermore, the  $Im(\varepsilon_m)$  is a material parameter and does not include other scattering factors that come into play from structuring of the materials. Like, there are many topographical losses, for e.g. surface roughness scattering, electron scattering from microstructural

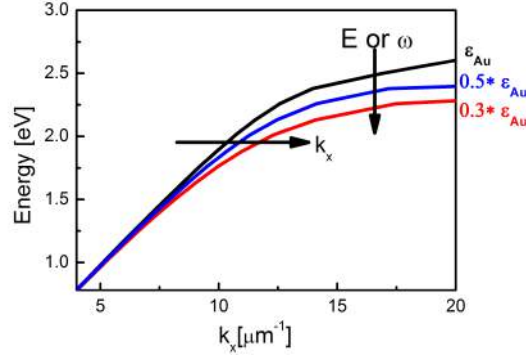


**Figure 2.3.:** Dispersion relation of gold by hypothetically increasing porosity [ $\epsilon_{Au}$  (bulk black),  $0.5 \epsilon_{Au}$  (50% porous blue) and  $0.3 \epsilon_{Au}$  (80% porous red)] i.e. increasing  $\epsilon_{eff}$  (less negative value) of nanoporous gold. Showing a red shift with increasing porosity.

grain size, etc. All these scattering factors have to be considered along with the  $Im(\epsilon_m)$  to define the total extinction from the metal.

All the lucrative properties arising from the flattening of dispersion relation, i.e. small group velocities and strong field confinement at metal dielectric interface of SPs is the motivation of this thesis.

### 2.1.1.2. Porous metal interface

The wave vector given in equation 2.1, is usually controlled by varying the external dielectric constant  $\epsilon_d$  or  $\epsilon_m$ . Here,  $\epsilon_m$  is changed by introducing porosity into the metal. Porosity is a mixture of air in metal i.e. sub-wavelength structure sizes of air compartments in the metal matrix. Such mixtures are seen by the incident light wave as an effective material. The properties of such an effective medium are defined by its content (fill fraction, permittivity) and shape of its components. Details of defining the value of  $\epsilon_{eff}$  of such porous metals using effective medium approximations will be described in the following sections. Introducing porosity increases the effective permittivity of the metal ( $\epsilon_{eff}$  is less negative) with respect to its solid counterpart. This will have an impact on the dispersion relation of SPs. An effective dielectric constant is used for calculating dispersion relation of such porous films and is given as:

$$k_x = \frac{\omega}{c} \sqrt{\frac{\epsilon_{eff} * \epsilon_d}{\epsilon_{eff} + \epsilon_d}}; \quad (2.4)$$

The impact of a hypothetical change of the dielectric of metal is shown in figure 2.3. As an example, the SP on air-gold interface is assumed (black line). Shifting the dielectric from  $\varepsilon_{Au}$  to  $0.5\varepsilon_{Au}$  (blue) or  $0.3\varepsilon_{Au}$  (red) by introduction of a large porosity will lower the dispersion relation, where, the  $\omega$  (or in other words energy) is red shifted and  $k_x$  shifts to larger values. This effect of increasing the porosity (i.e. increasing  $\varepsilon_{eff}$ ) on dispersion relation of porous gold is shown in this thesis. Porous structures are fabricated and characterized optically to analyze the predicted red shift of the dispersion relation in the following sections of the thesis.

### 2.1.2. Effective medium theory

Homogeneity has been debated over decades and it is just a matter of scale to see even a very homogeneous mixture as heterogeneous [40]. The properties of heterogeneous mixtures are highly variable and hence, defining the very basic parameters like the dielectric constant becomes difficult. So, effective medium theories have been introduced to make it simpler to define parameters pertaining to heterogeneity. The classic and the most well known of the EMTs are the Maxwell-Garnett(MG) [43] and Bruggeman (BG) [44] theories [40, 45, 46].

The main difference between MG and BG theory is the topology of the random effective medium [47]. While, MG theory considers isolated spheres embedded in a material with different dielectric constant, the BG theory starts from a symmetric arrangement of lumps of both materials. As a consequence, BG theory leads to an expression for dielectric constant that is symmetric upon interchanging the two dielectric constants as well as their respective filling fractions. In contrast, MG theory leads to a formula that does not exhibit this symmetry. In the following subsections, we derive both for two component systems and show their direct application for our samples.

#### 2.1.2.1. Bruggeman Model

When the matrix and inclusions are inseparable and intertwined, a clear line between matrix and inclusions is missing. So, Bruggeman treated the two parts (matrix and inclusion) in a symmetrical fashion [40, 45, 46]. The electrodynamics treatment is given twice, once to inclusion  $(\varepsilon_i, \eta_i)$  embedded in effective material and then to the matrix  $(\varepsilon_m, \eta_m)$  embedded in effective material. Both these cases when superimposed, as shown in figure 2.4(a), should give an effective medium. Consider the inclusion of radius  $a$  and a

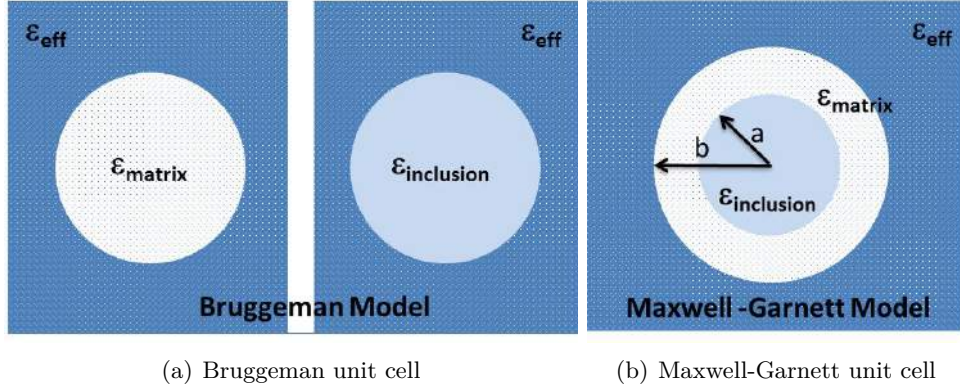


**Figure 2.4.:** Effective-medium theories basic unit cell [40, 46]

constant external electric field  $E_0$  along the z-direction and far from the inclusion which is defined in spherical coordinate system  $(r, \theta)$  as shown in figure 2.5.

From basic electrostatics, the electric field outside and inside a sphere are given as [46]:

$$E_{outside} = (E_0 + 2\frac{C_1}{r^3}) \cos \theta \hat{r} + (-E_0 + \frac{C_1}{r^3}) \sin \theta \hat{\theta} \quad (2.5)$$

$$E_{inside} = -A_1 \cos \theta \hat{r} + A_1 \sin \theta \hat{\theta} \quad (2.6)$$

where,  $\hat{r}$  and  $\hat{\theta}$  are the radial and polar unit vectors of spherical coordinate system.

Furthermore,  $C_1$  and  $A_1$  are equivalent dipole moments generating the fields  $E_{outside}$  and  $E_{inside}$  of the spheres, resp. and are given as [46]:

$$C_1 = \frac{\varepsilon_i - \varepsilon_{eff}}{\varepsilon_i + 2\varepsilon_{eff}} a^3 E_0; \quad (2.7a)$$

$$A_1 = -\frac{3\varepsilon_{eff}}{\varepsilon_i + 2\varepsilon_{eff}} E_0; \quad (2.7b)$$

The total electric flux deviation ( $D_{local} - D_{eff}$ ) due to polarization of inclusion in a plane perpendicular to the z-axis (parallel to  $E_0$ , i.e.  $\theta = \pi/2$ ) and inside the sphere is given as:

$$\Delta\phi_i = 2\pi \left( \int_0^a D_{local} r dr - \int_0^a \overbrace{\varepsilon_{eff} E_0}^{D_{eff}} r dr \right) \quad (2.8)$$

$$= 2\pi a^2 \varepsilon_{eff} E_0 \frac{\varepsilon_i - \varepsilon_{eff}}{\varepsilon_i + 2\varepsilon_{eff}}. \quad (2.9)$$

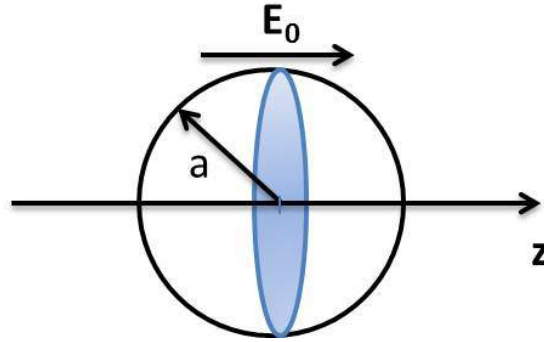


*Figure 2.5.: Bruggeman flux deviation through inclusion [46]*

where,  $i$  is either the dielectric or the metal sphere.

BG provides the hypothesis that there should be a zero average flux deviation, which reduces the calculation to [46]:

$$\eta_d \Delta \phi_d + \eta_m \Delta \phi_m = 0; \quad (2.10)$$

where,  $\eta_d (= f)$  and  $\eta_m (= 1 - f)$  is the volume fraction of the inclusions and matrix, respectively.

This gives us the well known BG formula as [46]:

$$f * \frac{\varepsilon_m - \varepsilon_{eff}}{\varepsilon_m + 2\varepsilon_{eff}} + (1 - f) * \frac{\varepsilon_d - \varepsilon_{eff}}{\varepsilon_d + 2\varepsilon_{eff}} = 0; \quad (2.11)$$

For highly porous, interlinked, spongy structures, this formula would be used for the calculations of effective dielectric constant in the forthcoming results. But for well separated medium, MG formula derived in the following subsection will be used.

### 2.1.2.2. Maxwell-Garnett Model

In Maxwell-Garnett model, a clear separation between matrix and the inclusion is assumed. For simplicity, Hashin et al. [48] assumed a shell model. Where, an inclusion ( $\varepsilon_i$ ) embedded in the matrix  $\varepsilon_m$ , and both are embedded together in an effective dielectric medium  $\varepsilon_{eff}$  are considered as shown in figure 2.4(b). We proceed as in BG case from electrostatics of concentric spheres.

## 2. Propagating Surface Plasmons at Solid and Nanoporous Metal-Air Interface

---

The field in the innermost sphere of inclusion, for  $0 < r < a$ , is given as:

$$E_a = -C_a \cos \theta \hat{r} + C_a \sin \theta \hat{\theta} \quad (2.12)$$

The next immediate area to this inclusion is a concentric shell of the matrix, ( $a < r < b$ ) the field in the matrix region is given as:

$$E_b = (C_b + 2\frac{C'_b}{r^3}) \cos \theta \hat{r} + (-C_b + \frac{C'_b}{r^3}) \sin \theta \hat{\theta} \quad (2.13)$$

The above two system of inclusion in a matrix should be replaced by an effective medium which exists from  $b < r < \infty$ . So, the field in the effective medium is given as:

$$E_{eff} = E_0 \cos \theta \hat{r} - E_0 \sin \theta \hat{\theta} \quad (2.14)$$

Boundary conditions: the continuity of  $D_{\perp}$  and  $E_{\parallel}$  for the interfaces  $r = a$  [40]

$$C_a - C_b + \frac{C'_b}{a^3} = 0; \quad (2.15a)$$

$$\varepsilon_i C_a - \varepsilon_m C_b + 2\varepsilon_m \frac{C'_b}{a^3} = 0; \quad (2.15b)$$

and  $r = b$

$$C_b + \frac{C'_b}{b^3} - E_0 = 0; \quad (2.16a)$$

$$\varepsilon_m C_b - 2\varepsilon_m \frac{C'_b}{b^3} - \varepsilon_{eff} E_0 = 0; \quad (2.16b)$$

These equations can be solved for C when the determinant of the coefficients vanishes [40].

$$\begin{vmatrix} -1 & 1 & \frac{a^3}{b} & 0 \\ -\varepsilon_{eff} & -\varepsilon_m & -2\varepsilon_{eff}(\frac{a}{b})^3 & 0 \\ 0 & 1 & 1 & -1 \\ 0 & \varepsilon_m & -2\varepsilon_m & -\varepsilon_i \end{vmatrix} = 0; \quad (2.17)$$

this gives us the Maxwell-Garnett formula, which is valid for 3D spheres:

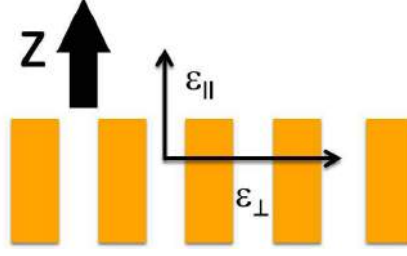


**Figure 2.6.:** 2D Maxwell-Garnett model for a columnar structure showing the directions of  $\varepsilon_{\perp}$  and  $\varepsilon_{\parallel}$

$$\frac{\varepsilon_{eff} - \varepsilon_m}{\varepsilon_{eff} + 2\varepsilon_m} = f \frac{\varepsilon_i - \varepsilon_m}{\varepsilon_i + 2\varepsilon_m}; \quad (2.18)$$

where,  $f = (\frac{a}{b})^3$  is the volume fraction of the inclusion.

This equation can also be re-written as [47]:

$$\varepsilon_{eff} = \varepsilon_m \frac{1 + 2f\Delta}{1 - f\Delta}; \quad \text{where } \Delta = \frac{1}{\varepsilon_m} \frac{\varepsilon_i - \varepsilon_m}{\varepsilon_i + 2\varepsilon_m} \quad (2.19)$$

**2.1.2.2.1. MG for uni-axial columnar effective medium:** The above section is valid for all 3D spheres but when there is a 2D symmetric case, a simpler uniaxial column formula can be derived. The same Maxwell's equations defined in the above 3D case are used.

This case is valid for solid metal wires or air pores which are parallel and embedded in a dielectric or metal matrix. In this thesis, MG 2D model is considered for effective medium with parallel air pores in gold matrix. Such an effective medium has two principle dielectric constants. One with  $\varepsilon_{\parallel}$  and other perpendicular  $\varepsilon_{\perp}$ , as shown in figure 2.6. The effective dielectric constant is given as a tensor of the form:

$$\vec{D} = \underbrace{\begin{pmatrix} \varepsilon_{\perp} & 0 & 0 \\ 0 & \varepsilon_{\perp} & 0 \\ 0 & 0 & \varepsilon_{\parallel} \end{pmatrix}}_{\varepsilon_{eff}} \vec{E} \quad (2.20)$$

To determine the  $\varepsilon_{\parallel eff}$ , the E field parallel to the wires or pores, i.e. the optical axis is considered and is given by equation 2.21a. This field is insensitive to directionality of pores, and is given as a simple volume averaged dielectric constant as defined by Newton [40].

Whereas, to determine the  $\varepsilon_{\perp eff}$  i.e. in the perpendicular case. The Maxwell- Garnett theory as shown in equation 2.19 is used, except that the value of  $\Delta$  is changed a little and is calculated by Kirchner et. al. [49] for the 2D case, is given as:  $\Delta = \frac{1}{\varepsilon_m} \frac{\varepsilon_i - \varepsilon_m}{\varepsilon_i + \varepsilon_m}$ . The final equation for air pores in gold matrix is inspired by [43, 50] who have derived MG 2D for inclusion (metal rods) embedded in dielectric matrix (air). For this thesis, the equation for air rods embedded in metal matrix are given as:

$$\varepsilon_{\parallel eff} = f \varepsilon_a + (1 - f) \varepsilon_{Au} \quad (2.21a)$$

$$\varepsilon_{\perp eff} = \varepsilon_{Au} \frac{(1 + f) \varepsilon_a + (1 - f) \varepsilon_{Au}}{(1 - f) \varepsilon_a + (1 + f) \varepsilon_{Au}} \quad (2.21b)$$

where,  $\varepsilon_a$  and  $\varepsilon_{Au}$  are the dielectric constants for air rods and gold metal matrix, respectively. To use these formulæ, need to input the air fraction  $f$  for each sample.

The possibility of exchange of the dielectric constants depending on the mixing criteria (metal in air or air in metal) to give different effective permittivity shows the versatility of the MG model which will be used in both parts of this thesis.

## 2.2. Experimental details

In this section, fabrication details of porous structures are described. Afterwards, the basic optical characterization techniques that were used to study the fabricated samples and determine the SP dispersion are presented.

### 2.2.1. Fabrication and structural characterization of nanoporous Au films

Samples with two different kinds of porous structures are fabricated in two different ways which are discussed in this section. First one, is a random porous gold structure which has a bi-continuous and interlinked porosity. The second structure is a continuous gold film and contains well ordered holes which are isolated from each other. A simple clear boundary exists between air pores and gold metal.

#### 2.2.1.1. Films with random nanopores

Spongy and random nanoporous gold was produced by dealloying technique. It is a process of selective corrosion or leaching, in which a less noble metal or a metal lower in electrochemical potential is selectively removed from its noble counterpart [31, 51, 52]. The higher the difference between the metals placed in the galvanic series, the easier it is to dealloy. For this sample, dealloying was carried out for white Au (50 wt% Au-50 wt% Ag). As both, Au and Ag, have similar lattice constants and crystallize in the face centered cubic structure, gold and silver atoms are homogeneously distributed [53] within the white gold alloy, so dealloying would leave homogeneously random porosity. Sample fabrication is carried out using 12-carat white gold leaves which were purchased from Dukatshop (Germany) and are ca. 180 nm thick. These leaves are floated on 65% conc.  $HNO_3$  for 10 mins, 30 mins and 60 mins similar as reported by Ding et. al. [31]. After this, the leaves are floated on water to rinse the residual acid and finally the films are placed on a glass slide (BK7) and the water is allowed to evaporate at room temperature.

Dealloying of 12 carat gold is carried out for different times. As time passes more Ag dissolves in  $HNO_3$  and gold atoms remain and aggregate due to surface diffusion (spinodal decomposition) into two-dimensional worm like clusters at the metal-electrolyte interface [51, 54]. The resulting nanoporous gold film has a sponge-type appearance. As the leaching time increases from 10 mins to 60 mins, the average pore diameter varies from 12 nm to 30 nm (figure 2.7(a) and 2.7(b)), respectively. In parallel to the removal of

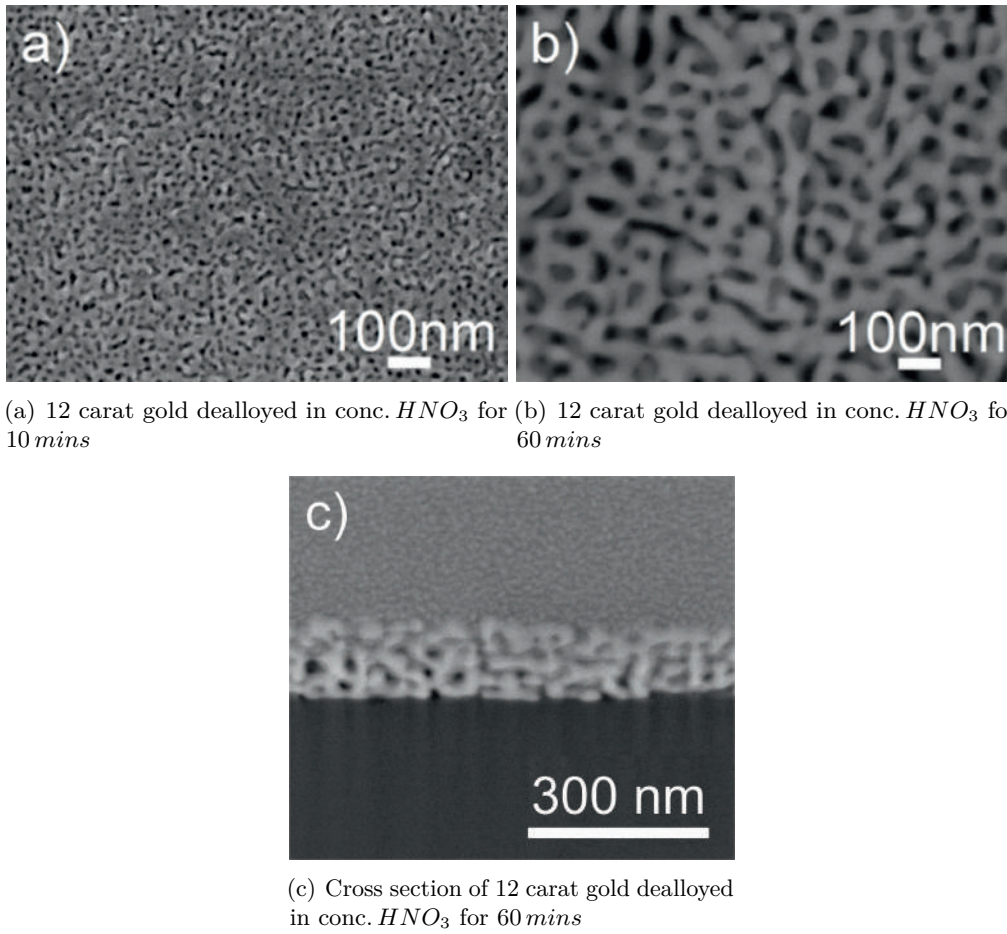


**Figure 2.7.:** SEM images of the dealloyed nanoporous gold samples. All structure sizes are considerably smaller than the wavelength of visible light

**Table 2.1.:** Effect of dealloying times on percentage of gold

| Sample                       | Weight percent of Gold | Atomic percent of Gold |
|------------------------------|------------------------|------------------------|
| Au-Ag (12 carat foil)        | 50.5                   | 35.8                   |
| 10 min dealloying in $HNO_3$ | 89.1                   | 81.8                   |
| 30 min dealloying in $HNO_3$ | 96.1                   | 93.1                   |
| 60 min dealloying in $HNO_3$ | 100                    | 100                    |

Ag atoms, the surface area continuously increases and a coarser gold skeleton structure is formed. The cross section prepared by FIB shows the interconnected porosity for all samples forming a bi-continuous network of air pores and gold veins (figure 2.7(c)).

To determine the stoichiometric composition of the nanoporous films after leaching, energy dispersive X-ray spectroscopy (EDX) measurements were carried out. The percentage of Au and Ag left after a certain dealloying time is shown in table 2.1. As the dealloying time increases, more and more silver dissolves. The concentration of Au in the Au-Ag dealloyed samples rises. After 60 *mins* of dealloying, all the silver of the original 180 *nm* thick white gold leaf is dissolved in the acid and the film consisting of pure porous gold is left floating on the surface of the acid. For all the following investigations, only the 60 *min* dealloyed film, is considered. In this way, any possible influence of silver remnants, which could also influence the effective dielectric constant of the porous film and impact the surface plasmon dispersion is avoided.

**Fill fraction determination:** For the 60 *min* dealloyed gold, the fill fraction is calculated using the volume loss of the film. The overall volume loss of the film can be determined by considering the complete loss of (64.2 *atomic* % = 50 *weight* %) silver from the original 12 carat white gold film due to the dealloying. However, very small change in the outer dimensions of the film is observed. The area of the film stays constant during the dealloying but the average thickness of the film reduces by one-third from 180 *nm* to about 120 *nm*. The remaining volume loss appears in the form of porosity of the remaining nanoporous gold film and the metal fill factor of the nanoporous gold film is determined as:

$$f * \frac{\text{Total At. wt. of 12 carat gold}}{\text{initial thickness}} = \frac{\text{At. wt. of Ag}}{\text{final thickness}} \quad (2.22a)$$

$$f * \frac{305}{180} = \frac{108}{120} \implies f \simeq 0.5 \quad (2.22b)$$

This c.a.  $f = 0.5$  is in agreement with the estimates for  $f$  obtained by evaluating the various SEM images of the film. For reference and comparison bulk gold sample is also considered. A 60 *nm* thick non-porous solid gold film, which has been deposited on a glass slide by thermal evaporation is considered as the reference bulk gold. This has a fill fraction of  $f = 1$ .

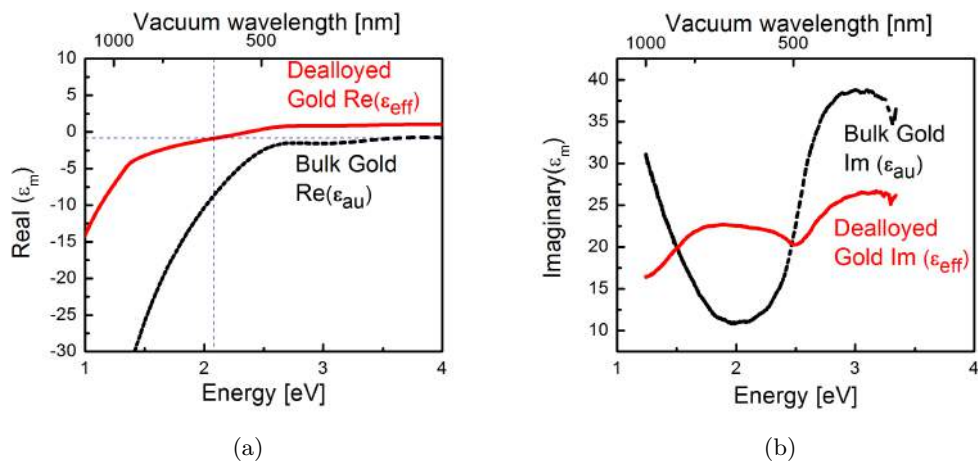


**Figure 2.8.:** Real and imaginary parts of the dielectric constant of the dealloyed nanoporous gold film (red) and of the evaporated bulk gold film (black) determined by spectroscopic ellipsometric measurements.

**2.2.1.1.1. Dielectric constant determination:** Ellipsometry is an elegant experimental technique to measure the dielectric constants of the thin films.

A dealloyed nanoporous gold and bulk gold sample on glass substrate were used for ellipsometry. The spectral evolution of the ellipsometric angles is fit with a model of single smooth metallic layer with a complex refractive index on a glass substrate which results in the effective dielectric constants of the metal films.

The real ( $\epsilon_{\text{eff}}$ ) and imaginary ( $\epsilon_{\text{eff}}$ ) parts of nanoporous gold and bulk gold are shown in figure 2.8. The surface and interface roughness influence (e.g. scattering losses) is incorporated in the fitted optical constants of the single metal layer only but not included specifically as an additional layer(/s) in the model. For layer thickness  $> 100 \text{ nm}$  the results for  $\epsilon_{\text{eff}}$  saturated and are not affected anymore by changes in the layer thickness. This insensitivity towards the layer thickness demonstrates that the ellipsometric measurements mainly probe the surface of the metal film and the contribution from the buried metal - glass interface is negligible too for these thicker films.

The condition  $\epsilon_m < -1$  ( $\epsilon_{\text{air}} = 1$ ) must be true in order to support surface plasmons at the metal-air interface (as defined in section 2.1.1.1). From figure 2.8, this condition is applicable for  $\lambda > 356 \text{ nm}$ , in the case of the bulk gold film while only valid at  $\lambda > 610 \text{ nm}$  for the nanoporous gold film. The imaginary part of the  $\epsilon$  of the nanoporous gold layers is lower in the near IR and for  $\lambda < 500 \text{ nm}$ . However,  $\text{Im}(\epsilon)$  of the nanoporous

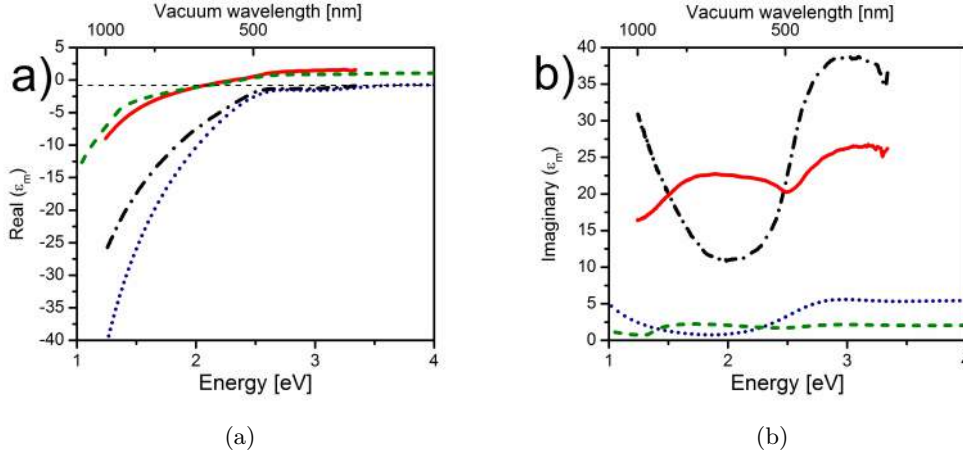


**Figure 2.9.:** Comparison of the dielectric constants determined by ellipsometry from figure. 2.8 with calculated values using the Bruggeman theory (a) Real part of the dielectric constant of the nanoporous gold and bulk gold film as received from ellipsometric data (red solid line and dash-dot black line, respectively) and calculated using Bruggeman effective medium model (green dashed line and blue dotted line, respectively) and corresponding (b) imaginary part of dielectric constant.

films is approximately a factor 2 larger than for the bulk gold film in the spectral range  $900 \text{ nm} > \lambda > 500 \text{ nm}$  resulting in a larger extinction for the nanoporous film.

#### 2.2.1.1.2. Comparison of permittivities obtained from ellipsometry and theoretical calculations:

As discussed in the theory part, the structural assumptions of the Bruggeman (BG) effective medium model fit well to the dealloyed nanoporous gold film. BG model is used to determine the dielectric constants of dealloyed nanoporous gold. The real parts of the permittivities ( $\text{Re}(\epsilon_{eff})$ ), which were determined by ellipsometry in previous section and the ones calculated via the Bruggeman theory are compared and shown in figure 2.9(a). The match for the dealloyed nanoporous gold film is even better than for the evaporated bulk gold film. However, comparing the imaginary parts of the permittivities ( $\text{Im}(\epsilon_{eff})$ ), clear differences of the absolute values are observed (figure 2.9(b)). The values determined by ellipsometry are about a factor 8 larger than the tabulated values for bulk gold or the calculated Bruggeman values. The spectral trend of  $\text{Im}(\epsilon_m)$  is on the other hand comparable:  $\text{Im}(\epsilon_m)$  of the nanoporous gold increases at about  $1.5 \text{ eV}$  and has a minimum at  $2.5 \text{ eV}$  for both ellipsometric data and Bruggeman calculation. Similarly, for the bulk gold layer: the minimum of  $\text{Im}(\epsilon_m)$  appears at  $1.9 \text{ eV}$  for both ellipsometric data and Bruggeman data. The main reason for the large values

of  $\text{Im}(\epsilon_m)$  of the samples, are probably, the scattering losses due to surface roughness of the porous films. Since, the ellipsometric model used only a single plane film as a representation of the bulk as well as the nanoporous gold films, all the scattering losses of the samples are included in the imaginary part  $\text{Im}(\epsilon_m)$  of the film. Furthermore the chance of impingement of the oscillating electrons at the internal nanostructured surfaces increased due to the porosity leading to increased electron scattering and decay of coherent plasmonic oscillation.

### 2.2.1.2. Films with regular nanopore arrays

In order to compare the nanoporous films comprising of random nanopores with a more regular arrangement of the porous network, the fabrication of ordered porous films, which is based on self-ordered nanoporous alumina templates is described in this section.

Hexagonally ordered porous alumina with pore sizes  $30 \pm 2 \text{ nm}$ ,  $55 \pm 2 \text{ nm}$  and  $70 \pm 2 \text{ nm}$  are received from Smart Membranes GmbH. These porous templates are coated with Au by the process of thermal evaporation to get a uniform thick film with a thickness of  $60 \pm 3 \text{ nm}$ . These samples are then placed in  $50 \text{ wt.}\% \text{ KOH}$  solution for  $20 \text{ mins}$  to etch away the alumina templates. After this, the leaves are floated on water to rinse the residual alkali and finally the hexagonally ordered films are placed on a glass slide (BK7) and the water is allowed to evaporate at room temperature.

The pore diameter of the template, and that of the, finally achieved hexaporous Au layer, have the same order of pore sizes, especially for smaller sizes. Therefore, the final hexaporous Au films with pore sizes of approx.  $30 \text{ nm}$ ,  $55 \text{ nm}$  and  $63 \text{ nm}$  are achieved. When the template pore size is increased to  $70 \text{ nm}$  the gold film becomes very fragile. During the final etching in KOH several pieces of the hexaporous Au film break off and deposit as a lot of debris on the sample (figure 2.10(c)). These debris result in increased surface roughness and a strongly increased light scattering, hence, an optical excitation of surface plasmons can not be observed anymore. Therefore, this structure is not considered in the thesis any further.

The pore size of the hexaporous samples is obtained directly from the SEM images by using the ImageJ software. First, the SEM image is converted into (black and white) binary format and then the area fraction of pores (black) is analyzed. By this procedure,

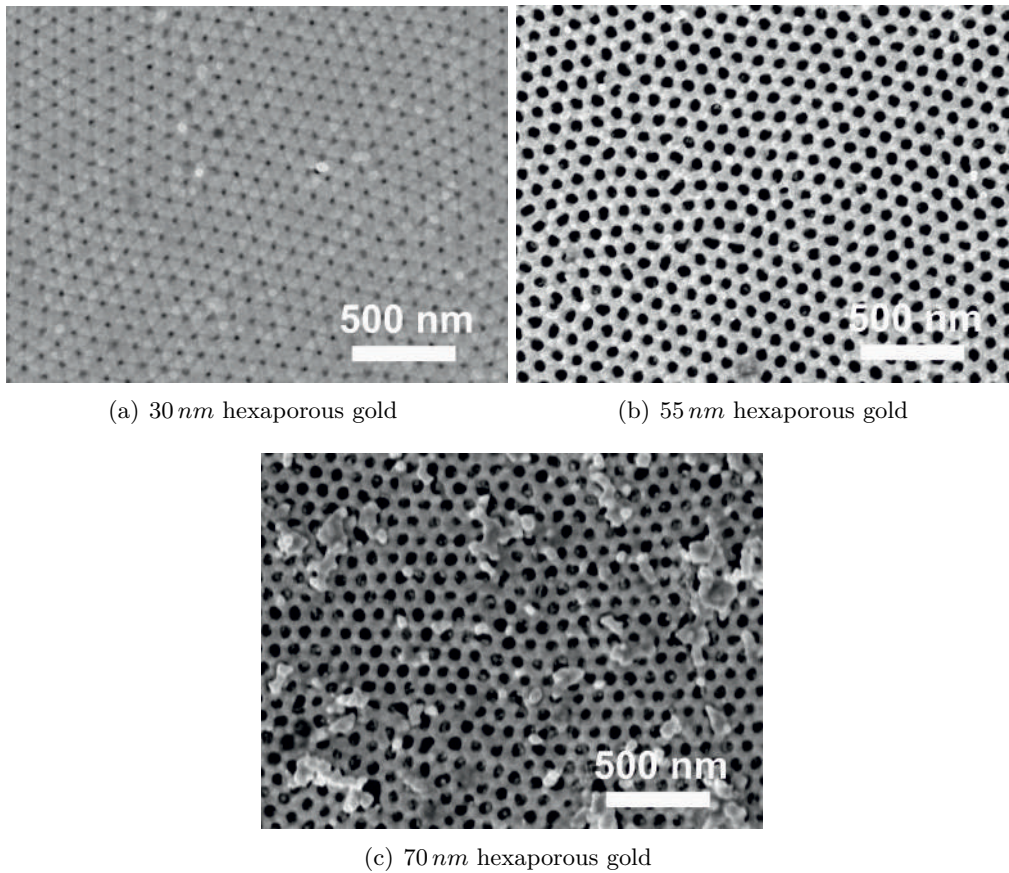


**Figure 2.10.:** SEM images of the hexaporous gold samples. All structure sizes are considerably smaller than the wavelength of visible light

$f = 0.2$  and  $0.3$  is obtained for nanoporous gold with pore sizes of  $30\text{ nm}$  and  $55\text{ nm}$ , respectively<sup>1</sup>.

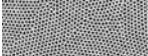
EDX was performed on hexaporous gold films, the results of which show no residual aluminum from the template. Hence, any result that will follow from such structures, is solely from ordered gold. Furthermore, the film thickness of the individual hexaporous samples was measured by X-ray reflectometry (XRR), which confirmed a ca.  $60\text{ nm}$  thick hexaporous gold layer.

<sup>1</sup>From now onwards, the gold with hexagonally organized pores will be named with their final pore sizes, like  $30\text{ nm}$  hexaporous gold and  $55\text{ nm}$  hexaporous gold. They should not be confused with the thickness. The thickness for all hexaporous gold films is always  $60\text{ nm}$ .

## 2. Propagating Surface Plasmons at Solid and Nanoporous Metal-Air Interface

---

**Table 2.2.:** Overview of all the continuous film samples that are used for study of propagating surface plasmons

| S.No. | Sample                    | Porosity (%) | LOM/SEM Image  |
|-------|---------------------------|--------------|--|
| 1     | Bulk Gold                 | 0            |  |
| 2     | Dealloyed nanoporous Gold | 54           |  |
| 3     | 30 nm Hexaporous Gold     | 20           |  |
| 4     | 55 nm Hexaporous Gold     | 30           |  |

No ellipsometric measurements were attempted for ordered nanoporous gold, as the more complex, effective medium models for the uniaxial materials (hexaporous Au films) were not readily available in the software of the ellipsometer setup.

### 2.2.1.3. Summary of samples

Besides the described random and ordered nanoporous samples, a bulk gold sample was fabricated for reference. It consisted of  $60\text{ nm}$  thick solid gold film, which was deposited on a glass slide by thermal evaporation.

So, overall a total of 4 samples are considered for a comparative study - namely bulk gold ( $f = 0$ ), spongy-dealloyed gold ( $f = 0.5$ ),  $30\text{ nm}$  ( $f = 0.2$ ) and  $55\text{ nm}$  ( $f = 0.3$ ) hexaporous gold. All these samples are shown in table 2.2. These samples are optically characterized by using Kretschmann configuration and leakage radiation microscopy which are discussed in the following section.

### 2.2.2. Experimental setups for optical excitation of SPs

The fabricated disordered and ordered nanoporous gold samples are optically characterized using angle resolved reflection spectroscopy in Kretschmann configuration and leakage radiation microscopy. These characterization methods allow the excitation of SPs and the experimental determination of their wave vector and frequency - delivering the SP dispersion relation. The two techniques and their specific experimental setups are discussed in this section.

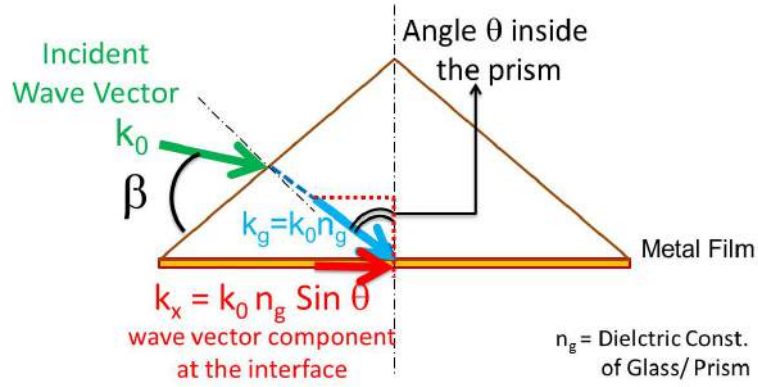


**Figure 2.11.:** Schematic of wave vectors and their components at Au-air interface inside a prism

### 2.2.2.1. Reflection spectroscopy by prism coupling

Since the SP wave vector at the air/gold surface is larger than the wave vector of light in air, the surface plasmons at Au-air interface cannot be excited directly by shining light on Au-air interface from air. However, light passing through dielectric with higher refractive index acquires a lateral wave vector which can excite SPs. Experimentally, this is realized by prism coupling (figure 2.11) and the change of incidence angle, which allows the matching of  $k_x$  in glass with the SP- $k_x$ . The lateral wave vector component inside the prism, which is parallel to the ground plane of the prism and the metal film, is given as [9, 55]:

$$k_{x\text{dielectric}} = n_{\text{dielectric}} * k_0 * \sin\theta; \text{ where } n_i = \sqrt{\epsilon_i}. \quad (2.23)$$

Under this condition, the Au-air SP is excited and the reflected light is reduced, since a large part of the energy traveling in the SP is gradually absorbed within the metal. This leads to a dip in reflection. There are two strategies to find the excitation condition for SP excitation in reflection, one is fixing the wavelength and varying the angle in which the surface plasmons [56] are excited for a single frequency. The second method<sup>2</sup> is by fixing the angle and doing a spectroscopic measurement and hence, investigating the surface plasmon dispersion over a large range of frequencies from the near infrared to the visible [57].

<sup>2</sup>The suitability of both these methods are compared theoretically in section 2.3.2.1.

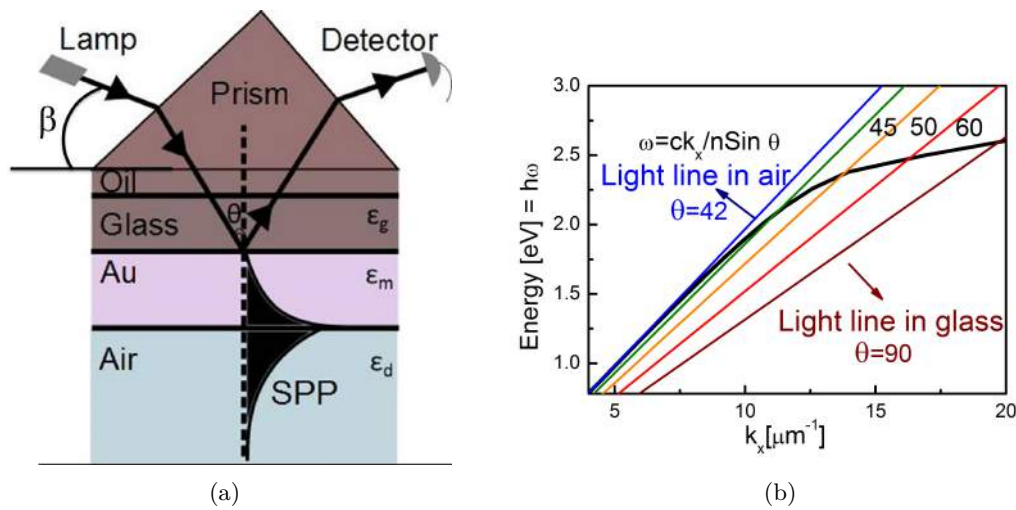


**Figure 2.12.:** (a) Kretschmann configuration; (b) Probing of dispersion relation by altering angle of incidence in Kretschmann configuration

In this thesis, the latter of the two methods is used hand in hand with the prism coupling method. Prism coupling can be achieved in either Kretschmann or Otto configuration. Experimentally, Otto configuration can be achieved only by introducing a very even vertical slit between prism and the metal, which has alignment problems for experimentation, so, we use Kretschmann configuration.

In the Kretschmann configuration (KC) (shown in figure 2.12(a)), the glass slide carrying the metal film is pressed against a right angled prism (BK7 glass,  $\epsilon_{glass} = 2.25$ ) and a drop of L4085 AGAR immersion oil ( $\epsilon_{oil} = 2.3$ ) from Plano labs (Germany) is applied between glass slide and prism. The surface tension of the oil ensures a close contact between sample and prism. Furthermore, undesired reflections at the glass interfaces are avoided due to the matching refractive indices of glass slide, oil and prism. In this configuration the light with higher  $k_{x,dielectric}$  coming from the dielectric has to tunnel through the Au film to excite the Au-air SP at the opposite free surface.

This Kretschmann configuration with prism and sample is mounted on a rotating stage, which is a part of a larger setup shown in figure 2.13. In this set-up, a beam of light from a halogen lamp (200 W) passing through a series of lenses and a birefringent crystal polarizer is incident on one of the prism side facets. The light which is reflected from the sample at the base of the prism exits via the opposite prism side facet and is picked

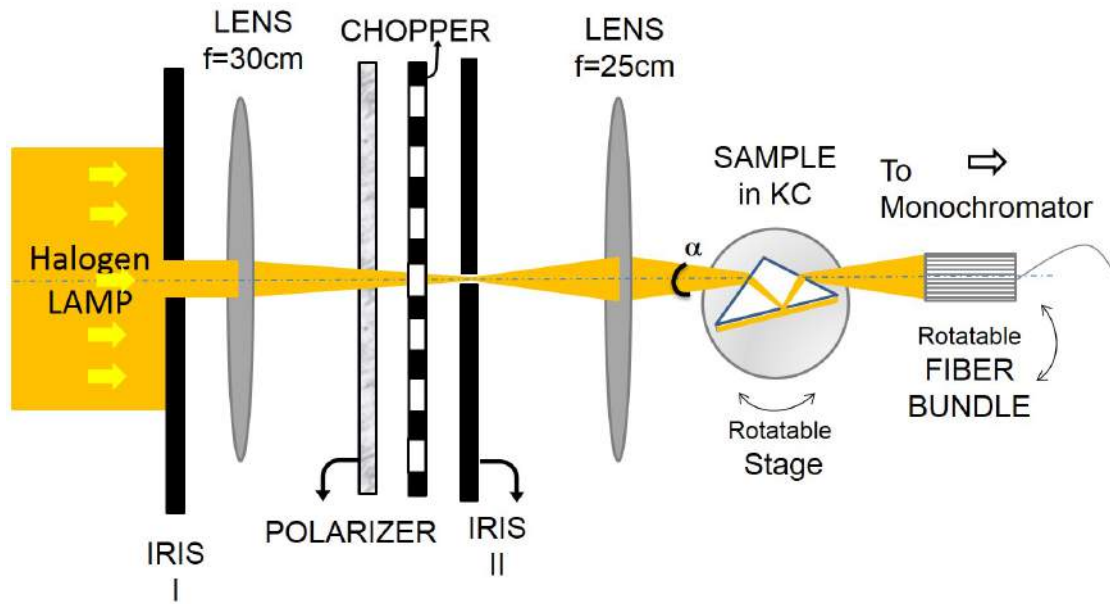


*Figure 2.13.: Schematic (top view) of setup for angle resolved spectroscopy measurements*

up by a fiber bundle guiding it to a grating spectrometer which is equipped with single channel photodiode detectors for the near IR and the visible wavelengths.<sup>3</sup>

By rotating the prism and the detecting fiber bundle with a relation of  $\theta - 2\theta$ , this setup allowed the measurement of angular resolved reflection spectra with incidence angles in the range of  $45^\circ < \theta < 68^\circ$  inside the glass (as defined in figure 2.12(a)) which corresponds to  $0^\circ < \beta < 80^\circ$  in air. Each angle of measurement gives an experimental data point which corresponds to a point in dispersion relation. The point of intersection of each angle of measurement with the dispersion curve (shown in figure 2.12(b)) corresponds to the dip in reflection measurements which will be discussed in detail in the results section 2.3.1.

### 2.2.2.2. Leakage radiation microscopy

For leakage radiation microscopy, SPs on air-metal interface are launched by illumination of a slit which is  $100\text{ nm}$  wide and  $50\ \mu\text{m}$  long and was prepared by FIB (Focused ion

<sup>3</sup>The full divergence angle of the incoming beam of light is determined from the setup distances and spot sizes. It is approx.  $\alpha = 1.14^\circ$ . The angle of divergence could partly influence the widening of the dips discussed in section 2.3.1.

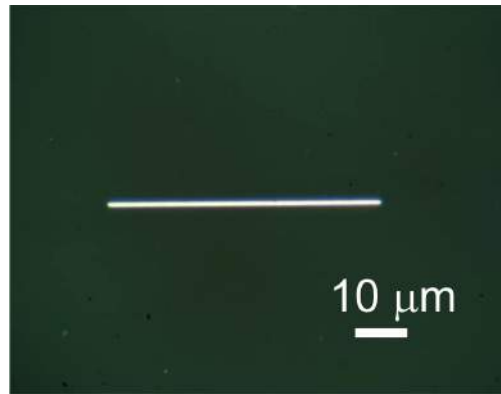


*Figure 2.14.: FIB milled slit on bulk gold as seen with the CCD.*

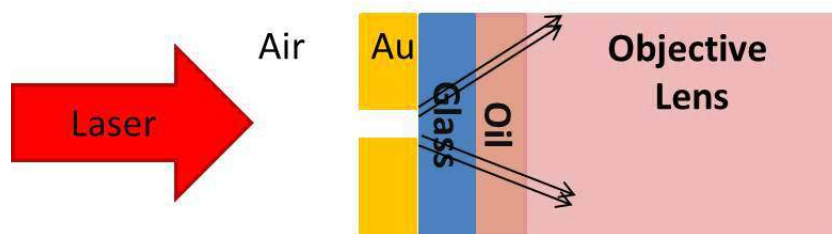


*Figure 2.15.: Schematic showing the contact layers of FIB milled sample, which mounted on the immersion oil objective. It shows the leaked radiation for LRM.*

beam) milling (figure 2.14). The glass slide carrying the FIB milled metal film is placed in the focus of the immersion microscope objective lens and a droplet of index matching oil is applied between sample and objective (figure 2.15). This setup is a part of a larger 4f leakage radiation microscopy (LRM) setup shown in figure 2.16. This setup allows the imaging of sample and the back focal plane of the objective lens L1.

In this set-up, the laser ( $\lambda = 780\text{ nm}$ ) is incident from the air slit interface. SPs propagating along the air-metal interface leak through the thin metal film and reach glass, where, it is radiated off as leakage radiation. Using an oil immersion objective ( $100\times$ , Numerical aperture (NA) = 1.4, Zeiss), the leakage radiation is collected and can be analyzed by arranging a set of lenses behind the objective. This can either image the real plane or the back focal plane of the objective, by focusing leaked radiation onto the CCD (ABS Jena) camera.

The real image of the sample is imaged by the setup shown in figure 2.16(a) (the red ray diagram in the middle). The sample attached to the immersion objective is at its focal distance, and hence could form a image at infinity, represented by the red parallel rays

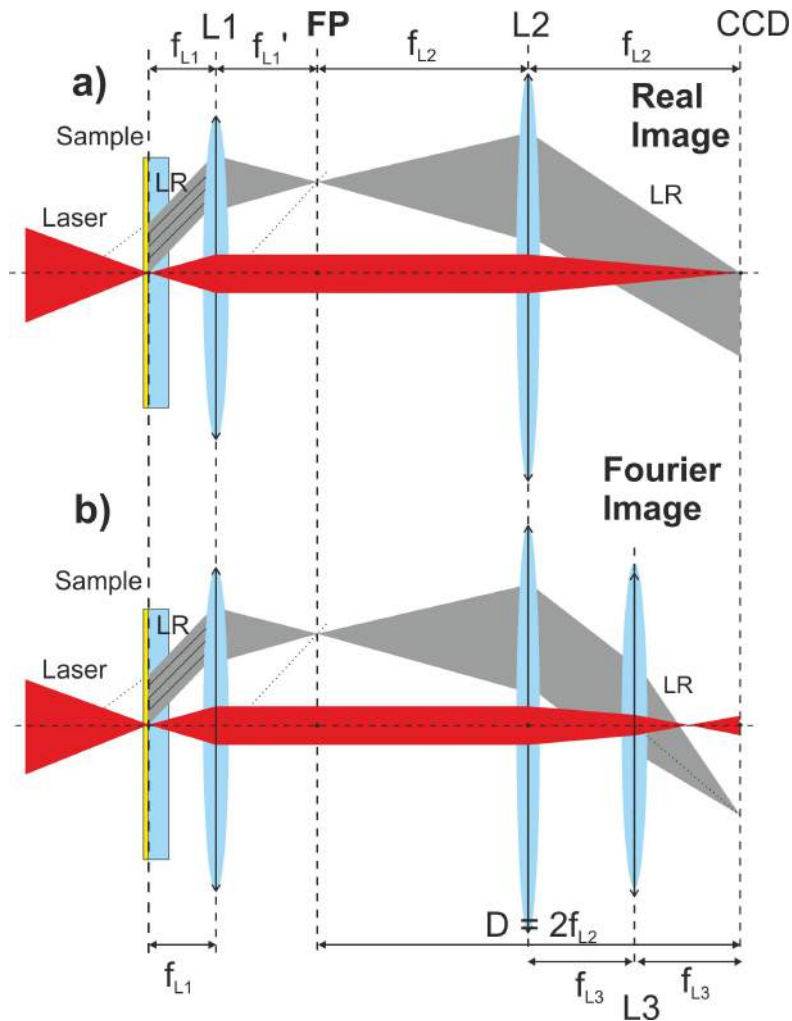


**Figure 2.16.:** Leakage radiation microscopy setup: (a) Real plane imaging and (b) Fourier plane imaging.

after L1. Using another lens L2 at a distance equal to its focal length from the CCD, a real image of the sample surface including the slit is formed on the CCD as shown in figure 2.14.

Furthermore, the parallel leakage radiation emitted at a specific angle from SP is focused at the back focal plane (FP) of the immersion objective L1. Now, to achieve an directional analysis i.e. angle at which the SPs are leaking, one needs to image the back focal plane of the immersion objective. To achieve this, another lens L3 is introduced in the beam path as shown in figure 2.16(b) and the gray ray diagram. An image of this FP is then created on CCD camera by the combination of lenses L2 and L3.

## 2. Propagating Surface Plasmons at Solid and Nanoporous Metal-Air Interface

---

This setup allows to switch between imaging of the back focal plane and the real image plane (IP) onto the CCD camera, by just introducing and / or eliminating the third lens L3. The back focal plane corresponds to the Fourier plane (FP) of the image which allows access to the angle at which the leakage radiation is emitted. From this, the lateral wave vector component  $k_x$  is determined [41, 42].

## 2.3. Results and discussions on propagating surface plasmons on nanoporous metal films

The wave vectors of surface plasmons on bulk gold, dealloyed gold, 30 *nm* and 55 *nm* hexaporous gold samples are experimentally determined using the angle resolved reflection spectroscopy in Kretschmann configuration (KC) and leakage radiation microscopy. In the first part, the results from the KC-measurements are shown which are also compared with the results predicted from theoretical effective medium models applying the Bruggeman model for dealloyed gold and Maxwell-Garnett model for hexaporous gold using the dielectric constants from Johnson & Christie [58, 59] data. Furthermore the dielectric constants of bulk gold and nanoporous dealloyed gold determined by ellipsometry are used to calculate and compare the SP dispersion relation. The final data is then confirmed with the experimental results. In the second section of optical results, the analysis of the SP wave vectors and the SP decay lengths is carried out using the leakage radiation microscopy. Finally, in the end of this section, all the results are compared and discussed together in a dispersion relation graph.

### 2.3.1. Angle resolved spectroscopy

Angle resolved spectroscopy is carried out in Kretschmann configuration (figure 2.12(a)) as discussed in previous section. The measured reflection spectra for p- and s-polarized light for the bulk, the dealloyed gold sample and hexaporous gold samples are shown in figures 2.17 and 2.18, respectively. In figures 2.17, the spectra are normalized by the p-polarized total reflection of a bare glass slide, and in figures 2.18, the spectra are normalized by the s-polarized total reflection of a bare glass slide, while the ratio of p-polarized reflection/s-polarized reflection is shown in figures 2.19. A characteristic dip in reflectivity is only observed for p-polarized light, which shifts to the shorter wavelengths with increasing angle of incidence. These dips are more clearly visible in the figures 2.19. Here, the overall dropping slope of the reflectivity, which is common to both p- and s-polarized light, is diminished by plotting the ratio of p- and s-polarized spectra. The overall drop in reflection towards shorter wavelengths is caused by the starting interband absorption in gold and by dividing the spectra with the s-polarized spectra, its effect on the SP dip position can be reduced, hence resulting in clear dip minima.

However, for  $\lambda < 900 \text{ nm}$ , the dips in reflectivity observed for the SP on nanoporous gold layers widen considerably, and it would be difficult to assign a clear single minimum.

## 2. Propagating Surface Plasmons at Solid and Nanoporous Metal-Air Interface

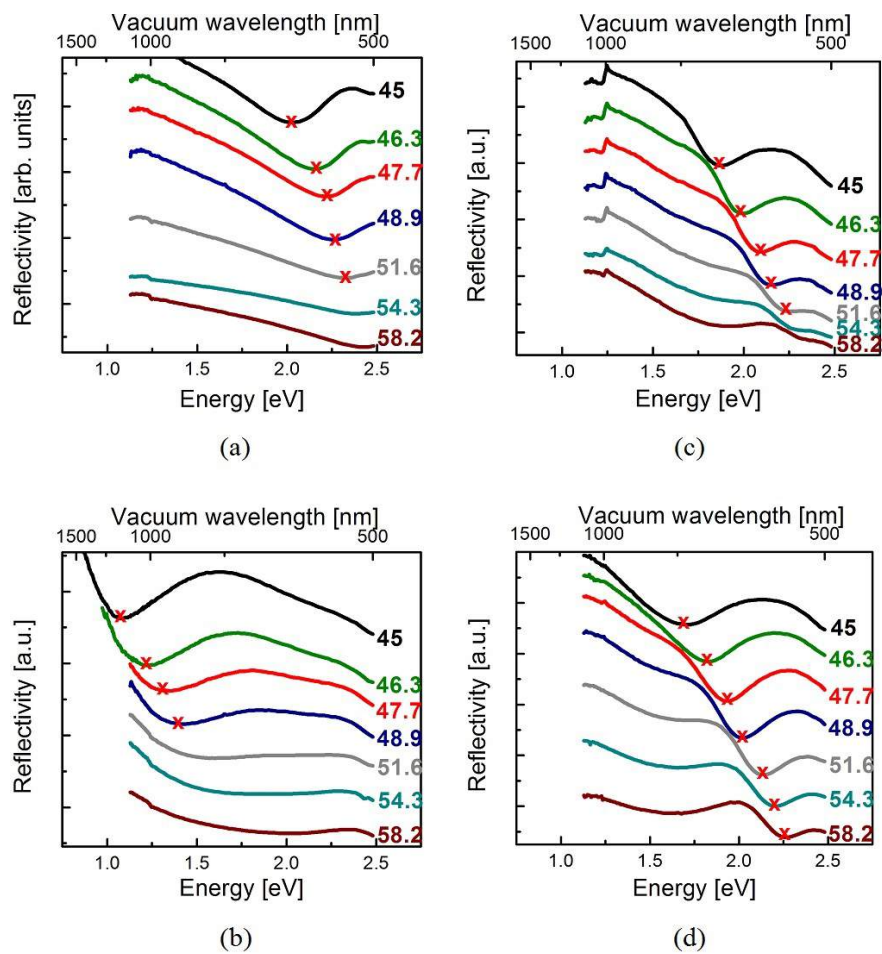


**Figure 2.17.:** Angular resolved reflectivity spectra in Kretschmann configuration. The plotted curves represent the ratio of p-polarized reflection for (a) bulk gold film (b) dealloyed nanoporous gold film (c) 30 nm hexaporous gold and (d) 55 nm hexaporous gold normalized with p-polarized glass background. The values of the angles of incidence in the glass are the same for all curves. A dip in reflection occurs, which shifts to shorter wavelengths with increasing angle of incidence (marked by the crosses). This indicates the resonant excitation of propagating surface plasmons.

This limits the experimental mapping of the dispersion relation of the nanoporous gold layers. The shift of the dip in p-polarized reflectivity is characteristic for the excitation of a propagating surface plasmon at the metal-air interface. The frequency  $\omega$  and the in-plane wave vector  $k_x$  of the reflection dip are determined to map the dispersion relation of the SPs given as:

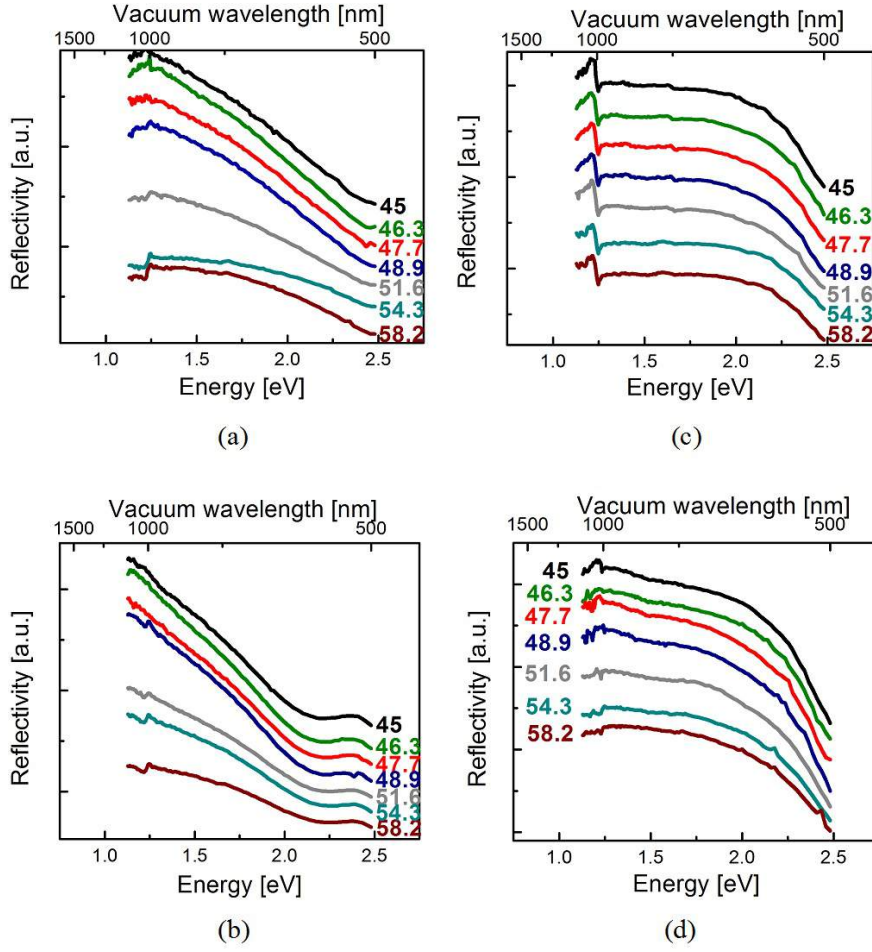


**Figure 2.18.:** Angular resolved reflectivity spectra in Kretschmann configuration. The plotted curves represent the ratio of *s*-polarized reflection for (a) bulk gold film (b) dealloyed nanoporous gold film (c) 30 nm hexaporous gold and (d) 55 nm hexaporous gold normalized with *s*-polarized glass background. The values of the angles of incidence in the glass are the same for all curves. No change in dip position is observed

$$k_x = \sqrt{\epsilon_g} \frac{\omega_{dip}}{c} \sin \theta \quad (2.24)$$

where,  $\epsilon_g$  is dielectric constant of glass and  $\theta$  is the angle of incidence within the glass at the base of the prism [9].

Generally, SPs can be excited for  $\theta > 41.83^\circ$  (critical angle for glass/air). In figure 2.20, the experimentally determined data points ( $k_x, \omega$ ) are indicated by the symbols (squares,

## 2. Propagating Surface Plasmons at Solid and Nanoporous Metal-Air Interface

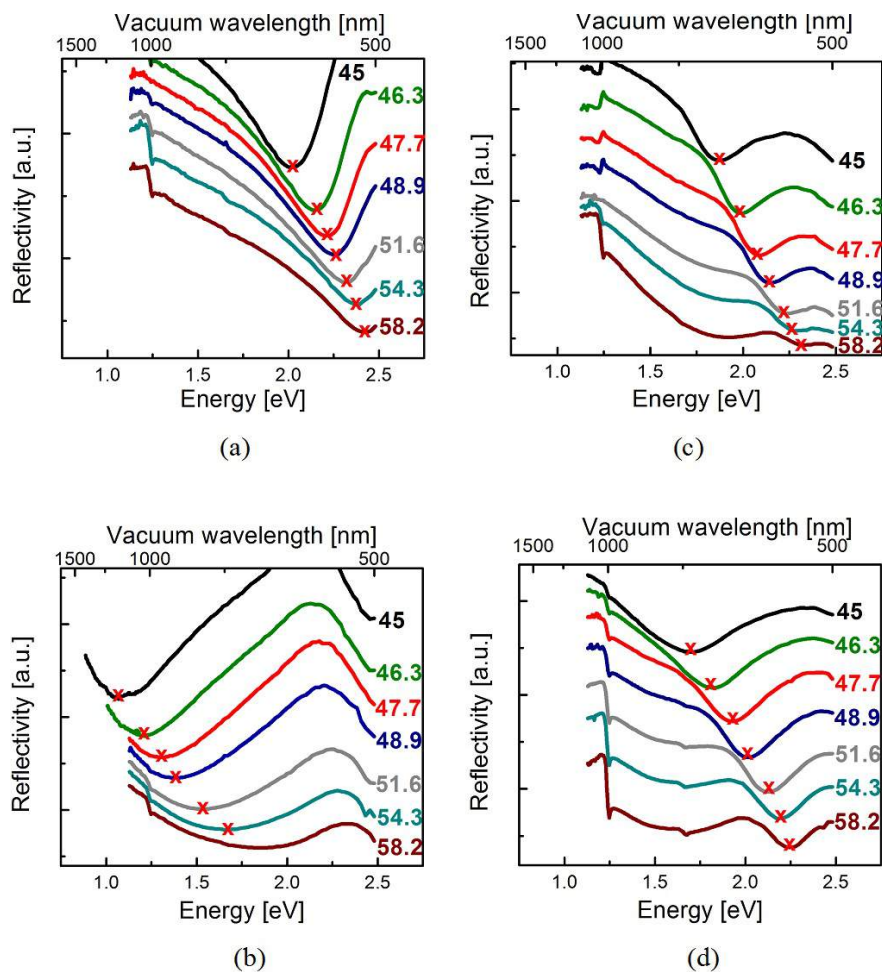


**Figure 2.19.:** Angular resolved reflectivity spectra in Kretschmann configuration. The plotted curves represent the ratio of p-polarized/s-polarized reflection for (a) bulk gold film (b) dealloyed nanoporous gold film (c) 30 nm hexaporous gold and (d) 55 nm hexaporous gold. The values of the angles of incidence in the glass are the same for all curves. A dip in reflection occurs, which shifts to shorter wavelengths with increasing angle of incidence (marked by the crosses). This indicates the resonant excitation of propagating surface plasmons.

triangles, etc.) and represent the experimentally mapped SP dispersion relation. A red shift of the surface plasmons at the same wave vector  $k_x$  or a corresponding increase of  $k_x$  at fixed surface plasmon frequency  $\omega$  was clearly observed.

Comparing the reflection curves for a fixed angle e.g.  $45^\circ$ , one observes that the dips for the dealloyed nanoporous gold ( $f = 0.5$ )- air interface are red shifted by  $0.85 \text{ eV}$  with respect to bulk gold-air interface. However, for lesser fill fractions of  $f = 0.2$  and  $0.3$

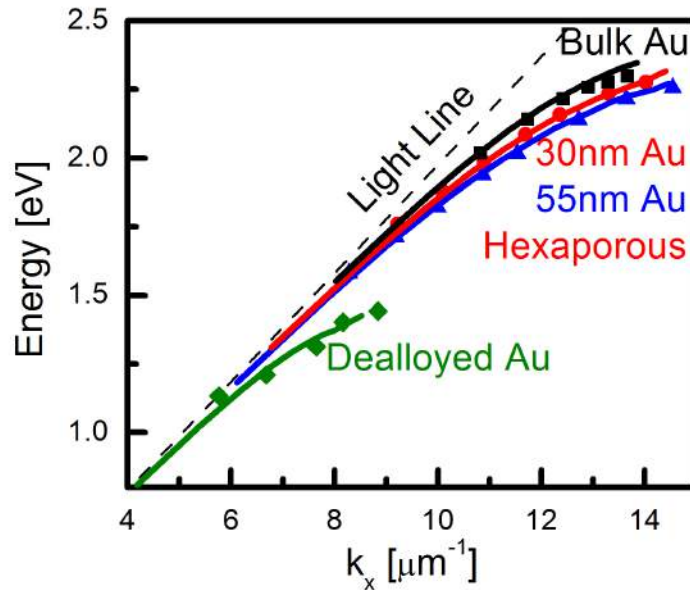


**Figure 2.20.:** Dispersion relation of bulk gold, dealloyed nanoporous gold, hexaporous 30 nm and 55 nm gold. The symbols show the experimental data and the continuous lines show the theoretically calculated data using effective medium theories. (Bruggeman model for bulk and dealloyed nanoporous gold and Maxwell-Garnett model for hexaporous gold).

for hexaporous gold, the shift is just around 0.2 eV. This confirms that by introducing nanoscopic porosity in the metal film, the SPs can be spectrally shifted towards longer wavelengths i.e. the near infrared region. To shift the SP on nanoporous gold-air interfaces even further to the near IR would require even larger porosities. However, this causes structural problems since it was already observed that for larger porosities (70 nm wide regular pores) the metal film partly disintegrates. In the next section these experimental data will be compared with effective medium calculations.

### 2.3.2. Theoretically derived SP dispersion relation from EMTs

The experimental shift in the dispersion relation (DR) is compared with theoretical calculations using effective dielectric constants for the nanoporous gold films. The dielectric constant of the nanoporous gold films is calculated using the tabulated optical constants for bulk gold from Johnson and Christie [58, 59]. First of all, for the calculation of the effective dielectric constant of nanoporous dealloyed gold, the Bruggeman (BG)

## 2. Propagating Surface Plasmons at Solid and Nanoporous Metal-Air Interface

---

effective medium theory was applied [44] as the dealloyed gold film is a random mixture of air pores in metal matrix. Afterwards, a thin film reflection model is setup up for  $d = 120 \text{ nm}$  thickness. Finally, by inserting the values of fill fraction  $f = 0.5$  for dealloyed nanoporous and operating the incident angle from  $42^\circ$  to  $60^\circ$  with a step size of  $1^\circ$ . The reflection modeling is carried out using MATLAB to plot the reflection curves for all angles of incidence. The code used here is given in appendix B.

To view the comparative trends of the reflection curves achieved from the dealloyed nanoporous gold theoretically are plotted in figure 2.21(a), which are compared with experimentally received reflectivity in figure 2.17. Both of the reflectivities show moving of dips towards higher energies with increasing angle of incidence. Furthermore, these theoretical dips are sharper for long wavelengths and lower angles of incidence, which weakens out for larger angles like in experiments.

Finally, for calculation of dispersion relation, the dips in the theoretical reflection curves are located and the corresponding  $k_x$  wave vector is plotted in the dispersion relation curve using the equation 2.24.

Similarly, for the highly ordered pores Maxwell-Garnett Model is used. Hexaporous gold films with pore sizes  $30 \text{ nm}$  and  $55 \text{ nm}$ , i.e.  $f = 0.2$  and  $0.3$  is inserted into the Maxwell-Garnett Model. A finite thickness of  $60 \text{ nm}$  is fixed to get the reflection curves (appendix B). Just as above, locating and plotting the calculated  $k_x$  wave vector by equation 2.24 is carried out to derive the final dispersion relation.

The theoretical dispersion relation for bulk gold is achieved by inserting  $f = 0$  in any of the above two models. Theoretically, both the Bruggeman model and Maxwell-Garnett model give same values of dispersion relation curve for bulk gold. The dispersion relation attained from theoretical calculations for bulk gold and all the nanoporous gold samples is shown in figure 2.20 as solid lines. These theoretical derived dispersion curves shows a good agreement with the experimentally determined dispersion data values shown as symbols in the figure.<sup>4</sup>

---

<sup>4</sup>The data obtained from experiments and theory is from dips in reflection curves. The smearing out i.e. flattening of the dips after certain angles for theoretical data aswell limits the plotting of data for dispersion relation curve.

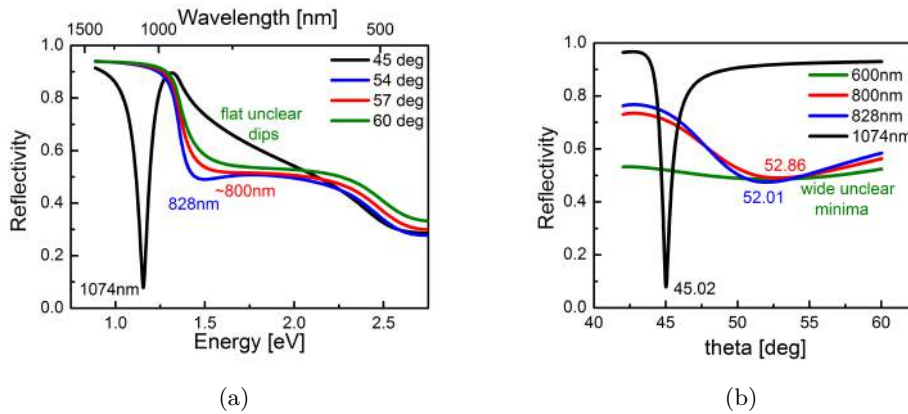


**Figure 2.21.:** Theoretically calculated reflectivity by two different methods: (a) Reflectivity vs wavelength graph for 45°, 54°, 57° and 60° angles of incidence and (b) Reflectivity vs theta at the wavelength minima obtained from graph (a).

### 2.3.2.1. Theoretically comparing reflectivity Vs. lambda (or energy) and reflectivity Vs. angle

There are two methods to determine the dispersion relation, the reflectivity vs theta and reflectivity vs lambda (or energy). As the former of the two is much widely used technique for fixed wavelengths of incoming light, so it is necessary to compare these two methods. Furthermore, the surface plasmons on metal/dielectric composite layers were already observed by Shi et al. [56] who have studied evaporated gold films of different grade of agglomeration. However, in their work, the surface plasmons were only excited for a single frequency and showed reflectivity vs theta graphs, while, this thesis, investigates the surface plasmon dispersion over a large range of frequencies from the near infrared to the visible using reflectivity vs energy (or lambda) graphs (figure 2.19). Therefore, a comparison between the two methods is necessary and feasible theoretically only. A comparison was made for dealloyed nanoporous gold under reflectivity vs lambda (or energy) and reflectivity vs theta.

The graphs shown in figure 2.21, represent theoretically calculated reflectivity curves for both methods. In figure 2.21(a), the angle is a fixed parameter and the reflectivity is calculated vs energy (like in the experiments). In figure 2.21(b), the wavelength is fixed (corresponding to the wavelengths of the minima in figure 2.21(a)) and the reflectivity for different angles is plotted. In figure 2.21(a), dips are seen for 45°, 54°, 57° (unclear wide dips) while for 60° no dips are visible. The wavelengths of the minima are at: 1074 nm

for  $45^\circ$ ,  $828\text{ nm}$  for  $54^\circ$ , and approximately  $800\text{ nm}$  for  $57^\circ$ . For higher angles no minima is observed. Similarly, clear dips are seen for reflectivity vs theta graphs at lower angle of incidence, which eventually become wider and flattens for higher angles.

Indeed, for long wavelengths and small angles (corresponding to low losses) a very good correspondence between, both measurement techniques can be found (dip for  $45^\circ$  yields  $1074\text{ nm}$  in figure 2.21(a) and  $1074\text{ nm}$  gives minimum at  $45.02\text{ deg}$  in figure 2.21(b)). For higher angles and shorter wavelengths, the methods are indeed not completely interchangeable any more (dip for  $54^\circ$  yields a minimum at  $828\text{ nm}$  in figure 2.21(a) while  $828\text{ nm}$  gives a minimum at  $52.01^\circ$ ). However, since the experimental evaluation was stopped, anyway, in the spectral range of flattening dips, the basis for the investigation of dispersion relation is only from the clearly visible minima. Due to this, the discussed range of measurement is well in the limits of correspondence of the two methods.

### 2.3.2.2. Comparison of dispersion relation obtained from experiments, theory and ellipsometry:

As we have the values of dielectric constants of bulk and dealloyed nanoporous gold, they (from figure 2.8) are used to calculate the reflectivity of the glass/film/air multilayer system for the different incidence angles. This method is used as a rechecking experimental tool for dispersion relation by inputting the dielectric constants received from section 2.2.1.1.1 in the MATLAB program in appendix B.

The theoretical SP dispersion is mapped from the resonance dips of the calculated reflection curves using the MATLAB program in appendix B and steps similar to as defined in section 2.3.2. This is the same way as the experimentally determined SP-dispersion was obtained. In this way, possible shifts due to the finite metal layer thickness are taken into account and the similar data evaluation (using the calculated reflection dips) ensures a good correspondence between the experimental, and theoretical results. Figure 2.22 shows the good agreement between the experimentally mapped dispersion (squares/triangles) and the theoretical data (lines) using the ellipsometric  $\varepsilon_m$  is quite good for the bulk gold film and still reasonable for the nanoporous gold film.

The dispersion relation determined by ellipsometric dielectric constants using MATLAB, the spectral range is limited to about  $1000\text{ nm} > \lambda > 800\text{ nm}$  for the theoretical dispersion curve of the nanoporous gold (solid red line in figure 2.22(a)). On one side, the effective index values from ellipsometry measurements are limited to the range  $1000\text{ nm} > \lambda > 372\text{ nm}$  which limits the calculations in the IR regime. On the other side,

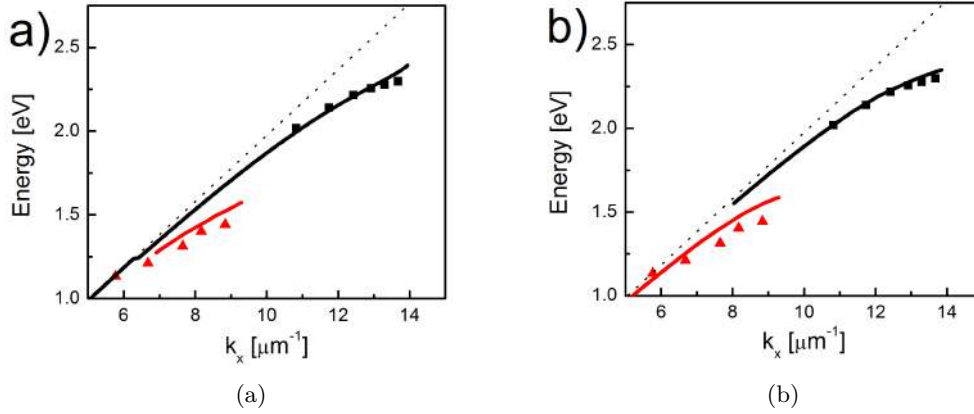


**Figure 2.22.:** Dispersion relation of propagating surface plasmons at the bulk gold film (black) and the dealloyed nanoporous gold film (red). Experimentally determined data are shown as symbols (squares or triangles), while dispersion curves determined from theoretical calculations are shown as lines. (a) For the theoretical calculations, the dielectric constants from the ellipsometric measurements are used from figure 2.8. (b) The theoretical calculations are based on effective dielectric constants determined by the Bruggeman formula.

the obtained reflection curves show a similar widening of the dips like the experimentally determined ones at higher angles (shorter wavelengths) (figure 2.17), inhibiting the determination of the theoretical dispersion curves for  $\lambda < 800 \text{ nm}$ .

It was already discussed that the ellipsometric data are almost independent of the thickness of the gold film when it surpasses  $100 \text{ nm}$  mark while comparing to experimental and theoretical data. Therefore, the contributions from the reflections at the buried gold-glass interface have a negligible impact on the dielectric constants of the gold layers determined by ellipsometry. However, the light has to penetrate the gold film coming from the glass side for the SP excitation. Direct impact on the efficiency of the surface plasmon excitation was observed with the scattering losses at the glass-gold interface and fluctuations in the film thickness (which appear in the original white gold leaves). These scattering losses and thickness variations can contribute considerably to a widening and flattening of the resonance dips [60] making it more difficult for the determination of an accurate minimum (especially for visible wavelengths). A rough surface (nanoporous gold films of this study) leads to a direct shift in the wave vector of the SP besides increased scattering [60] which can explain the remaining difference between the experimental and the theoretically derived SP dispersion.

### 2.3.3. Leakage radiation microscopy

The reflection measurements in Kretschmann configuration give only the dispersion relation of surface plasmons, which is determined by the real part of the SP wave vector  $Re(k_x)$  and the frequency  $\omega$  of the SPs. However, no information about the imaginary part of the SP wave vector ( $Im(k_x)$ ) is obtained. To experimentally determine this and also determine the propagation length of surface plasmons the leakage radiation microscopy setup as defined in section 2.2.2.2 is used. The propagation length of the SPP can be determined in two different ways by using the results from leakage radiation microscopy (LRM): firstly, by fitting an exponential decay to the SPP-intensity trail in the real image plane (IP), or secondly, by evaluating the width of the crescents in the Fourier plane (FP) which are the focus areas of the leakage radiation of the SPs.

#### 2.3.3.1. Real image plane

Firstly, the setup for the real image plane (IP) as shown in figure 2.16a is considered. The FIB milled sample is placed and a 780 nm laser is incident through it. The CCD camera records the real image as shown in figure 2.23(a). Intensity profiles along the central horizontal line are taken as a starting point i.e. at the central bright stripe, which indicates the excitation point of the SP at the slit. This profile is represented by the thin curves with the small markers in figure 2.23(a). An exponential decay fitting is used for each sample intensity profile. From these the decay lengths of the SPs are determined and yield  $L_{spp} = 9.0 \mu m, 5.6 \mu m, 3.7 \mu m$  and  $4.5 \mu m$  for bulk gold, 30 nm, 55 nm hexaporous gold, and dealloyed gold, respectively. The faster decay of the SPPs at the nanoporous gold surfaces is clearly connected with the larger losses for these SPs. These can mainly be assigned to increased radiative scattering losses due to surface roughness. Furthermore, the electronic oscillatory motion might already be damped by increased surface scattering of the electrons within the thin gold veins, increasing the ohmic losses of the nanoporous material which corresponds to the  $Im(\varepsilon_m)$ .

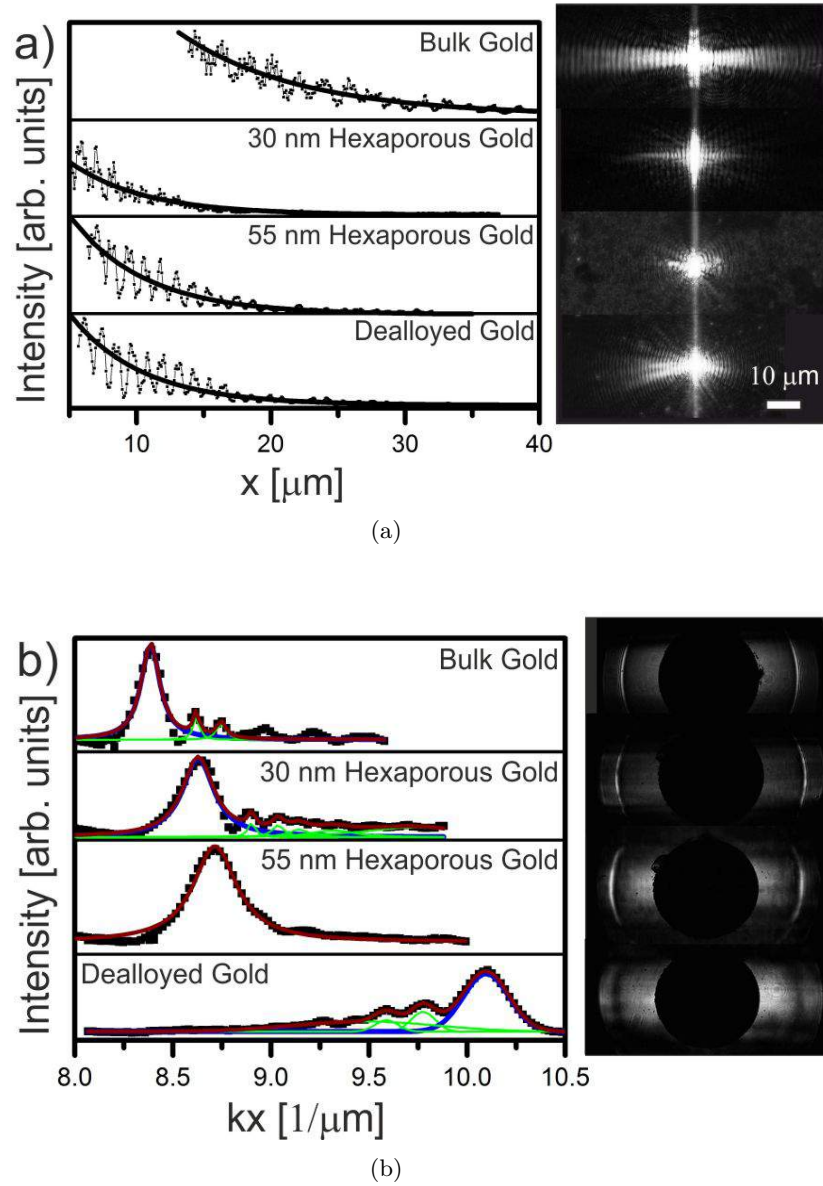


**Figure 2.23.:** Leakage radiation microscopy a) Real plane image and its data (symbols) fitted with exponential decay profiles (solid line) b) Fourier plane image and its corresponding intensity profile (symbol) fit with a system of Lorentzian peaks (solid lines).

### 2.3.3.2. Back focal plane or Fourier plane

As previously mentioned, the leakage radiation of the SPP forms crescents in the Fourier plane (FP). They are positioned on a circle with radius  $((k_x)_r)$  and their intensity profile can be fitted by a Lorentzian curve [9, 41] given as:

$$I = \frac{const.}{(K_x - (k_x)_r)^2 + (k_x)_i^2} \quad (2.25)$$

Here, the imaginary part of the surface plasmon wave vector  $((k_x)_i)$  determines the full width at half maximum of the Lorentzian  $\delta(k_x)_r = 2 (k_x)_i$ . Therefore, one can obtain:

$$L_{spp} = 1/\delta(k_x)_r \quad (2.26a)$$

$$L_{spp} = 1/2(k_x)_i \quad (2.26b)$$

Several smaller peaks are also observed in the intensity profile of the FP apart from the main Lorentzian peak of the crescent. These small peaks seem to be further artifacts of the measurements as their strength and appearance is influenced by the focusing of the laser on the slit. However, to obtain an accurate fit of the major peak, the overlap with the smaller peaks has been taken into consideration. Therefore, multiple Lorentzian were fitted to all the peaks, resulting in a unbiased representation of the experimental profile and obtained following values,  $L_{spp} = 8.8 \mu m, 5.2 \mu m, 3.5 \mu m$  and  $4.4 \mu m$  for bulk gold,  $30 nm, 55 nm$  hexaporous gold, and dealloyed gold, respectively from the full width at half maximum. A reasonable similarity to the results obtained from the exponential decays in the IP is observed (Table 2.3). The slight difference which is still present might be attributed due to the background scattered light. The radiative losses due to scattering on the surface roughness results in a considerable radiation background and lead to an overall increase in the observed radiation in the image plane. This can actually be seen as the strong halo of light around the beam block in figure 2.23(b). This radiation background can easily lead to a perceived longer decay (longer  $L_{spp}$ ) in the image plane. However, in the Fourier plane, the scattered radiation and the SPP light are separated, so that more realistic and true values for the SPP-decay length can be calculated using the FP profiles and fitting the Lorentzian peaks.

Finally, the real part of the SPP wave vector  $((k_x)_r)$  can be determined from the position of the maximum of the SPP signature in the FP. The positions of the crescents are obtained from the center values of the fitted Lorentzian peaks. Figure

**Table 2.3.:** Values of  $L_{spp}$  from LRM

| Image Plane | Bulk Au     | Dealloyed Au | 30 nm Hex Au | 55 nm Hex Au |
|-------------|-------------|--------------|--------------|--------------|
| Real        | $9.0 \mu m$ | $4.5 \mu m$  | $5.6 \mu m$  | $3.7 \mu m$  |
| Back Focal  | $8.8 \mu m$ | $4.4 \mu m$  | $5.2 \mu m$  | $3.5 \mu m$  |

**Table 2.4.:** Values of  $(k_x)_r$  from LRM and theoretical calculations

| Type   | Bulk Au          | Dealloyed Au      | 30 nm Hex Au     | 55 nm Hex Au     |
|--------|------------------|-------------------|------------------|------------------|
| LRM FP | $8.3 \mu m^{-1}$ | $10.1 \mu m^{-1}$ | $8.6 \mu m^{-1}$ | $8.7 \mu m^{-1}$ |
| EMT's  | $8.2 \mu m^{-1}$ | $9.03 \mu m^{-1}$ | $8.4 \mu m^{-1}$ | $8.4 \mu m^{-1}$ |

2.23(b) yields  $(k_x)_r = 8.3 \mu m^{-1}, 8.6 \mu m^{-1}, 8.7 \mu m^{-1}$  and  $10.1 \mu m^{-1}$  for the SPP wave vectors of the bulk gold, 30 nm, 55 nm hexaporous gold, and dealloyed gold, respectively. Although, a straight forward comparison with experimental data of the reflection measurements in Kretschmann configuration is impossible because reflection dips have not been recorded at the wavelength of 780 nm. But, theoretical SPP-wave vectors of  $8.2 \mu m^{-1}, 8.4 \mu m^{-1}, 8.4 \mu m^{-1}$  and  $9.03 \mu m^{-1}$  were obtained for the bulk gold, 30 nm, 55 nm hexaporous gold, and dealloyed gold, respectively, at  $\lambda = 780 nm$  by applying effective medium theory (Table 2.4). The theoretically determined dispersion curves show a good agreement with both, the reflection data and the specific LRM measurements at 780 nm for the bulk and ordered hexaporous gold samples. These results demonstrate clearly how the structure of the nanoporous gold and the level of porosity influence the SPP dispersion and propagation length.

Besides the overall exponential decay of the SP intensity during the propagation in figure 2.23(a), one can observe periodic intensity oscillations. These appear on top of the exponential decay and become more obvious in a detailed magnified section of the real images in figure 2.24. The cause of these oscillations is the interference of the SPP leakage radiation and the homogeneously scattered light which is collected by the numerical aperture (NA) of the objective. The possible oscillation periods for our microscope objective with a numerical aperture of 1.4 is calculated as  $\Lambda_l$  and  $\Lambda_s$  and are given as [61]:

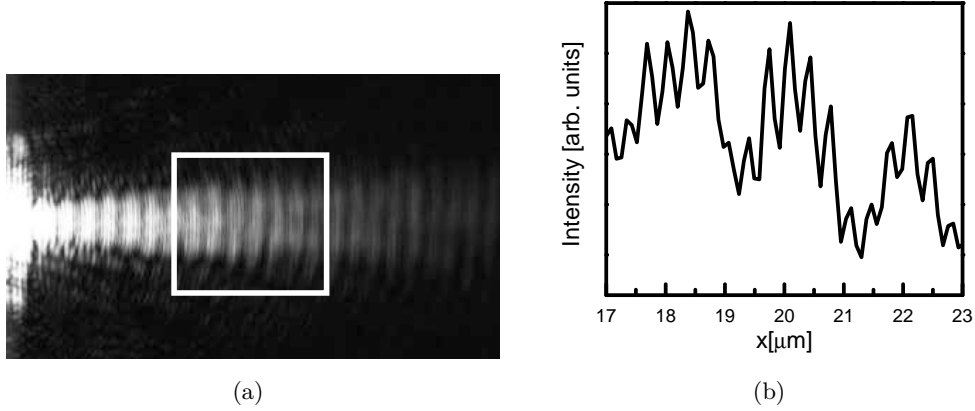


**Figure 2.24.:** Leakage radiation microscopy: Real plane image magnified view, (a) The magnified view of the intensity profile image and the corresponding (b) magnified exponential decay profile of bulk gold revealing the long and short range oscillations  $\Lambda_{l,s}$ .

**Table 2.5.:** Comparison of oscillation period with respect to Hohenau et al. [61]

| Periodicity | Experimental fitting | Hohenau et al. [61] |
|-------------|----------------------|---------------------|
| $\Lambda_l$ | $2.069 \mu m$        | $2.01 \mu m$        |
| $\Lambda_s$ | $0.3219 \mu m$       | $0.33 \mu m$        |

$$\Lambda_l = \frac{2\pi}{NA k_0 - k_{spp}} = 2.069 \mu m \quad (2.27a)$$

$$\Lambda_s = \frac{2\pi}{NA k_0 + k_{spp}} = 0.3219 \mu m \quad (2.27b)$$

One can clearly observe  $\Lambda_l$  from figure 2.23(a), while to observe  $\Lambda_s$ , a magnified view is required, shown in figure 2.24(a). When these values are compared with the oscillation periods for bulk gold values of  $2.01 \mu m$  and  $0.33 \mu m$  as determined in [61] for the similar wavelength of  $785 nm$ , they show a good agreement (as shown in table 2.5) with the equation 2.27. This confirms the interference effects as suggested by Hohenau et al. [61].

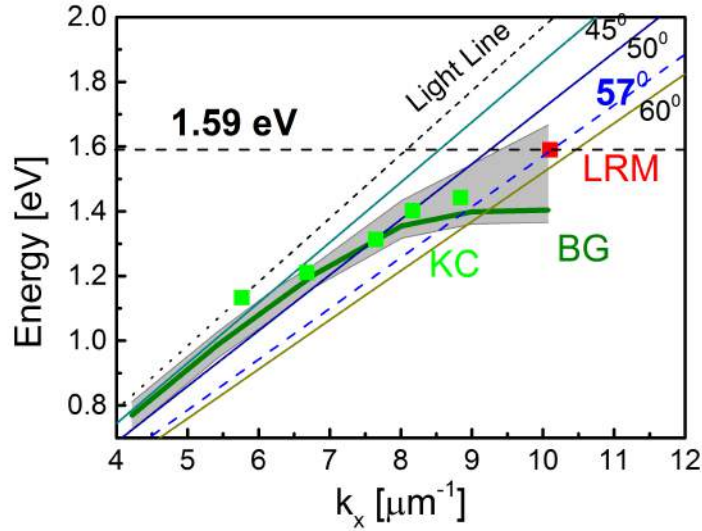


**Figure 2.25.:** Dispersion relation of dealloyed nanoporous gold from results of Kretschmann configuration (green squares), theoretical values (green line) and Leakage radiation microscopy (red point) value. The light line (41.83°) and (45°, 50°, 57° and 60°) angle lines are also shown. The gray area depicts the full width at half maxima of theoretically determined values of the dip.

#### 2.3.4. Comparison of wave vectors by two different experimental methods

Now, comparing the two experimental methods used for determination of wave vectors in this part, angular dependent reflection spectroscopy and leakage radiation microscopy (LRM). The LRM showed several advantages, as both the real and imaginary part of the SPP wave vector can be determined very precisely using the Fourier plane (FP) images. Furthermore, the observed FP features are reasonably sharp and it was possible to compare the results to that received from the real image, this allows a quick check for reliability of the method.

However, LRM has been used only for one specific laser wavelength, while a spectroscopic measurement covering a wide wavelength regime would require other light or tunable laser sources. This is the strength of the applied reflection spectroscopy in Kretschmann configuration which can be used to map the SPP dispersion relation (DR) within the whole near IR and visible spectral region. But the dips are very wide for spectra taken at fixed angular positions, which complicates the determination of the exact SPP resonances especially for SPPs experiencing higher losses i.e. wider resonances.

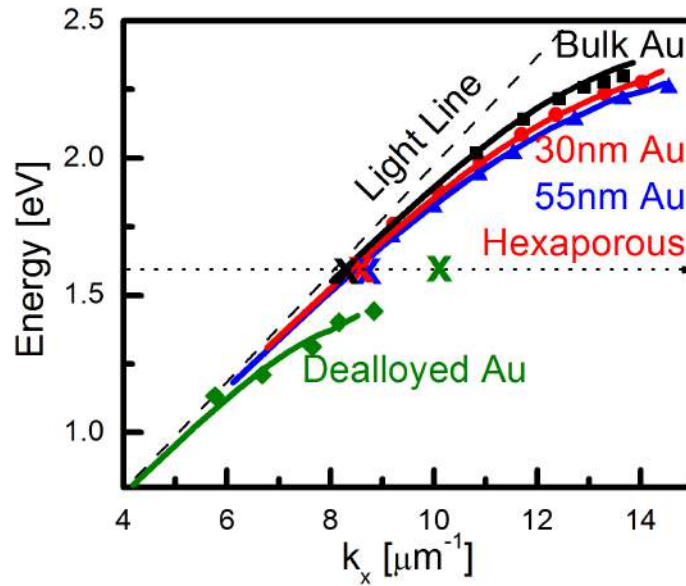


**Figure 2.26.:** Dispersion relation of bulk gold, dealloyed nanoporous gold, hexaporous 30 nm and 55 nm gold with LRM values (shown as crosses). It shows good correspondence between the two different experimental methods.

Now, zooming in the dispersion relation data of Kretschmann configuration from figure 2.20 and viewing only the dealloyed gold (figure 2.25) and also inserting the LRM data point ( $10.1 \mu\text{m}$ ,  $1.59 \text{ eV}$ ) shown as a red point in figure 2.25. The gray area in this figure is defined from the width of the reflectivity curves and plotting the values at the half width points on the both sides of the dips. The extended width of the dips is caused by the nature of the measurement and measuring the wavelength at a fixed angle ( $45^\circ$ ,  $50^\circ$ ,  $57^\circ$  and  $60^\circ$ ), meaning that one follows an inclined line similar to the light line and passing through the dispersion diagram, as shown in figure 2.25. This measuring line (blue dotted line at approx.  $57^\circ$ ) intersects the SPP dispersion curve under a small angle resulting in a long way through the resonance valley <sup>5</sup>.

The situation is different for the LRM which operates at a fixed frequency and basically cuts the dispersion curve along a horizontal line ( $1.59 \text{ eV}$ ) leading to a sharper, better defined resonance in the FP. Both these methods have their own limitations, but the

<sup>5</sup>The full width at half maximum of the dips similar to those shown in (figure 2.21(a)) are taken as values to plot the gray shaded area around the theoretically determined dispersion relation (green line). This gray shaded area shows the resonance valley of surface plasmons in figure 2.25. The resonance valley calculation is also limited by the flattening of the dips for higher angles and lower wavelengths, plus the range of calculation.

comparison can be successfully concluded by showing that both the methods lie well within the resonance valley of measurement, where one method follows an inclined line (blue dotted line at approx.  $57^\circ$ ) and other follows the horizontal line (at  $1.59\text{ eV}$ ). Both these lines intersect, hence the experimental data points lie well within a limited range of  $\pm 20\%$  to each other.

Furthermore, the figure 2.26 also shows a good match between all the experimental results received from the Kretschmann configuration (shown as symbols) in section 2.3.1, theoretical results (shown as lines) in section 2.3.2 and finally from section 2.3.3 (shown as crosses on line  $1.59\text{ eV}$ ). With all these results at hand, the next step of experimentation is to see the effect of plasmonic resonance on the luminescence of silicon.

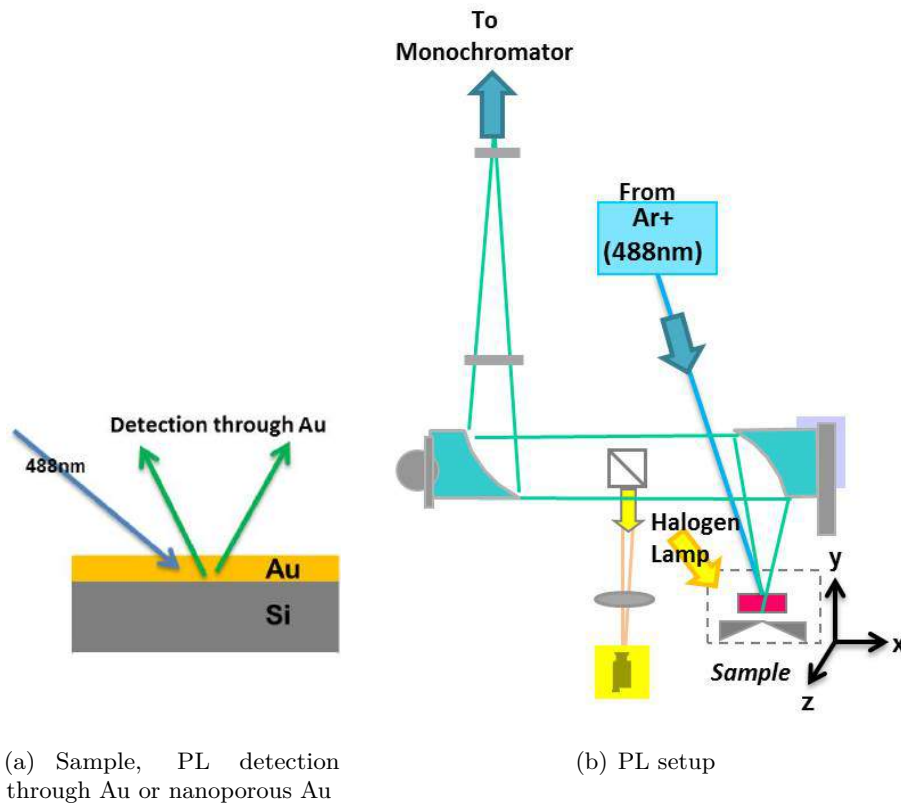


*Figure 2.27.: Sample detection through gold and PL setup*

### 2.3.5. Photoluminescence characterization

As a trial for viable Silicon applications, the samples produced by dealloying are used in contact with Si to see if any enhancement of luminescence of Si is achieved. This is a simple detection of Si photoluminescence through metal layer (figure 2.27(a)), where the incident laser comes through the gold onto the Si and the emission of Si passes through the metal layer for the detection.

#### 2.3.5.1. PL setup

An Ar-laser (488 nm) is used as the exciting laser for the Si samples. The laser falls on to the sample attached to a xyz-translation stage. A spot size of approx. 1 mm is focused onto the area of interest. The area can be viewed on a CCD camera when a halogen lamp light is incident onto the sample. When only the laser is incident, the light emitted from

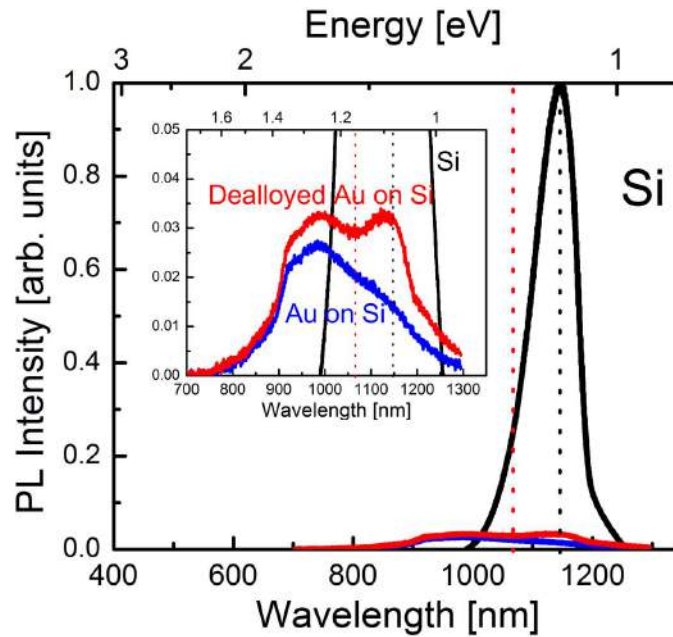


*Figure 2.28.: PL for Si, Au on Si and dealloyed nanoporous Au on Si.*

the sample propagates through a series of parabolic mirrors, lenses and apertures and enters the monochromator *SP2558* from Princeton Instruments. The detected intensity is finally plotted with respect to the wavelength.

The dealloyed nanoporous gold films were prepared in the similar way as explained in section 2.2.1 but in the final step, instead of lifting the sample on a glass substrate they are lifted by a two side polished  $500\ \mu\text{m}$  thick silicon substrate and left to dry at room temperature. For comparison a  $60\ \text{nm}$  solid gold film was deposited by thermal evaporation on the same kind of Si-sample. For these experiments, only bulk gold and dealloyed gold are considered, as the dispersion relation of dealloyed gold flattens around  $1.5\ \text{eV}$  which is nearest to the Si luminescence region. These samples are analyzed for Si photoluminescence (PL) and the results obtained are shown in figure 2.28.

The bulk silicon shown as a black curve, which has 25 times more PL intensity than Si with Au or  $60\ \text{min}$  dealloyed gold. But on a close inspection of the range of the PL curve, it is observed that the range of PL intensity of Si, which is from  $1050\ \text{nm}$  to  $1250\ \text{nm}$ , now increases to a range of  $800\ \text{nm}$  to  $1300\ \text{nm}$ , for Si with nanoporous dealloyed gold. One of the reasons for not seeing a discrete PL enhancement is surely the measurement of the PL through the gold layer. This layer absorbs a large part of the incoming laser

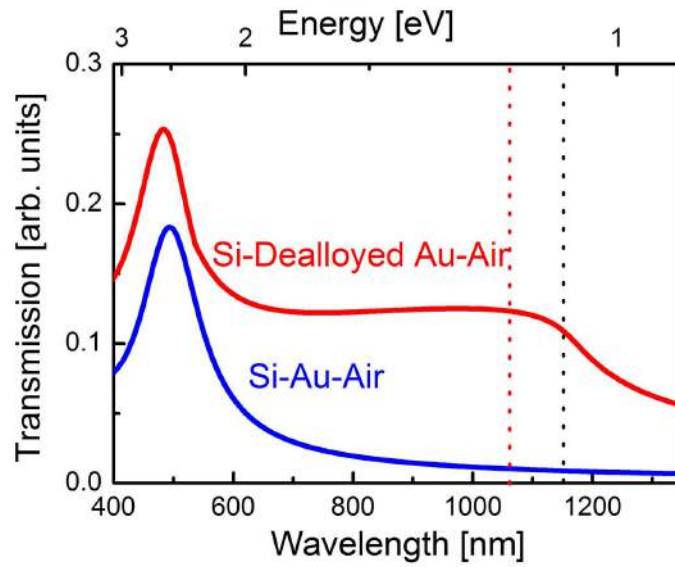


**Figure 2.29.:** Theoretically calculated simple first order transmission data of emission of Si passing through Au (blue) or dealloyed Au (red) into air.

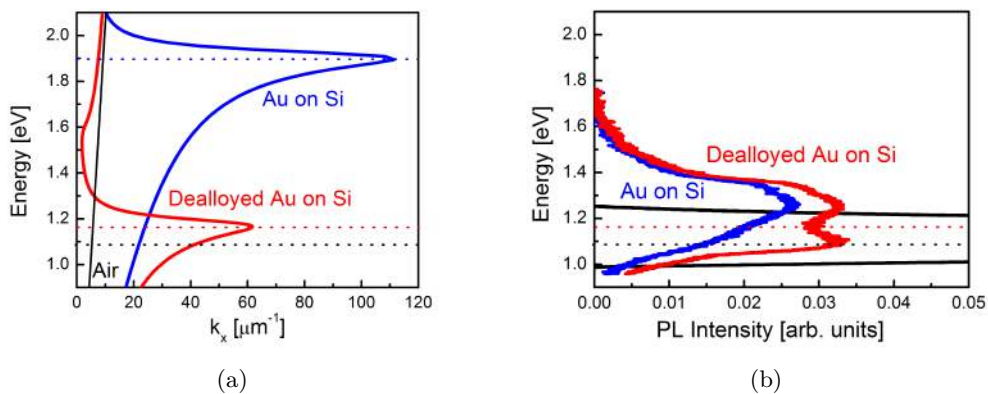


**Figure 2.30.:** (a) Theoretical dispersion relation for semi infinite layer of dealloyed nanoporous gold on Si, glass and air (b) Experimental PL result for Si, Bulk Au on Si and dealloyed nanoporous Au on Si. This shows a comparison between theoretical dispersion relation of SPs on dealloyed nanoporous Au on Si (red) with the experimental PL of dealloyed nanoporous Gold on Si (red).

light before it reaches the underlying silicon and also absorbs part of the Si emission lowering the overall detected PL intensity.

There are two noteworthy points which can be observed in the PL data (inset in figure 2.28):

1. The PL intensity through dealloyed Au on Si is higher than that of Au on Si.
2. There are two peaks for emission of Si through Dealloyed Au on Si but only one peak for the bulk Au on Si.

To investigate the possible reasons for these observations a transmission calculation for both gold layers is performed (figure 2.29). For bulk Au, the theoretical calculation is shown as a blue curve in figure 2.29 and that for dealloyed porous gold layer is shown as a red curve. The comparison shows a higher transmission through delloyed gold with respect to the bulk gold. This can be expected due to the overall porous nature of the dealloyed film and it explains the overall higher transmission of the detected PL signal from the dealloyed Au/Si sample compared with the bulk Au/Si samples as seen experimentally in the inset of figure 2.28.

Now, to consider the effect of a possible SP- mediated luminescence enhancement from the bulk Au - Si and dealloyed Au - Si interface, the theoretically determined dispersion curves for the SPs at the two different interfaces (figure 2.30(a)) will be compared with the PL spectra in (figure 2.30(b)). The dispersion of the SP on the bulk Au - Si interface shows the usual SP dispersion within the whole range of the Si luminescence. Its limiting frequency  $\omega_{sp}$  appears at  $1.9 eV$  and a considerable flattening of the bulk Au - Si SP dispersion only happens for energies above  $1.7 eV$ . This means that in the range of the Si luminescence the photonic density of states of these SPs is still small and an enhanced emission is not expected. From this perspective it is surprising that around  $1.3 eV$  the luminescence of the bulk Au - Si sample is larger than the usual luminescence from an uncovered Si sample. It would be normal to wonder if there is still an impact of the confined surface plasmon fields near the interface? This higher emission around  $1.3 eV$  is also observed for the dealloyed Au/Si-sample so that the same cause might be suspected. At the moment it is not clear what the reason for this luminescence at  $1.3 eV$  is. It might be speculated that at the Au - Si interface some Au diffuses into Si and might form a thin layer of gold silicide. However the samples were not heated after the deposition of the gold films and also a corresponding luminescence from AuSi compounds was not found in literature, so that the source for this luminescence peak at  $1.3 eV$  remains unclear.

Considering the case of the dealloyed Au sample, a small dip in PL-signal appears at  $1.16 eV$  and a second peak at  $1.1 eV$  is also obvious -both features are absent for the bulk Au/Si emission. The dotted line (red) indicate that the small dip coincides with the “bending back” of the dispersion relation of the SP at the dealloyed Au - Si interface.

Maybe the large absorption of the large  $k_x$  SPs at this wavelengths causes this reduced emission. However of larger interest is the origin of the second peak at 1.1 eV. Maybe it indicates a slight enhancement of luminescence because of the flat dispersion of the corresponding SP dispersion relation. This would mean that the higher photonic density of states lead to an increased emission of SPs which travel at the interface. However, since the dealloyed gold film has a considerable roughness the SP can be coupled out as light. In the former chapters, this large scattering losses of the nanoporous films were already observed. However, a comparison of the exact position of the luminescence peak of the dealloyed Au sample with the luminescence of the free Si-wafer shows that the luminescence peaks appear at the same wavelength. So it might be true that the usual peak of silicon luminescence just appears additionally for the dealloyed Au sample since the transmission of this nanoporous layer is higher resulting in a “pushing through” of the usual Si emission profile. Therefore, from the current data a luminescence enhancement due to SP coupling can not be safely concluded. Further experiments might be necessary e.g. by measuring the Si luminescence through a thin Si layer which is covered by the gold films on the opposite side. However this was not attempted here and is more difficult to achieve experimentally.

Furthermore it has to be considered that, although the red shift of dispersion relation is shown and the concept of nanoporous metals works in principle, the porosity of the dealloyed gold is not high enough to shift  $\omega_{sp}$  further into the near infra red region. This would require higher porosities, but corresponding samples broke down due to their fragile nature. To shift the SPs further into the near IR and observe enhanced luminescence there, a search for alternative plasmonic structure and emitters is required.

## 2.4. Summary of Part I

In this part of the thesis, the set of experiments and analysis of different types of nanoporous gold films (with random and ordered nanoporosity) have been carried out. Introducing a nanoporosity with structural sizes well below the wavelength of light creates a “meta-metal” with an effective dielectric constant leading to a distinct red shift of its SP dispersion relation. Reflection spectroscopy in Kretschmann configuration has revealed a substantial red shift with respect to its bulk counterpart, especially for porosity  $f = 0.5$ , a red shift of approx.  $0.85 \text{ eV}$  has been observed.

These results have been found to be in good agreement with theoretical predictions based on effective medium models for the nanoporous films. Bruggeman model has fit well to the random, disordered and bi-continuous dealloyed nanoporous gold. Whereas, Maxwell-Garnett model has fit well with the hexagonally ordered nanoporous gold. These results indicate that the frequency and wave vector of surface plasmons can be tuned effectively even for a fixed adjacent dielectric material by adjusting the porosity of the metal layer.

Additionally, leakage radiation analysis has been used to determine SPP propagation lengths on the order of  $4 - 5 \mu\text{m}$  for the nanoporous samples. The results demonstrate that a control of the metal permittivity and the connected surface plasmon dispersion relation is, in principle, possible by introducing a nanoporosity. The observed SPPs, therefore, represent designer plasmons in the visible and near infrared spectral region. The price for this flexibility are increased scattering losses due to the surface roughness and electron surface scattering in small metallic veins in the material.

When these nanoporous films were brought into contact with Si, with the aim to observe a possible luminescence enhancement of Si since the SP at the nanoporous Au - Si interface was predicted to have its limiting frequency  $\omega_{sp}$  within the spectral range of Si-emission which is connected with a low group velocity and a high photonic density of photonic states. However, the Photoluminescence measurements did not show an unambiguous proof for this. Although the demonstration of surface plasmon supported luminescence enhancement in the near IR was not yet successful, it can be concluded that the basic principle to achieve designer plasmons on nanoporous metal films for the near IR has been successfully implemented.

A further shift of the plasmon dispersion towards the IR requires larger porosities, which could not be realized with the investigated structures due to their increased fragility. So,

## 2. Propagating Surface Plasmons at Solid and Nanoporous Metal-Air Interface

---

in the next part of the thesis, a possibility of creating structures supporting localized surface plasmons at even longer wavelengths is discussed. To study possible luminescence enhancement for  $\lambda > 1200 \text{ nm}$  also an alternative emitter material has been used.

---

Papers published from this part:

1. N. Sardana, T. Birr, S. Schlenker, C. Reinhardt and J. Schilling; Surface plasmons on ordered and bicontinuous spongy nanoporous gold; *New Journal of Physics*, 16 (6) (2014), 063053.
2. N. Sardana, F. Heyroth and J. Schilling; Propagating surface plasmons on nanoporous gold; *Journal of the Optical Society of America B* 29 (7) (2012) 1778-1783.

## **PART II**

### **Localized surface plasmons on metal nanoantenna arrays**

## 3. Localized Surface Plasmons on Metal Nanoantenna Arrays

The field of nonlinear optics and the possibility to enhance absorption or emission in small volumes has been greatly influenced by high optical confinement and local field enhancement of the localized surface plasmons resonances (LSPR) occurring at metal nanoparticles, nanostructures or nanoantennas [5, 10, 18, 62–66]. Due to this important LSPR property of metallic nanoantennas, they have been widely studied but mainly as single nanoantennas or two interacting nanoantennas. Further, as an extension to the interaction between the two adjacent antennas, the few studies have also focused on large arrays of nanoantennas, where, the array coupling leads to a new grating effect, which has been studied in the visible regime [67, 68] only for square periodicities but no systematic study of parameter variations has been carried out. In this part of the thesis, a systematic investigation for the effect of multiple scattering among regularly arranged metal nanoantennas along with the resulting enhancement of light emission from quantum dots placed in their vicinity has been pursued.

In consonance with the thesis topic, this part also aims to tailor/shift the SP resonance to the near infra red (NIR) (specifically  $> 1.2\mu m$ ), in order to exploit the possibility of field enhancement. In next section, the theory of single particle extinction (Mie theory) is reviewed for longer particles. Particle plasmonics is known to shift with length in IR region, so, in this section, an array of such particles is created and a theory with Hertzian dipole approximation is presented. This theory is followed by the experimental results which are discussed viz-a-viz contemporary literature and basic theoretical calculations.

### 3.1. Theoretical background

A single metallic nanoparticle or nanoantenna supports localized surface plasmon resonance. Furthermore, an individual plasmonic nanoantenna placed in an external electromagnetic field can also be described as a dipole charge oscillator (Fröhlich mode <sup>1</sup>) [69]

---

<sup>1</sup>Fröhlich emphasized the lossless transmission of energy from one mode to another mode. He described a model of a system of coupled molecular oscillators supplied with energy at a constant rate. When

or electric dipole with a resonance frequency which is determined by the antenna size and shape. A single metallic nanoantenna which is symmetric in all directions i.e. spherical in shape is taken as the starting point for calculation using the Maxwell's equation by Mie theory [40, 70].

### 3.1.1. Calculation of extinction for spherical Au nanoantennas embedded in $n = 1.5$ by Mie theory

From Maxwell's equations, a solution for the response of a single dielectric sphere placed in an external electromagnetic field can be derived. Specifically, for an uncharged spherical dielectric sphere placed in a homogeneous medium, an analytical solution was given by Mie [45, 71]. The degree to which a sphere can scatter or absorb electromagnetic radiation is described through its extinction cross section  $\sigma_{ext}$ . The cross section ( $\sigma$ ) represents an apparent area, which is used to describe the amount by which the radiation interacts with the sphere ( $\sigma$  usually does not correspond to its geometric cross section). When the sphere is illuminated by a plane wave (power density  $P_i$ ), it scatters and absorbs a portion of the wave. The radiation scattered or absorbed is detected at location defined by  $\theta$  and  $\phi$  with respect to the waves propagation vector (power density of detection  $P_r$ ) [40, 45, 72, 73]. Assuming that the metal sphere has scattered the incident electromagnetic radiation, then the cross section  $\sigma$  can be directly calculated using:

$$\sigma(\theta, \phi) = 4 \pi r^2 \frac{P_r(\theta, \phi)}{P_i} \quad (3.1)$$

where,  $r$  is the distance between detection location and the sphere.

Three different cross sections can be distinguished: scattering cross section  $\sigma_{sca} = S$ , the absorption cross section  $\sigma_{abs} = A$  and the extinction cross section  $\sigma_{ext}$ . Where, extinction cross section is always the sum of absorption and scattering cross sections, as shown in equation 3.2:

$$\sigma_{ext} = \sigma_{sca} + \sigma_{abs} = S + A \quad (3.2)$$

Furthermore, Mie showed that for spherical particles a solution could be obtained in terms of an infinite series of electric and magnetic multipoles (to simplify the calculations, in this thesis, the magnetic modes have not been considered), which on solving give

---

this rate exceeds a certain threshold, then it leads to condensation of the whole system of oscillators takes place into one giant dipole mode (similar to Bose-Einstein condensation). A coherent, nonlocal order emerges and this effect takes place far from equilibrium. Fröhlich coherence is in that sense related to the principles underlying the laser (another pumped, coherent system).

the so called the Mie coefficients [45, 71]. These Mie coefficients can be further used to calculate the extinction, absorption and scattering cross sections or the electromagnetic fields inside and outside of the spherical particle. For the details of derivations, reader is referred to [45, 71].

In this thesis, the Mie-formalism is carried out for gold. For initial estimation, three different spherical particle diameters,  $150\text{ nm}$ ,  $250\text{ nm}$  and  $350\text{ nm}$  are considered. The corresponding extinction is a sum of contributions from different absorption and scattering modes (equation 3.2). These values were calculated using the MATLAB program and MNPBEM toolbox for plasmonic nanoparticles given by Truegler and Hohenester et al.[73, 74], which is based on calculations shown by Bohren and Huffman [45]. The estimated cross sections are shown in figure 3.1. The spectra demonstrate the contributions for both absorption ( $A_m$ ) and scattering ( $S_m$ ) for dipole and quadrupole resonances for  $m = 1$  and  $2$ , respectively. From these figures, one can see that absorption becomes important in the spectral regime below  $500\text{ nm}$ . This is connected with the interband (d-band) transitions of Au that start at these energies. At longer wavelengths, the contributions of the dipole mode dominate the scattering cross section spreading well into the infrared, while the scattering due to the quadrupole mode becomes only noticeable at shorter wavelengths in the visible regime. In general, a red shift of the scattering peaks of the different modes is observed as the particle size increases which also governs the extinction cross section. For particles (nanoantenna) with  $250\text{ nm}$  diameter a well separated dipolar contribution dominates in the near-IR, which is the region of interest for the experiments in this thesis. The impact of any higher order modes (quadrupole, octopole, etc.) can therefore be neglected for these particles in the near IR region i.e. between  $1000\text{ nm}$  to  $1500\text{ nm}$ .

#### 3.1.2. Plasmonic nanoantennas arranged in a regular array

To gain an understanding of the collective phenomena in nanoantenna array, each plasmonic nanoantenna can be approximated as, a Hertzian dipole having an electric and magnetic field around it. Let us first consider, a Hertz diopole antenna oriented along the z-axis having a length  $dl$  and current  $I_0 e^{j\omega t}$ , in the spherical coordinate system  $(r, \theta, \phi)$ . The magnetic field loops along z-axis and has only a  $\phi$  component, whereas the electric

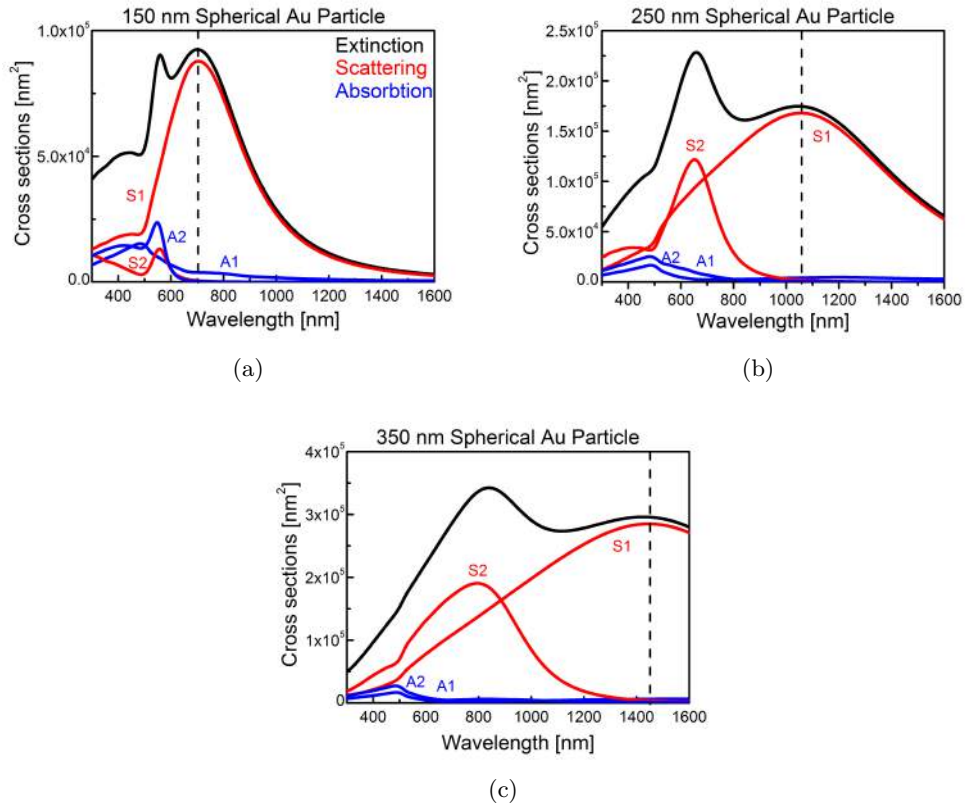


**Figure 3.1.:** Extinction cross sections of Au sphere with diameters: (a) 150 nm (b) 250 nm and (c) 350 nm. The spectra is further decomposed into contributions from absorption and scattering cross section with the dipole and quadrupole modes.

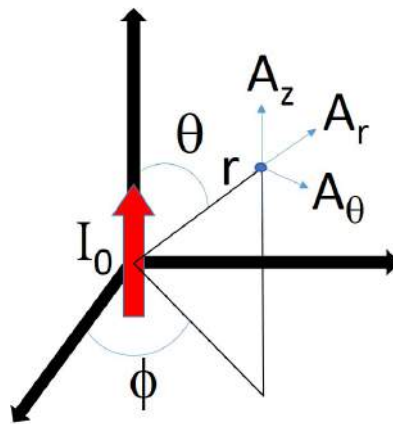


**Figure 3.2.:** Hertz dipole and its influence at a point  $(r, \theta, \phi)$  defined in spherical coordinate system.

field has both  $r$  and  $\theta$  components (which are more important for this thesis) and are given as [75–79]:

$$E_r = \frac{I_0 dl \cos\theta e^{(j\omega t - j\beta r)}}{4\pi\omega\varepsilon} \left( \frac{\beta}{r^2} - \frac{j}{r^3} \right) \quad (3.3a)$$

$$E_\theta = \frac{I_0 dl \sin\theta e^{(j\omega t - j\beta r)}}{4\pi\omega\varepsilon} \left( \frac{j\beta^2}{r} + \frac{\beta}{r^2} - \frac{j}{r^3} \right) \quad (3.3b)$$

Where, the  $\phi$  component of the electric field is zero. These equations comprise of different fields which vary with  $1/r^3$ ,  $1/r^2$  and  $1/r$ . These are defined as follows [45, 80]:

1. The field which varies as  $1/r^3$ , is the electrostatic field. This field is dominant in the close vicinity of the dipole since its amplitude decreases rapidly as function of distance. The electrostatic field is inversely proportional to the frequency. As the frequency of the current approaches zero, this field diverges to infinity. This field is essentially due to the accumulation of charges on the tip of the antenna and the field acquires its maximum at the tips of the dipole with a polarisation along the z-axis ( $\theta=0$ ).
2. The induction field varies as  $1/r^2$ . This field extends little further than the electrostatic field but still decays rapidly as a function of distance. The induction field is independent of frequency. This field has same behavior as the magnetic field obtained from the Biot-Savart law.
3. Finally the third, radiation field varying as  $1/r$ , extends over farthest distance from the antenna and is responsible for the radiation of power from the antenna. The radiation field is proportional to the frequency. This field is therefore practically absent at low frequencies. This field is essentially a high frequency phenomenon.

The electrostatic and the induction fields together are called the *nearfields*, and the radiation fields are called the *farfields*. The three field become equal in magnitude at a distance of  $1/\beta = \lambda/2\pi = \lambda/6$ . The distance within  $\lambda/6$  is called the near-field zone and the distance  $\gg \lambda/6$  is called the far-field zone. In the near-field coupling, there are two modes, the symmetric and asymmetric modes which are discussed in the section that follows.

#### 3.1.2.1. Near-field coupling

When two nanoantennas are in vicinity of each other, the dipole field of one nanoantenna is influenced by the neighboring nanoantenna. This influence depends on the size and

shape of the nanoantennas interacting and also the distance between them. When there are multiple nanoantennas arranged in a regular array, the individual antenna behavior is modified by local electric fields that are generated due to the array. Many theoretical and experimental results have been published in literature that investigate array behavior of particles in arrays. The two major effects of arrays that have been predicted and observed were: The red or blue shift of the particle resonance due to the presence of neighboring particles [68, 81–83] and the collective behavior of the particle array as a grating, and its effect [65, 67, 84–87]. Both these factors depend on the polarization of incident light and array i.e. particle arrangement.

Considering the excitation of the antennas with a plane wave at normal incidence, there are two existent symmetric modes which can be excited by the external electric field. To explain the coupling between neighboring particles especially in the near-field region (quasi-static approximation is valid), let's consider two nanoantennas placed in an electric (E) field along y-axis. Each nanoantenna acts as a dipole with field distributions (figure 3.3) resonating along the direction of E-field in y-direction. Considering two arrangements of the adjacent placement of nanoantennas [88–91]:

1. First considering the effect of antennas arranged in series and aligned along the y-direction (figure 3.3(a)) (head-to-tail configuration). Both nanoantennas have similar field distribution and in the same direction. If the electron cloud is displaced, then the restoring force depends directly on the field inside the antenna. Since, the field of one antenna enhances the field inside the other antenna, the restoring force is increased and hence resulting in a red shift of resonance frequency [85, 88].
2. Now, considering the effect of antennas arranged next to each other (side-by-side configuration), as shown in figure 3.3(b). The external field from one, opposes the internal field of the other. Therefore, reduction in inside field results in increasing resonance frequency i.e. blue shift.

Similarly, when the distance between the antennas increases, the influence of one antenna on its neighbor antenna reduces. Hence, the deviation of the antennas resonance frequency from its individual resonance frequency changes, as explained above, depending on the arrangement of antennas [65, 88].

The near field coupling discussed till now is the symmetric mode excitation, in which the dipoles are in same direction and can be excited by a plane wave at normal incidence. This symmetric near field is minimum in the direction  $\theta = \pi/2$  and maximum in the directions  $\theta = 0, \pi$ . However, along no direction the near field is zero. The near field

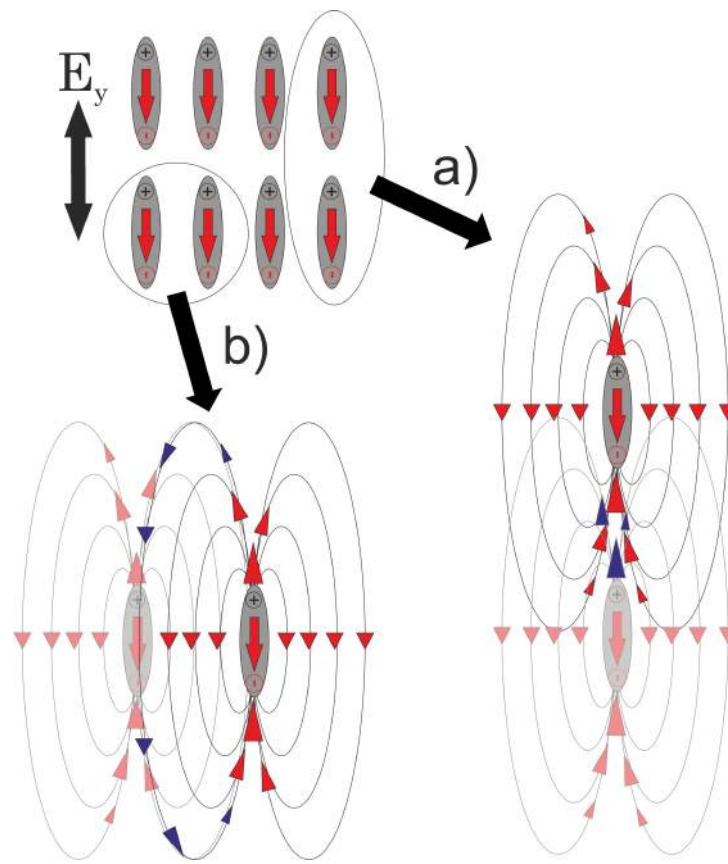


**Figure 3.3.:** *Interacting dipoles activated by light polarized along  $y$ -axis ( $E_y$ ). The interacting antennas (a) stacked in  $y$ -direction and (b) stacked in  $x$ -direction are shown [88].*

essentially stores the electromagnetic energy around the dipole but does not contribute to the power flow from the antenna. Whereas, the other mode i.e. asymmetric mode, is existent when the dipoles are in opposite direction. Such a dipole arrangement, cannot be excited by a plane wave at normal incidence. An oblique incidence would be necessary to introduce a phase difference between neighboring antennas, which would then partially excite the asymmetric modes.

### 3.1.2.2. Far-field coupling

When distances are  $\gg \lambda/6$ , the dipole field is in the far-field zone. In this zone, only the radiation field is prominent.

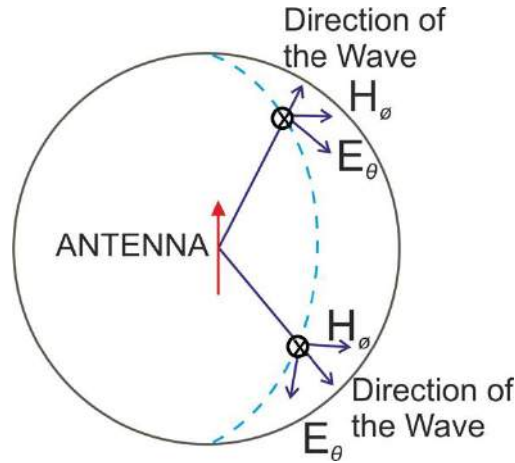


**Figure 3.4.:** Hertz dipole radiation directions, showing the spherical nature of far-field transverse electromagnetic waves.

The far field components of the electric and magnetic fields of a Hertzian dipole are given as [75–79]:

$$E_{\theta} = \frac{j I_0 dl \beta^2 \sin\theta e^{(j\omega t - j\beta r)}}{4 \pi \omega \epsilon r} \quad (3.4a)$$

$$H_{\phi} = \frac{j I_0 dl \beta \sin\theta e^{(j\omega t - j\beta r)}}{4 \pi r} \quad (3.4b)$$

This radiation or far field equations show that the electric and magnetic fields are proportional to the rate of change of current or acceleration of charges. Looking at the directionalities, the wave travelling radially outwards results in the electric field which is polarised in  $\theta$  direction and the magnetic field in the  $\phi$  direction i.e. they are perpendicular to each other forming a transverse electromagnetic wave, as shown in figure 3.4. Finally, these fields are not uniform in all directions. It has a maximum along  $\theta = \pi/2$  and zero along  $\theta = 0, \pi$ . Hence, the hertz dipole does not have any radiation along its axis.

### 3.1.3. State of the Art

Since the past two decades, a lot of work, both theoretical and experimental, is being done for the local field enhancement by the localized surface plasmons resonances (LSPR) occurring at metal nanoparticles, nanostructures and nanoantennas [5, 10, 18, 62–66]. When these nanoparticles or nanoantennas are arranged in an array, they cover large

### 3. Localized Surface Plasmons on Metal Nanoantenna Arrays

---

areas on the substrate and show resonance effects which arise not only because of their shape but also due to their array/grating arrangement (i.e. Fano like resonances). These large arrays of nanoantennas have been studied for circular and rectangular nanoantennas arranged in a square lattice where their resonances occur mainly in the visible regime [67, 68]. No systematic study of parameter variations has been carried out yet. So, here, a systematic study of effect of changes in size, elongation and periodicities is carried out with the aim to shift the Fano-like resonance in the near infra red regime.

## 3.2. Fabrication and structural characterization of nanoantennas

To shift the extinction maxima (Mie resonances) to the spectral region of  $1000 - 1500 \text{ nm}$ , the Mie theory predicts that spheres with a diameter in the range of  $250 \text{ nm}$  are sufficient. To fabricate such a regular array of nanoparticles e-beam lithography and a lift off process is used after gold deposition. Due to this processing technique, the resulting structures are not really spheres but at best circular disks having a fixed diameter and height. So, disks of  $250 \text{ nm}$  diameter and  $50 \text{ nm}$  height are considered here as a starting point for experiments.

Nanoantennas are written on a glass substrate (extra white glass  $24 \text{ mm} \times 24 \text{ mm} \times 1 \text{ mm}$  (length  $\times$  width  $\times$  height)). The glass is cleaned in ultrasonic bath with acetone for  $2 \text{ mins}$  and then in isopropanol for  $2 \text{ mins}$ . A first layer,  $600 \text{ k}$  PMMA (AR-P 669.04 from ALLRESIST GmbH) is spin coated at  $5000 \text{ rpm}$  for  $90 \text{ s}$ . Baking of this layer is carried out for  $1 \text{ hr}$  at  $200^\circ\text{C}$ . The sample is then cooled down to room temperature and a second layer of  $950 \text{ k}$  PMMA (AR-P 679.03) is spin coated with same parameters as before and baked again at  $180^\circ\text{C}$  for  $1 \text{ hr}$ . The sample is cooled down to room temperature. After this, the samples surface is made conductive (to avoid charging during e-beam lithography) with a layer of *SX AR - PC* 5000/90.2, spin coated at  $2500 \text{ rpm}$  for  $90 \text{ s}$ . Finally, this coated sample is baked at  $105^\circ\text{C}$  for  $5 \text{ mins}$ .

Now, this sample is processed by electron-beam lithography in the RAITH PIONEER system. The structures are written with an acceleration voltage of  $30 \text{ kV}$ , a beam current of  $150 \text{ pA}$  and an area dose between  $1000$  and  $1500 \mu\text{C}/\text{cm}^2$  depending of the structure sizes. Nanoantennas of the same geometry were produced each in an area of  $300 \mu\text{m} \times 300 \mu\text{m}$ . After removing the conducting layer with water and developing for  $1 \text{ min}$  in isopropanol;  $50 \text{ nm}$  Au layer with  $2 - 3 \text{ nm}$  Cr as interlayer are deposited in a thermal e-beam evaporator onto the sample. Finally, the remaining photoresist is removed by acetone and sample is ready for measurement<sup>2</sup>.

A  $2 - 3 \text{ nm}$  Cr adhesion layer between glass and Au antennas, does not affect the localized surface plasmon resonance noticeably [67]. The light optical microscope image of the sample are shown in the figure 3.6.

To understand the cause of the sharp features that are predicted in literature [67, 68] and their dependency on different parameters, it is very important to separate the correlated

---

<sup>2</sup>All of this processing has been done with help of Dr. Frank Heyroth in collaboration with IZM, Halle.

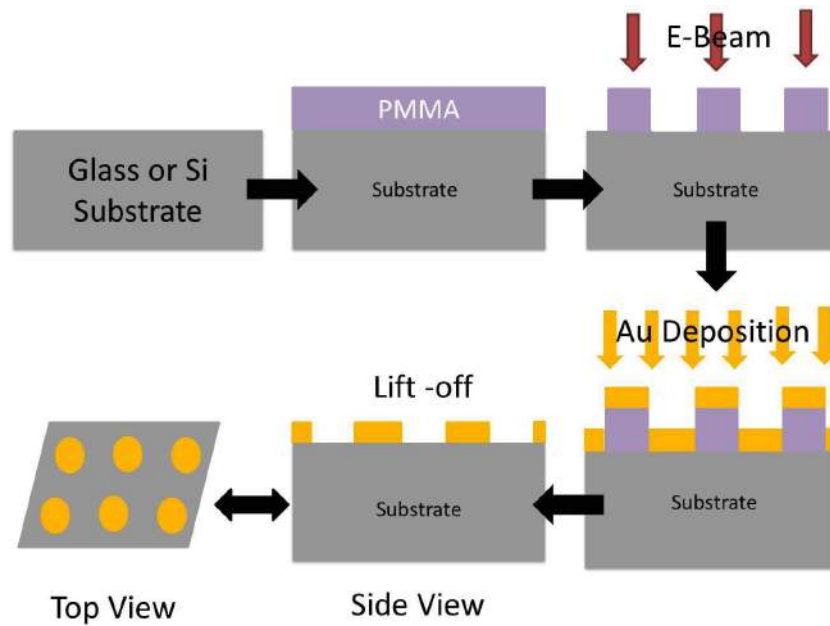


**Figure 3.5.:** Schematic of sample preparation on glass substrate. The process steps include the PMMA processing layer (all steps explained in corresponding text), e-beam lithography, Au deposition and lift off process to get nanoantennas.

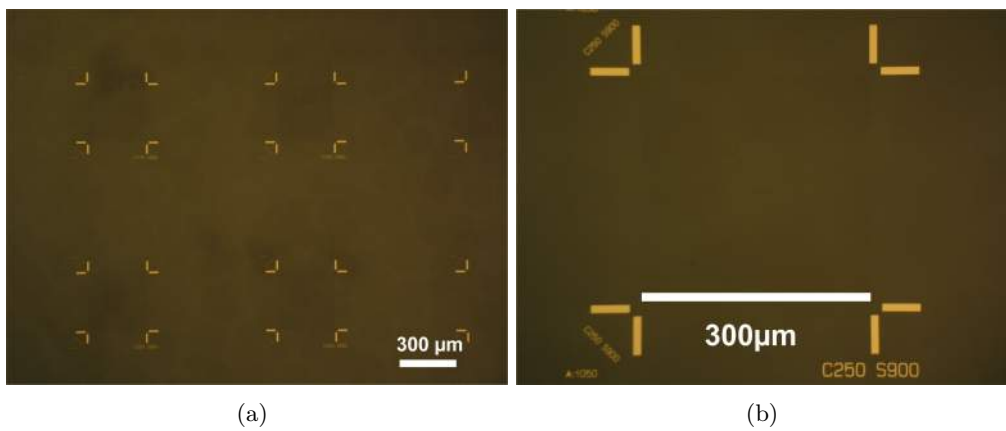


**Figure 3.6.:** Light optical microscope images for (a) the sample with four antenna area arrangements and (b) a specific area of  $300\ \mu\text{m} \times 300\ \mu\text{m}$  zoomed in. The sample marked as C250S900 is for disk shaped antennas with diameter 250 nm and a quadratic periodicity of 900 nm.

parameters. In other words, the particle volume, particle periodicity and the aspect ratio have to be considered, one at a time, to understand the influence of each factor on the spectral features. Keeping this in mind three different sample sets are prepared.

**Table 3.1.:** Overview of fabricated Au nanoantennas samples

| Samples             | Period (nm) |          |          | Length (nm) |          | Figure |
|---------------------|-------------|----------|----------|-------------|----------|--------|
| Change in           | S.No.       | Period x | Period y | Length x    | Length y |        |
| Set 1: Size         | 1           | 900      | 900      | ∅ 250       | ∅ 250    | 3.7(b) |
|                     | 2           | 900      | 900      | ∅ 225       | ∅ 225    | -      |
|                     | 3           | 900      | 900      | ∅ 200       | ∅ 200    | -      |
|                     | 4           | 900      | 900      | ∅ 175       | ∅ 175    | 3.7(a) |
|                     | 5           | 900      | 900      | ∅ 150       | ∅ 150    | -      |
| Set 2: Periodicity  | 1           | 900      | 800      | ∅ 250       | ∅ 250    | 3.8(a) |
|                     | 2           | 900      | 900      | ∅ 250       | ∅ 250    | 3.8(b) |
|                     | 3           | 900      | 1000     | ∅ 250       | ∅ 250    | 3.8(c) |
| Set 3: Aspect Ratio | 1           | 900      | 900      | 225         | 218      | -      |
|                     | 2           | 900      | 900      | 245         | 200      | 3.9(a) |
|                     | 3           | 900      | 900      | 265         | 185      | -      |
|                     | 4           | 900      | 900      | 285         | 172      | 3.9(b) |
|                     | 5           | 900      | 900      | 305         | 160      | -      |
|                     | 6           | 900      | 900      | 325         | 150      | -      |
|                     | 7           | 900      | 900      | 345         | 140      | 3.9(c) |

### 3.2.1. Overview of fabricated samples

Three different sets of samples are prepared by e-beam lithography, with specifications shown in table 3.1. Each set is produced with an aim to alter one spectral feature, i.e. either shift the single particle resonance or shift and vary the strength of the new grating resonances.

### 3.2.2. Change in size

Round disk shaped antennas with diameters of 250 nm, 225 nm, 200 nm, 175 nm and 150 nm, all with height of 50 nm are fabricated. These disks are arranged in a 300 μm x 300 μm area with quadratic periodicity (i.e. center to center distance in both x- and y-direction) of 900 nm. The SEM images of two representative samples with disk diameter of 175 nm and 250 nm are shown in figure 3.7.

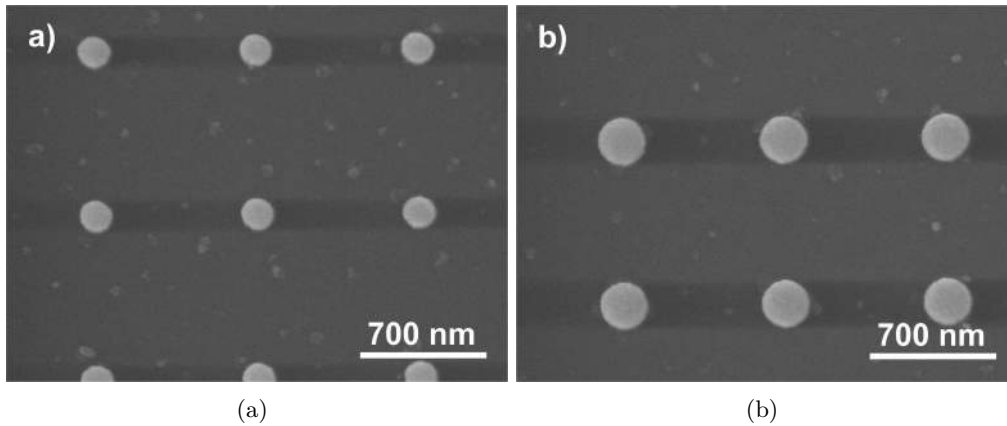


**Figure 3.7.:** SEM images of disk shaped nanoantennas with diameters of (a) 175 nm and (b) 250 nm arranged quadratically with a period of 900 nm. The dark stripes are charging effects in SEM.

#### 3.2.3. Change in period

The second set of samples comprises of samples in which the periodic arrangement of nanodisk arrays is varied. All the samples, in this set have a constant disk diameter and the arrangement periodicity in x-direction is 900 nm. Whereas, the periodicity in y-direction is changed to 800 nm, 900 nm and 1000 nm. The SEM images of the three samples are shown in figure 3.8.

#### 3.2.4. Change in elongation

Polarization effects can be observed much more clearly when the disks are elongated in one direction and compressed in the other [88, 89, 92]. So the set 3 of samples, is comprised of varying aspect ratios of the nanoantennas, while keeping the volume constant. The samples are written with dimensions (length x width): 225 nm x 218 nm, 245 nm x 200 nm, 265 nm x 185 nm, 285 nm x 172 nm, 305 nm x 160 nm, 325 nm x 150 nm and 345 nm x 140 nm. The thickness of Au is 50 nm in these samples. The longer axis of all these samples is defined along y-direction. The SEM images of three representative samples with dimensions 245 nm x 200 nm, 285 nm x 172 nm and 345 nm x 140 nm are shown in figure 3.9.

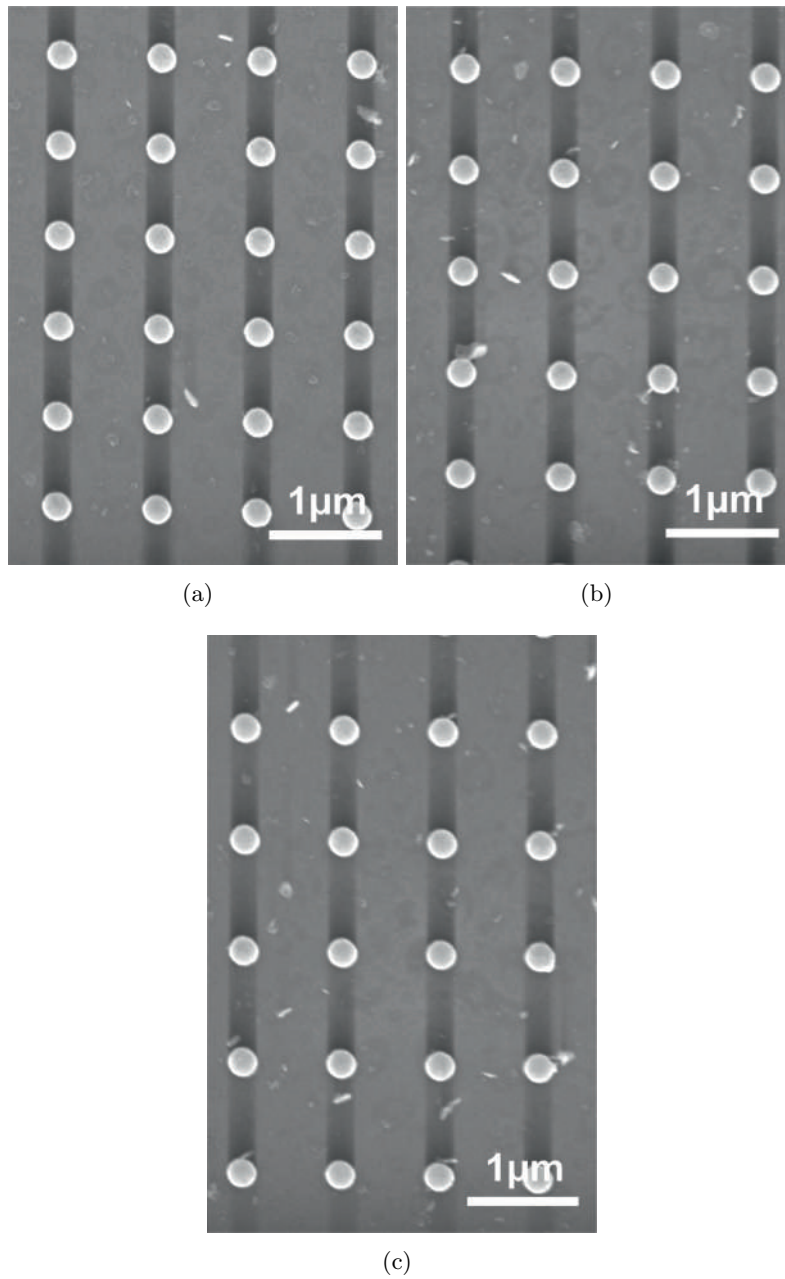


**Figure 3.8.:** SEM images of Au antennas with same disk diameter of 250 nm. They are arranged with a period of 900 nm in x-direction and a period of (a) 800 nm , (b) 900 nm and (c) 1000 nm in y- direction. The dark stripes are charging effects in SEM.

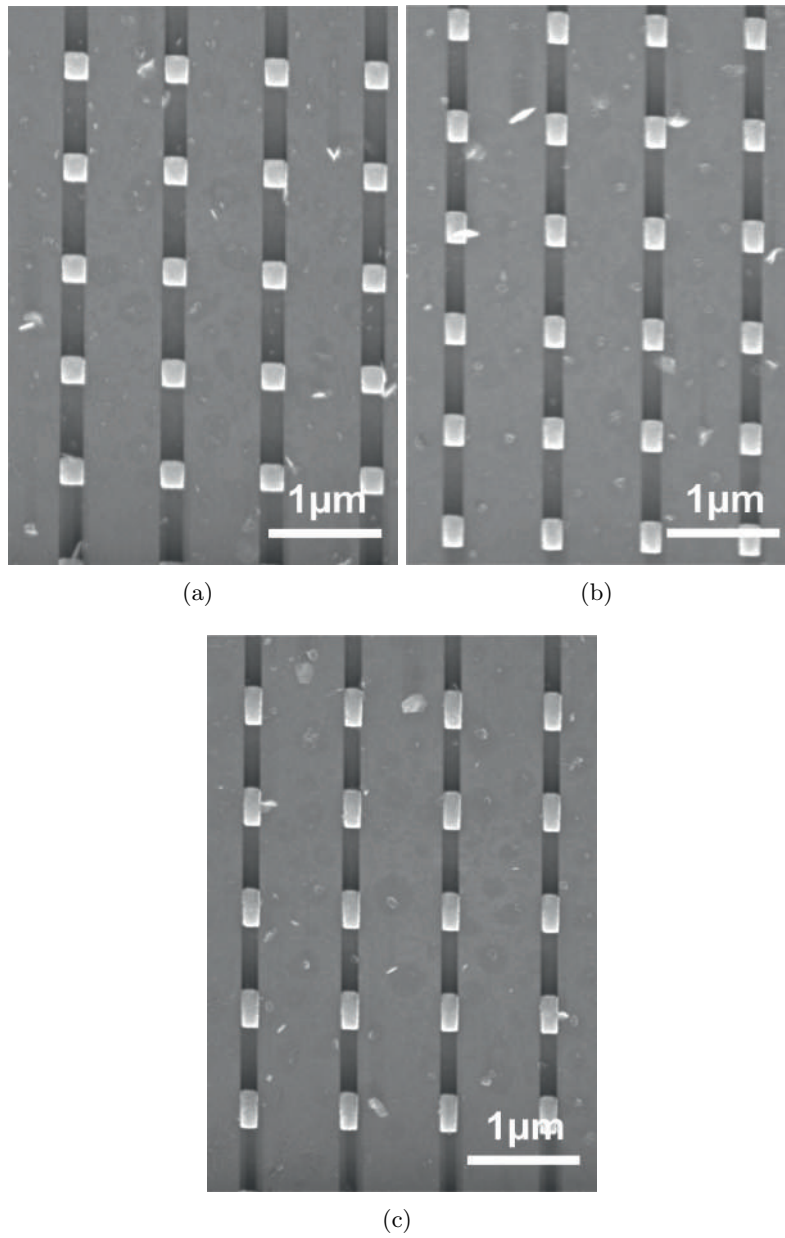


**Figure 3.9.:** SEM images of rectangular Au nanoantennas with dimensions (a) 245 nm x 200 nm, (b) 285 nm x 172 nm and (c) 345 nm x 140 nm. The dark stripes are charging effects in SEM.

### 3.3. Optical characterization by transmission measurements

The characteristic optical extinction of the nanoantennas was investigated by transmission measurements. It is known from the literature [86, 93, 94] that a homogeneous refractive index environment is important to achieve narrow structural resonances in nanoparticle arrays (i.e. they should be embedded in a homogeneous medium). So as to avoid the smearing out of optical spectral details, a homogeneous embedding and surrounding of the antennas with a refractive index of 1.5, similar to that of glass substrate is essential. This section begins with the methods that were used to embed the nanoantennas followed by the setups used for their characterization. Further, in this section, all the transmission results from the different antenna arrangements are discussed with respect to theoretical calculations and in context with contemporary literature.

#### 3.3.1. Embedding the nanoantenna arrays in 1.5 refractive index

After the nanoantennas were fabricated by electron beam lithography and a lift off process in an area of  $300\ \mu\text{m} \times 300\ \mu\text{m}$  on glass they had to be covered with a material with refractive index  $n=1.5$  to get a homogeneous environment of  $n = 1.5$  all around the antennas. The embedding procedure was carried out in two different ways:

- a) A thin ( $1\ \text{cm} \times 1\ \text{cm} \times 0.1\ \text{cm}$ ) glass slide is fixed from one side using super glue to the area of interest, and left to dry. Index matching oil with refractive index of 1.5 is dropped around the entrance. The glass forms a capillary action which pulls in the oil, hence, creating a uniform  $n = 1.5$  medium around the antennas. The thickness of the oil layer is approx.  $1\ \text{mm}$ .
- b) A drop of  $5\ \text{wt}\%$  PMMA in chloroform is dropped on top of the nanoantennas and spincoated at  $500\ \text{rpm}$  for  $1\ \text{min}$  and left to dry overnight. The thickness of the resulting PMMA layer is  $3.4\ \mu\text{m} \pm 0.2\ \mu\text{m}$ . The antenna samples are now surrounded by a constant refractive index of 1.5 and taken for transmission measurements.

Both the above methods of embedding the antennas by refractive index of 1.5 give similar results in transmission measurements that follow.

#### 3.3.2. Transmission measurement setup for nanoantennas

Transmission measurement setup comprises of a halogen lamp as a white light source. The light from the lamp is collimated using a two lens system. A collimated beam is

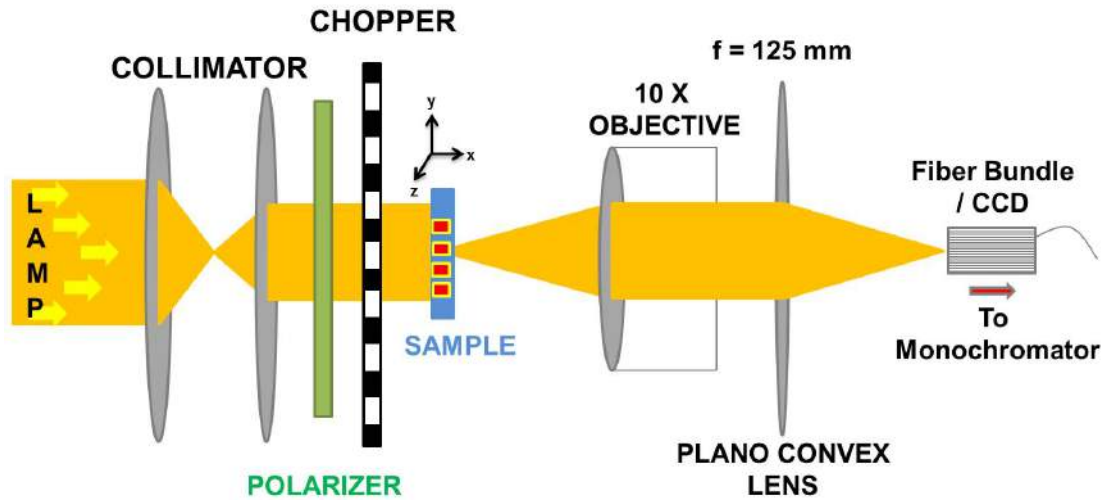


*Figure 3.10.: Schematic of the setup used for transmission measurements of nanoantenna samples*

used in order to excite all the antennas with the same phase. This collimated beam of light enters the sample from the substrate side and exit's through the PMMA or oil-glass interface. The transmitted light enters a Mitutoyo 10x (infinity corrected long working distance) objective and together with a plano-convex lens creates an intermediate image at the CCD camera. To detect the transmitted intensity the CCD camera is replaced by a fiber bundle which is placed in the intermediate image plane. The whole  $300 \mu\text{m} \times 300 \mu\text{m}$  area of antennas is imaged on the fiber bundle with this setup. The transmitted light from this single region of antennas is guided to a grating spectrometer which is equipped with single channel photodiode detectors for both near IR and visible wavelengths. Using a rotatable polarizer allows to control the polarization of the incident light at specific samples.

### 3.3.3. Array of nanoantenna disks with 250 nm diameter

The nanoantenna disks with 250 nm diameter and 50 nm height which are arranged in a quadratic lattice with a period of 900 nm are taken for transmission measurements in the setup defined above. The experimental transmission intensity is plotted in figure 3.11(a) as a black curve. A broad dip in transmission is observed with a minimum at 1040 nm. This broad extinction resonance corresponds to the excitation of the localized surface plasmon resonance (LSPR) in single Au disks. It has a width of approx. 570 nm which can be seen by fitting a Lorentzian curve to the transmission data. This Lorentzian

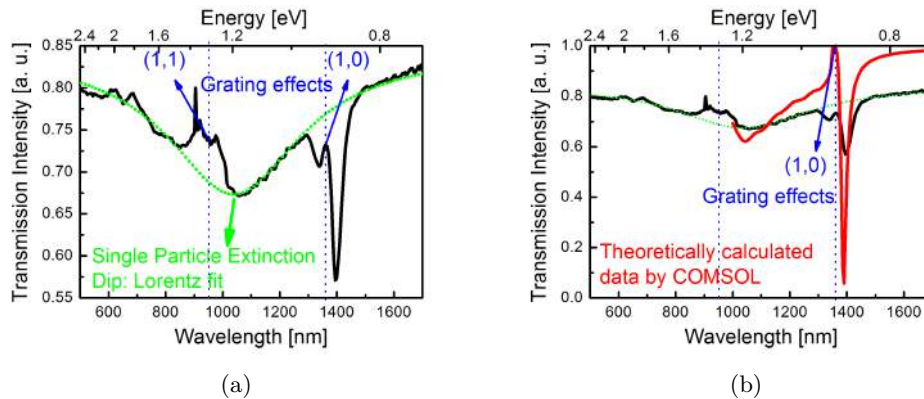


**Figure 3.11.:** Transmission data of nanoantenna arrays of 250 nm diameter, arranged quadratically with periodicity of 900 nm. (a) The black solid line shows the transmission measurement. A Lorentzian curve is fit to the spectrum and is shown in green to depict the extinction spectrum of a single Au-particle without any other effects. The grating effects are introduced at 1350 nm and 955 nm due to first order (1,0) and 2nd order (1,1) grating diffraction. (b) A finite element calculation (COMSOL) of the extinction of the same configuration in a restricted spectral range is shown as red line while black solid line is still the experimental transmission measurement.

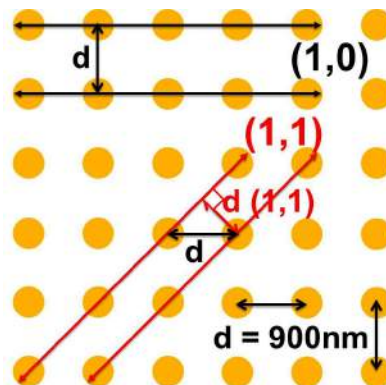


**Figure 3.12.:** The (1,0) and (1,1) diffraction edges and the corresponding distances between the interacting antenna directions.

fitting approximately coincides with the position of the dipolar resonance from a 250 nm Au spherical particle/nanoantenna, which would appear at 1050 nm. As all the higher orders of quadrupole extinction take place far towards the blue regime, so indeed the observed dip in transmission (peak in extinction) can be identified as the dipole resonance contribution from single disk shaped nanoantennas.

Furthermore, the dashed vertical lines (figure 3.11(a)) at  $955\text{ nm}$  and  $1350\text{ nm}$  indicate the position at which Raleigh (or Woods) anomalies can occur. Raleigh anomalies are dips in 0. order transmission when a new diffraction order starts to propagate. It is caused by a redistribution of energies among all the diffraction orders. For the simplest case, when the wavelength of the light (at normal incidence) is longer than the period of a grating only the 0. reflection and the 0. transmission orders exist. All other diffraction orders are evanescent and can not transport energy away from the grating, so that all incident radiation is transported away in the 0. transmission and reflection orders or is absorbed within the grating. When the wavelength at normal incidence becomes shorter than the grating period, then the 1. and -1. diffraction orders in reflection and transmission can propagate and carry energy. This leaves less energy for the 0. order, so that at this wavelength a dip in 0. order transmission (which is measured in the experiments) will appear.

Since in our case, a two dimensional lattice exists, one has to consider different directions within the 2D-plane to identify lattice planes (or better “lattice lines” in 2D) which act as “grating”. The lattice planes with the largest period of  $d = 900\text{ nm}$  are the (1,0) planes, whose Rayleigh anomaly(RA) should occur at  $1.5 * 900 = 1350\text{ nm}$  (1.5 is the refractive index of the grating environment) [64, 95–97]. The next Rayleigh anomaly will occur for the (1,1) lattice planes and can be predicted at  $1.5 * 900 * \sin(45^\circ) = 955\text{ nm}$ . The directions of the lattice planes with corresponding distances are shown in figure 3.12.

Revisiting the transmission curve in figure 3.11 again indeed one observes clear features in the vicinity of these wavelengths. For wavelength slightly longer than the  $1350\text{ nm}$  RA a sharp dip in transmission is formed while for slightly longer wavelengths another small dip appears. They are on top of the broad underlying single resonance extinction. These sharp dips are obviously connected with the lattice period and represent surface lattice resonances (SLR). At this SLR the electron gas in all Au-disks oscillates with the same phase since the scattered field from neighboring disks arrives with the same phase as the exciting wave at normal incidence (distance between disks is just about  $\lambda$ ). In this way, the dipoles support their oscillation mutually leading to a strong resonance. Since the first SLR occurs for wavelength just slightly longer than the first Rayleigh anomaly, only the 0. diffraction order are able to carry energy away which leads to strongly reduced scattering losses resulting in a narrow line shape.

A finite element calculation (done by Dr. C. Bohley using COMSOL) of the transmission through the Au-disk lattice (red curve in figure 3.11) confirms the spectral position of the SLR. However, the calculated resonance dip appears sharper and deeper than the

measured one. This is probably due to experimental limitations as the width of the SLR depends on the amount of nanoantennas oscillating with the same phase, while in theoretical calculations periodic boundary conditions were applied assuming basically an infinite amount of resonators. Experimentally, however, the antenna area was only  $300\ \mu\text{m} \times 300\ \mu\text{m}$  large. Arranging all disks in lattice lines with a period of  $900\ \text{nm}$  gives therefore only a finite number of 333 Grating lines. Furthermore, a slight divergence of the beam will lead to a non-planar wave front, so that slight phase differences in the excitation of the Au-disks might occur which also limit the number of constructively interfering dipoles. These experimental conditions will therefore lead to a “weaker” appearance of the SLR.

Having a closer look on the line-shape of the SLR a slight asymmetry is observed. The resonance dip has a sharp rise at short wavelength but a longer tail at longer wavelengths. This Fano-line shape arises from the coupling of the broad LSPRs resonance with the lattice resonance, due to which the surface lattice resonances do not exactly coincide with the Rayleigh anomaly but are little bit red shifted [15].

In the vicinity of the (1,1) Rayleigh anomaly such a strong SLR is not observed but a clear rise in transmission occurs which reduce the single particle resonance within the range  $880\ \text{nm} - 1000\ \text{nm}$ . Probably the larger scattering losses, which can occur at these shorter wavelengths in the (1,0), (-1,0), (0,1) and (0,-1) diffraction orders, inhibit the formation of a strong SLR like for the (1,0) lattice resonance. From now onwards, the thesis focuses mainly on the pronounced (1,0) resonance and the IR regime.

From the mechanism of the radiation coupling between neighboring nanoantennas the sensitivity of the SLR with respect to different refractive indices becomes clear. If the nanoantennas would not be embedded in an homogeneous medium, but arranged on glass substrate and kept in air, the refractive index step between glass and air in the surrounding of a nanoparticle array makes the wavelength of light at the two sides (above and below the air/glass surface), considerably different. This prevents the scattered light of the dipoles from summing up coherently at their neighbors. Zhukovsky et al. [93, 94] investigated this index-matching problem theoretically and found, that the larger the index mismatch is, the sooner the lattice resonance disappears for increasing distance between the nanoantennas. This is understandable since with rising distance between the nanoantennas the overall phase difference for scattered light traveling in index area 1 or 2 also increases. If the embedding of the sample would be in a lower refractive index medium than 1.5, then referring to the theoretical calculation in [94], it can be predicted for our samples too, that the LSPR will move towards higher frequencies.

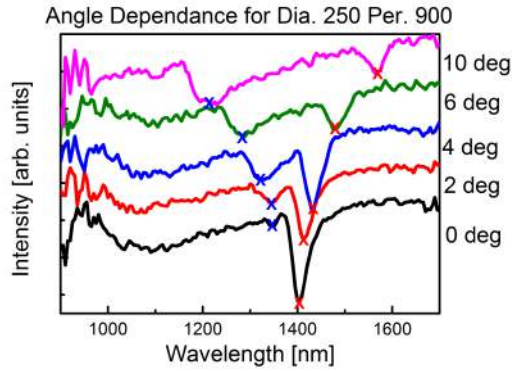


**Figure 3.13.:** Experimental transmission measurements of 250 nm disk arrays for changing angle of incidence of light on the sample from  $0^\circ$  to  $10^\circ$ .

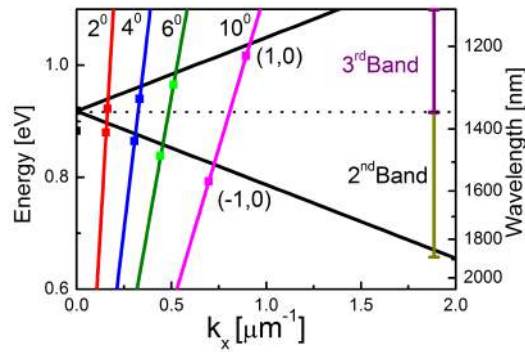


**Figure 3.14.:** The dispersion plot of experimental values (squares) received from figure 3.13. This is superimposed on calculations from a simple Maxwell-Garnett layer model (solid black lines).

Another set of transmission experiments was carried out by changing the angle at which light is incident on sample. The incident light angle is changed from normal incidence ( $0^\circ$ ) to higher angles of incidence ( $2^\circ$ ,  $4^\circ$ ,  $6^\circ$ ,  $10^\circ$ ). The results are shown in figure 3.13. A broad resonance centered at  $1050\text{ nm}$  for all angles is observed, which is followed by two dips which separate clearly with increasing angle. On increasing the angle of incidence, the dips on the left side, shift towards blue (shown as blue crosses in figure 3.13) while there is a red shift of dips on the right hand side (shown by red crosses in figure 3.13).

The array of nanoantennas can be interpreted as a two dimensional (2D) flat metallo-dielectric photonic crystal, where metallic scatterers are periodically arranged. Hence the work done by the group of Rivas [15, 96, 98], can be a guide line for explaining the observed splitting and shift. Similar like in a pure dielectric photonic crystal photonic

bands appear. Within this figure the observed resonances and their splitting correspond to the excitation of photonic modes. The larger dip moving to long wavelengths (smaller  $\omega$ ) represents the excitation of modes within the 2<sup>nd</sup> band while the dip moving to shorter wavelengths with increasing angle stems from the excitation of the modes in the 3<sup>rd</sup> band. These bands form by shifting the dispersion relation by the reciprocal lattice vectors (-1,0) and (1,0) into the first Brillouin zone.

To support the above interpretation with theoretical calculations, a simple model is suggested. For the moment, the long wavelength limit is assumed and the disk array is modeled as an effective medium using the 2D anisotropic Maxwell-Garnett theory from Part I of this thesis and considering an Au-filling factor of 6% for the Au disks. The layer comprises Au antennas (rods) embedded in refractive index of 1.5 matrix system. This layer has two principal dielectric constants ( $\epsilon_{\parallel eff}$  and  $\epsilon_{\perp eff}$ ), details of which have been discussed in section 2.1.2.2. Furthermore, it is known that the Maxwell-Garnett model fits well to ordered structures with low filling factor values. The value of  $\epsilon_{\perp eff}$  to the surface is calculated, which is then used to plot the dispersion relation of this embedded layer. The theoretical values are plotted as black line in figure 3.14. The experimental values are taken from figure 3.13 and plotted in figure 3.14. A reasonably good fitting with experiments is achieved with this simple model. In figure 3.14, at normal incidence, the experimental data points should ideally superimpose as in case of theory, but there is a splitting in the energy values by  $0.04 eV$ . This splitting at normal incidence is the classical counterpart of Rabi energy splitting [66, 99–101]. Also, a blue shift for surface lattice resonance fano-line shape  $g (+1,0)$  and a red shift for  $g (-1,0)$  is confirmed in literature by Murai et al. [15].

The transmission experiment on  $250 nm$  disk diameter and corresponding theoretical calculation concludes the following points:

1. A Lorentzian peak is a good approximation for fitting the single particle resonance.
2. Two Rayleigh anomalies (1,0) and (1,1) interfere with the Lorentzian peak.
3. A sharp dip corresponding to SLR appears slightly at the longer wavelength side of the Raleigh anomaly (1,0).

### 3.3.4. Effect of change in size of Au disk nanoantennas

Antennas in sample set 1 of table 3.1, comprising of varying Au disk diameters are measured under transmission. The stacked transmission data is shown in figure 3.15(a). In figure 3.15(b), the single particle resonance is shown as a overlaid Lorentzian (peak

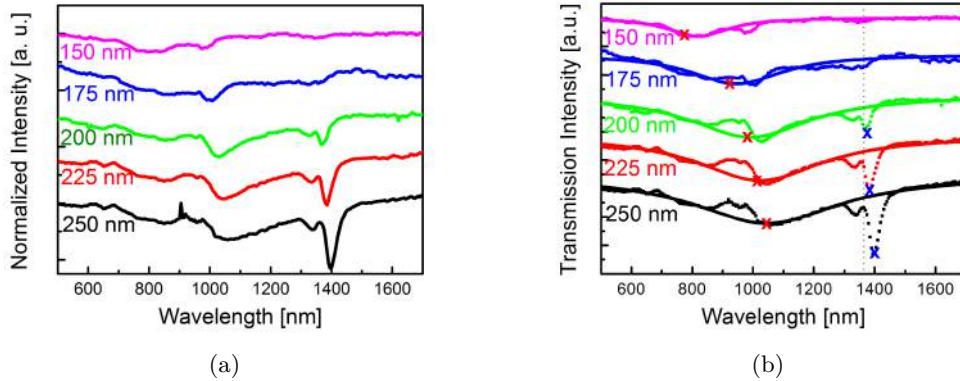


**Figure 3.15.:** (a) Transmission measurements of nanoantenna arrays with increasing disk diameter from 150 nm to 250 nm. (b) Lorentzian curve fitting shows red shift in the corresponding single particle resonance (red crosses) and enhancement of surface lattice resonance peak (blue crosses).

positions shown as red crosses). A broad resonance centered at approximately 1050 nm, 1000 nm, 950 nm, 900 nm and 800 nm are observed for 250 nm, 225 nm, 200 nm, 175 nm and 150 nm disk diameters, respectively. Relatively sharp spectral peaks (marked as blue crosses) is observed to the right hand side of the broad resonance. In figure 3.15(b), these occur at approx. 1400 nm for 250 nm diameter disks and shift slightly towards the blue as the diameter reduces. It is also observed that, these sharp features eventually decay excessively, by the time, the disk diameter reaches 175 nm and are almost absent for 150 nm. Finally, some discrepancies in the smooth Lorentzian to the left hand side of the the broad resonance peak are also observed <sup>3</sup>.

As the disk diameter increases a red shift in single particle resonance is observed, which is also supported by the Mie calculation of extinction for Au spherical particles in section 3.1.1. As the effective area of disks (used in experiments) interacting with the incoming light is the similar for the sphere (used for Mie calculation), so the results are comparative. The Mie theory in figure 3.1(a) and 3.1(b), shows an extinction at 700 nm and 1050 nm for spheres of diameters 150 nm and 250 nm, respectively. At the same time, the experimental data from figure 3.15(b) shows the single particle resonance at 800 nm and 1050 nm for disks of diameters 150 nm and 250 nm, respectively. Moreover,

<sup>3</sup>The observed spectral details can be clearly seen for data received from one single kind of array disks (as discussed for  $\phi$  250 nm in figure 3.11(a)). But as the transmission measurements of different disk diameter arrays are stacked one on the other to give a better comparison of the samples. This stacking results in the loss of the exact intensity values and quantitative sharpness of some spectral features with respect to others.

the filling fraction of Au nanoantennas ( $f_{\phi 150nm} = 0.087$  and  $f_{\phi 250nm} = 0.242$ ) is a good representative for the scattering volume. As the disk diameter reduces, i.e. the packing density reduces hence resulting in reduced impact from scattering (The figures 3.1(a-c), calculated using Mie theory show this effect clearly). Furthermore, as the particles are not so densely packed, therefore, the impact is not so big on the scattering effects.

Also, as the filling fraction decreases for disks with diameters from  $250\text{ nm}$  to  $150\text{ nm}$ , the scattering volume decreases. This leads to a growing spectral separation between single particle resonance and the RA (1,0) array resonance SLR. The smaller single particle oscillation amplitude reduces also the scattering, which in turn results in the decay of SLR related spectral features. Also, this surface lattice resonance is bound by the  $1350\text{ nm}$  Raleigh anomaly. Now, as the disk diameter is decreased, the spectral position of the sharp SLR is slightly blue shifted, but, as its bound to the RA, the spectral feature becomes less and less pronounced as the diameter of the disks decreases.

Now, considering the RA (1,1) which is at approx.  $955\text{ nm}$  due to the grating effect. As the disk diameter decreases, the broad Lorentzian peak, shifts towards blue from  $1050\text{ nm}$  to  $800\text{ nm}$  and passes through the above said fixed RA (1,1). This gives an interference result of the two spectral features (Lorentzian and RA), hence resulting in the attenuated peak intensity around this region for lower diameters.

Set 1 of transmission experiments on varying disk diameters while keeping the periodicity constant, concludes with the following points:

1. As the disk diameter reduces the single particle resonance shifts towards blue.
2. There is a slight blue shift and decline of the intensity in the SLR dips with decreasing particle diameter.
3. Rayleigh anomalies remain fixed for constant periods and interfere with the scattering volume effects from the single particle resonances.
4. Mie theory can predict the single particle resonances for larger disks quite well.

#### 3.3.5. Effect of change in periodicity of Au disk nanoantenna arrays

Antennas with disk diameter of  $250\text{ nm}$  are arranged with different periodicity as stated in sample set 2 of table 3.1. There are three samples and each one has a periodicity (center to center distance) of  $900\text{ nm}$  in x-direction, while, in the y-direction, the periodicity is  $800\text{ nm}$ ,  $900\text{ nm}$  and  $1000\text{ nm}$ , respectively. By using two different orthogonal polarization directions of light the direction of light scattering and the process of coupling between neighboring antennas can be probed. It is observed that both these polarizations do

### 3. Localized Surface Plasmons on Metal Nanoantenna Arrays

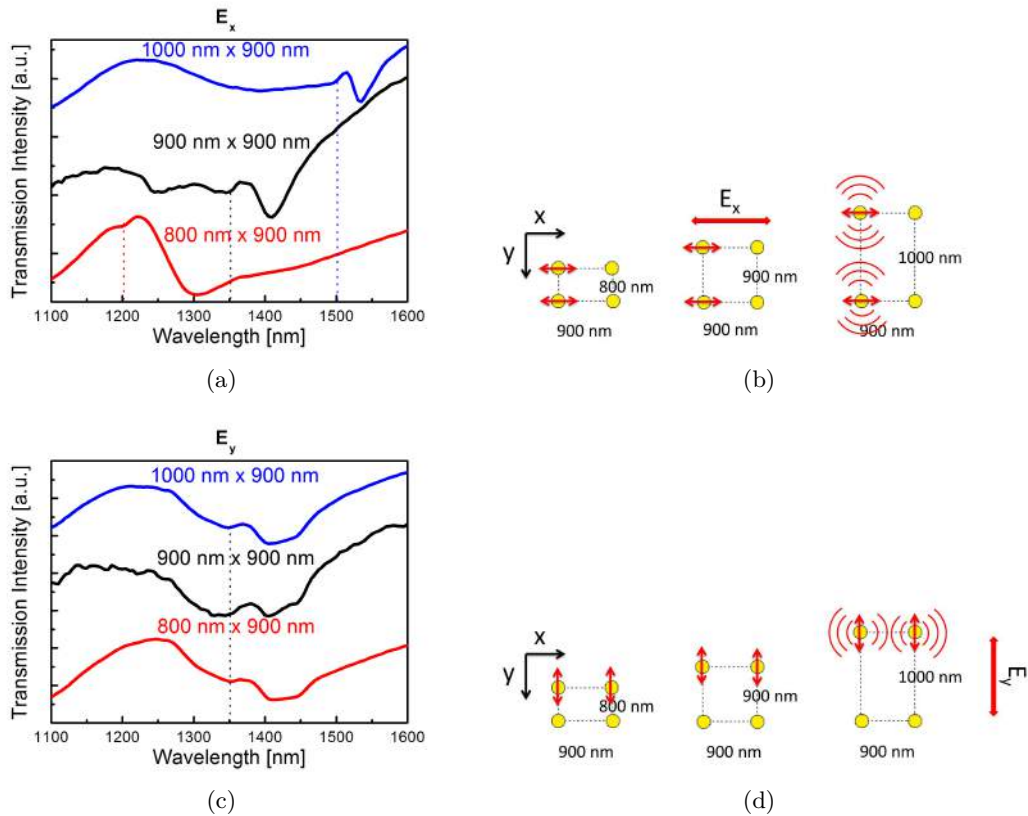


**Figure 3.16.:** Transmission measurements of Set 2: antennas with constant periodicity of 900 nm in  $x$ -direction and varying periodicity of 800 nm, 900 nm and 1000 nm in  $y$ -direction. (a) Transmission measurement for light polarized along  $x$ -direction and its corresponding (b) schematic for dipole-dipole resonance parallel to  $E_x$  and the net coupling effect is seen in  $y$ -direction. (c) Transmission measurement for light polarized along  $y$ -direction and its corresponding (d) schematic for dipole-dipole resonance parallel to  $E_y$  and the net coupling effect is seen in  $x$ -direction.

not effect the position of the broad single particle resonance and it is always at approx.  $1050 \text{ nm} \pm 20 \text{ nm}$  for all the three samples. This is reasonable, since the disks are circular and do not show any distinguished direction by themselves for normal incidence.

Let's first look at the transmission results in figure 3.16(a). When the polarizer directs the incoming light electric field in horizontal direction then a red shift in SLR is observed for increased center to center distances between the disks along the  $y$ -direction. Also, a decay in intensity of this spectral feature is observed. However, when the electric field is polarized in vertical direction, the transmission measurement in figure 3.16(c) shows no change in the spectra for all three samples.

The cause for this polarization dependence of the SLR-position becomes obvious when the scattering field of the nanoantennas is studied for both polarizations (Fig. 3.16(d), Fig.3.16(b)). When the electric field oscillates in horizontal direction, each dipole radiates mainly sideways (largest amplitude in y-direction). This scattered wave excites the nearest neighbor nanoantenna in y-direction, which radiates its own scattering field leading to an efficient radiative coupling of all antennas along the y-direction. Hence, an overall effect of grating contribution from periodicity in y-direction is observed. As the Rayleigh anomaly and SLR specifically depend on the periodicity of the arrangement of antennas in coupling direction, the first order of diffraction (1,0) and SLR is seen at  $1.5 * 800 = 1200 \text{ nm}$ ,  $1.5 * 900 = 1350 \text{ nm}$  and  $1.5 * 1000 = 1500 \text{ nm}$  wavelength, respectively for the three samples. This collective scattering resonance coincides actually with Bragg-scattering at the (0,1) lattice planes. Furthermore, as the periodicity increases, the distance between the RA from the single particle resonance location dip also increases. This increased distance leads to lower LSPR and weaker radiative coupling, hence, leading to lowering of the SLR intensity far away on the decaying part of single particle resonance.

Similarly, when the electric field of incident light is polarized in vertical direction, the antenna dipoles resonate parallel to it (figure 3.16(d)), hence, the scattered fields radiate in x-direction and probing the lattice periodicity along this directions (Bragg-scattering at (1,0) in x-direction). As each of the three samples have the same periodicity of  $900 \text{ nm}$  in x-direction, the transmission measurement in figure 3.16(c) shows the same spectral position of the Rayleigh anomaly of the diffraction order (1,0) at  $1350 \text{ nm}$ .

Similar red shifts, in the extinction spectra have been shown by Auguie et al.[67] for Au nanoparticle arrays but only in the visible range from  $700 \text{ nm}$  to  $800 \text{ nm}$  for particles of  $123 \text{ nm} \times 85 \text{ nm}$  and  $109 \text{ nm} \times 94 \text{ nm}$ , both having height of  $35 \text{ nm}$  and small pitch variation from  $460 \text{ nm}$  to  $540 \text{ nm}$ .

Set 2 of transmission experiments on varying periodic arrangements of constant disk diameters, concludes with the following points:

1. SLR is highly dependent on the relation between polarization and grating period.
2. The polarization dependence of the SLR demonstrated that the coupling between the nanoantennas occurs perpendicular to the oscillation of the dipoles (polarization direction). These results unambiguously confirm that the coupling between the nanoantennas is performed over their radiation fields (scattered field). An impact of near field coupling (which would be largest along the direction of oscillation of the dipoles) was not observed.

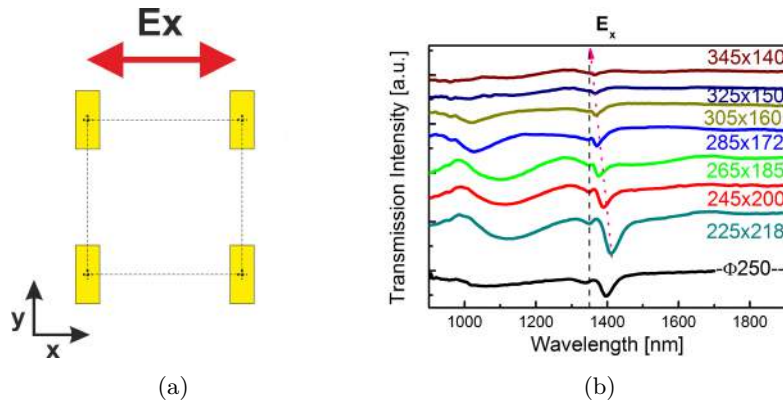


**Figure 3.17.:** Optical measurements of Set 3: (a) Schematic for changing aspect ratio of antennas, keeping volume constant. The light polarization direction is along the shorter side i.e. x-direction. (b) Transmission measurement data showing a slight blue shift of SLR with increasing aspect ratio.

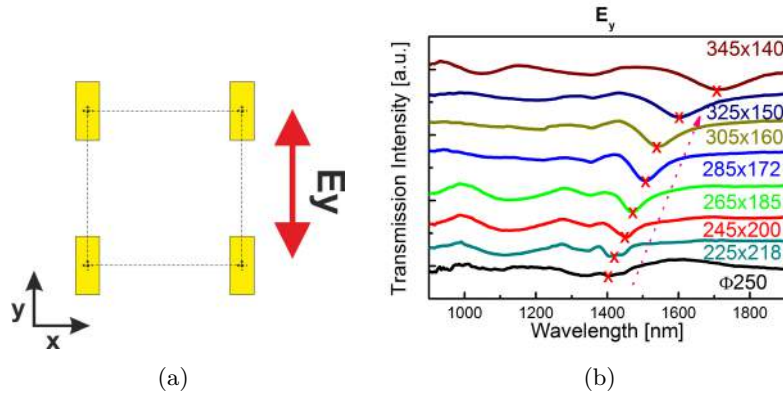


**Figure 3.18.:** Optical measurements of Set 3: (a) Schematic for the light polarization direction is along the longer side i.e. y-direction. (b) Transmission measurement data showing red shift of SLR with increasing aspect ratio.

### 3.3.6. Effect of change in aspect ratio of Au nanoantennas

The final set, namely set 3 of table 3.1, which contains the antennas with varying aspect ratio but the same volume as 250 nm disk antennas and 900 nm quadratic lattice are compared under transmission. Seven different rectangular dimensions are considered: (length x width) 225 nm x 218 nm, 245 nm x 200 nm, 265 nm x 185 nm, 285 nm x 172 nm, 305 nm x 160 nm, 325 nm x 150 nm and 345 nm x 140 nm. The longer side of these rectangular antennas is always arranged along y-direction as defined in figures 3.17(a) and 3.18(a).

It is observed that when the electric field of the incident light is along x-direction i.e. along the shorter axis of the rectangle, on increasing the aspect ratio, a blue-shifted resonance with decaying intensity is visible in figure 3.17(b). While, when the electric field is along y-direction (figure 3.18), i.e. along longer axis, the higher aspect ratio rectangular antennas exhibit a red shifted spectral feature with increased depth.

Each elongated antenna exhibits a longitudinal resonance (LR) and a transverse resonance (TR) [102, 103]. In case of LR, there is a red shift for stronger aspect ratios. This also leads to a red shift of the SLR Fano resonance. On the other hand, the TR leads to a very small blue shift of the SLR for thinner rods [88, 89]. The possibility to excite either LR or TR depends upon the direction of polarization of incident light. Similarly, in the above defined set of experiments, when the antennas are excited along x-direction, the TR is excited and hence a blue shift is seen. Similarly, for polarization along y-direction the LR leads to a red shift.

In addition to LR and TR, each nanoantenna acts like a dipole contributing to the radiative coupling (discussed in section 3.1.2). The volume of all rectangular nanoantennas is the same, i.e. they have the same scattering volume but as each nanoantenna is elongated more in one direction, this leads to increased dipole moment i.e. stronger scattering and creates deeper dips. This also shows the polarization dependence of the far field coupling. This coupling is strong when the antennas are placed side by side while no coupling is seen when the antennas are excited head to tail.

In contemporary literature, such extinction measurements have been predicted and shown experimentally but only till  $1000\text{ nm}$  wavelength. Vecchi et al. [96] showed the experimental transmittance for rectangular arrays supported by FDTD calculation through 2D plasmonic crystal in the range from  $500\text{ nm}$  to  $1000\text{ nm}$  for a fixed periodicity or pitch by varying angle of incidence.

### 3.4. Optical characterization by photoluminescence measurements

Metal nanoantennas show high degree of optical field confinement and high sensitivity to their local environment just by supporting localized optical modes of surface plasmons. If any particle having the same resonance frequency, (as that of the said optical modes) and is placed in vicinity of such antennas, then there is a possibility of luminescence enhancement. This possibility is explored in this section of the thesis.

#### 3.4.1. Embedding in PMMA containing PbS quantum dots

PbS quantum dots (due to its size dispersion) show strong photoluminescence in the range from 1300 *nm* to 1600 *nm*. The PL spectrum for PbS embedded in PMMA on glass is shown in figure 3.19. The large spectral range of the luminescence is caused by the size dispersion of the PbS particles. In this thesis, a possibility to exploit the constructive interference of the dipole scattering fields and the luminescence enhancement of PbS quantum dots has been explored. The PL peak lies towards the red side of the single particle Au extinction and in the range of the SLR.

Various samples with different concentrations of PbS in PMMA are prepared and PL is measured. The higher PL intensity is observed for the sample prepared by mixing 20  $\mu\text{mls}$  of PbS (received from evident technologies) is added to 1  $\text{mlts}$  of 5 *wt%* PMMA in chloroform, giving,  $2 * 10^{22}$  PbS nanoparticles per  $\text{m}^3$  of PMMA. This solution is spin coated onto the sample of interest at 500 *rpm* for 1 *min* to achieve  $3.2 \pm 0.2 \mu\text{m}$  layer thickness. The samples are left to dry overnight in Ar atmosphere <sup>4</sup>.

#### 3.4.2. $\mu$ -Photoluminescence setup

A He-Ne laser (633 *nm*) is used as the exciting laser for the PMMA-PbS embedded Au nanoantenna samples since its wavelength is absorbed well by the PbS but not by the PMMA. The laser passes through a chopper and a series of aperture and beam splitter. Finally, light is focused onto the sample by the Mitutoyo 10x (infinity corrected long working distance) objective. To easily locate the area of interest of nanoantennas, the

---

<sup>4</sup>Ar atmosphere is important to avoid the degradation of PbS quantum dots in air.

### 3.4. Optical characterization by photoluminescence measurements

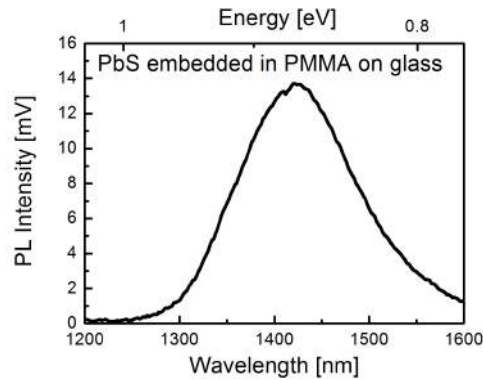


*Figure 3.19.: Photoluminescence of PbS quantum dots embedded in PMMA and spin coated on glass substrate.*

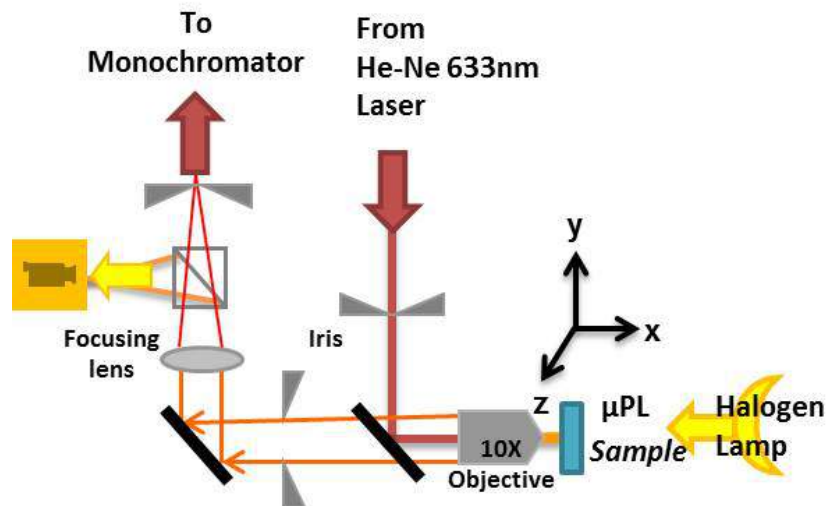


*Figure 3.20.: Schematic of the  $\mu$ -PL setup.*

sample is mounted onto a xyz-translation stage. The area can be viewed on a CCD camera when a halogen lamp is shown from backside of the sample.

A laser spot size of  $50 \mu m$  is focused onto this area of interest. When only laser is incident onto the sample, the light emitted from the sample after the absorption of photons is reflected back, this light propagates through a series of beam splitters, mirrors, iris and lenses to enter the monochromator (SP2558 Princeton Instruments). This intensity is finally plotted w.r.t. the wavelength.

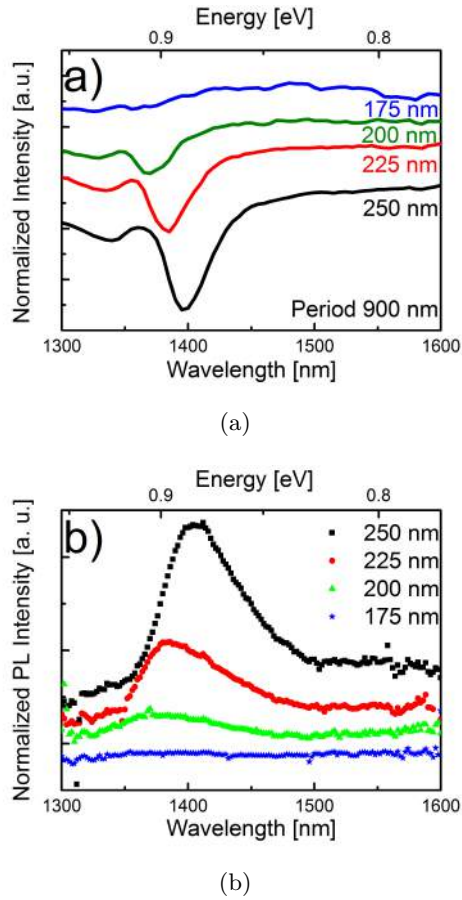


**Figure 3.21.:** (a) Transmission measurement and corresponding (b) PL spectra of samples comprising of varying antenna diameters from 175 nm to 250 nm. The increase in size gives a red shift in transmission and PL peak position

### 3.4.3. Effect of change in size of disk shaped antennas

The disc shaped antennas with varying diameters of 250 nm, 225 nm, 200 nm and 175 nm with a quadratic periodicity of 900 nm are embedded in PMMA layer which contains PbS quantum dots. The resulting  $\mu$ -PL spectra (figure 3.21(b)) show rather broad enhanced emission peaks on top of the wide unperturbed PbS-particle emission with enhancement ratios of 3.35, 2.08, 1.37 and 1.13 for 250 nm, 225 nm, 200 nm and 175 nm antennas, respectively (table 3.2) with respect to PbS-PMMA background (i.e. without any Au nanoantennas). These also show a blue shift with decreasing diameter.

Comparing these emission spectra with the extinction from figure 3.21(a), a clear spectral correspondence of transmission dips (i.e. extinction peaks) and emission peaks is observed,

**Table 3.2.:** Enhancement Ratio values of sample's with varying disk diameter

| S.No. | Au Nanoantenna       | Peak Position  | Enhancement ratio<br>(w.r.t. PbS-PMMA background) |
|-------|----------------------|----------------|---|
| 1.    | $\varnothing$ 250 nm | 1404 nm        | 3.35  |
| 2.    | $\varnothing$ 225 nm | 1386 nm        | 2.08  |
| 3.    | $\varnothing$ 200 nm | $\sim$ 1370 nm | 1.37  |
| 4.    | $\varnothing$ 175 nm | $\sim$ 1367 nm | 1.13  |

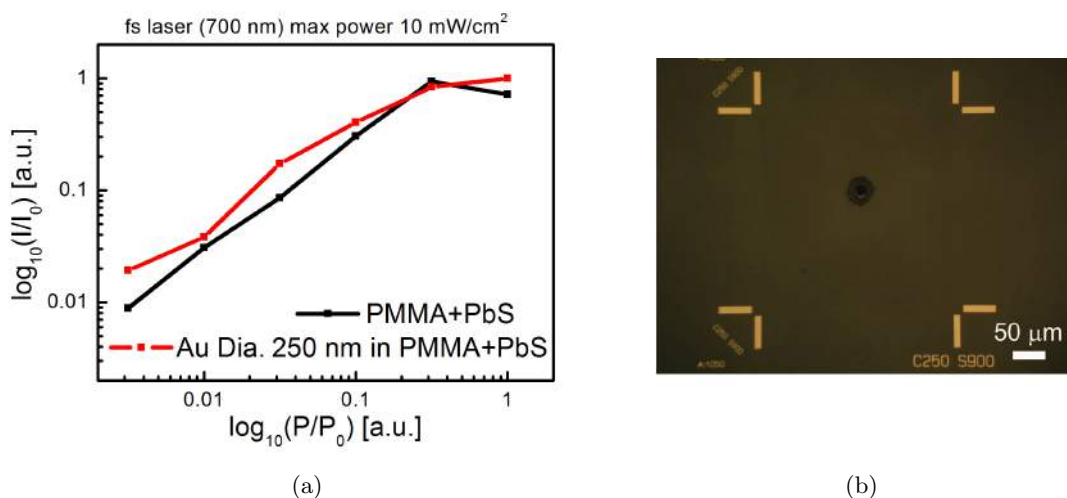


**Figure 3.22.:** Disk 250 nm with quadratic periodicty of 900 nm are pumped with laser (a) The experimental peak position of the PL curve obtained from area of sample with (red) and without (black) nanoantennas is plotted . The last point shows the breakdown power. (b) The corresponding light optical image of the burnt sample after breakdown.

plus, a similar behavior of enhancement of the spectra is seen. Apart from this, the blue shift of the peaks with decreasing particle size coincides with the original speculation of an emission enhancement due to collective particle plasmon oscillations of the nanoantennas.

Furthermore, to see the effect of optical pumping on the PbS-PMMA embedded samples, a chosen area with disc diameter of 250 nm and for reference, an area without any antennas is compared. Both these areas are pumped with 700 nm fs-laser, starting with lowest possible power to a maximum power of 10 mW/cm<sup>2</sup>. The PL intensity is plotted with respect to the log of pumping power (figure 3.22(a)). There is surely an increase in intensity of PL with increase in pumping power but still there is no distinct difference in the slopes of the line with Au antennas and that containing no antennas. The last point

of measurement shows the power at which the sample burns (shown in figure 3.22(b)), and hence, it is the maximum power that can be used for these samples.

The group of T.W. Odum reported in their paper by Zhou et al. [68], that they observed similar transmission dependence of the samples as done in this part of our work. However, they focused on shorter wavelengths and the SLR of their structures appeared around a wavelength of  $900\text{ nm}$ , which is a spectral range not yet applicable for Si-photonics. The advantage of this shorter wavelengths was, that they could use the laser dye IR-140 as efficient emitter [68]. For small excitation intensities, similar PL enhancement, is observed like for our PbS embedded nanoantenna arrays. However, increasing the excitation intensity (with fs-laser), they could demonstrate line narrowing and finally lasing from their nanoantenna arrays [68] while this was not observed in my PbS embedded nanoantenna array. The difference might lie in the quantum efficiency of the IR-140 dye with respect to the PbS quantum dots that were used differently.

#### 3.4.4. Effect of change in aspect ratio antennas

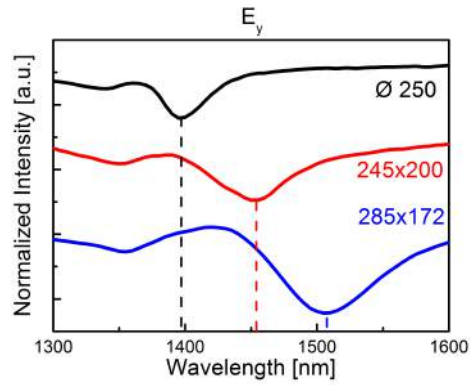
The disc shaped antennas with diameter of  $250\text{ nm}$  arranged with a quadratic periodicity of  $900\text{ nm}$  are compared with aspect ratio changed rectangular antennas  $245\text{ nm} \times 200\text{ nm}$  and  $285\text{ nm} \times 172\text{ nm}$ . All are embedded in PbS-PMMA layer of  $3.2 \pm 0.2\ \mu\text{m}$  thickness and then the samples are taken for  $\mu$ -PL measurement. The spectra show rather broad enhanced emission peaks (figure 3.23(b)) on top of the wide unperturbed PbS-particle emission as discussed in figure 3.11(a). Here, the PL spectra are normalized with the PL spectra received from unstructured area of the sample.

Also, no polarization dependency is shown here<sup>5</sup>, as a unpolarized laser is used. Comparing these emission spectra with the transmission from figure 3.17 and 3.18 a clear spectral correspondence of transmission dips (i.e. extinction peaks) and emission peaks can be observed. As the aspect ratio increases, there is a red shift in emission spectra of the PbS embedded in PMMA. This red shift corresponds to the red shift in the transmission spectra.

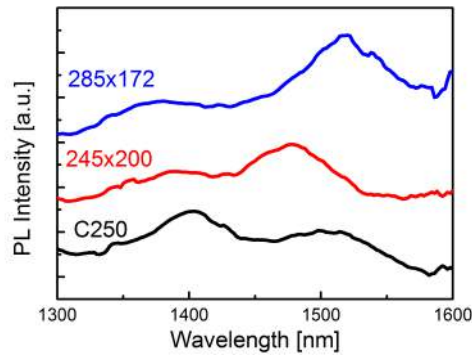
---

<sup>5</sup>Polarization dependence PL results showed no clear signs of contribution of the aspect ratio/directionality.

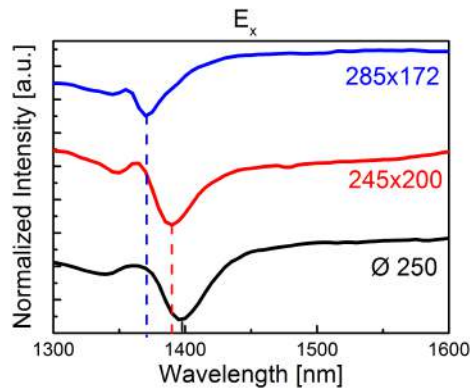
### 3.4. Optical characterization by photoluminescence measurements



(a)



(b)



(c)

**Figure 3.23.:** Comparison of discs with diameter of 250 nm with rectangular antennas of increasing aspect ratio from 245 nm x 200 nm to 285 nm x 172 nm. (a) Transmission measurement for  $E_y$  polarization; (b) the corresponding PL spectra of all three samples. A red shift is observed with increasing aspect ratio and (c) Transmission measurement for  $E_x$  polarization.

## 3.5. Summary of Part II

In this section, coupling of nanoantennas in the IR regime has been studied. Three different experimental sets were investigated comprising of variation in size, periodicity and aspect ratio which have been analyzed to clarify the behavior of nanoantennas. In all the samples, a localized surface plasmon resonance of the single particles and a sharper surface lattice resonance exhibiting a fano line shape are clearly visible. The fano lines are formed due to coupling of localized surface plasmon resonance with a grating resonance and appear at the long wavelength side of the Raleigh anomaly.

A single particle resonance of a 250 nm disk centered at 1050 nm fits well with a Lorentzian curve. Two spectral features of (1,1) and (1,0) Raleigh anomaly (for 900 nm periodicity) are observed at 955 nm and 1350 nm with the surface lattice resonance to the red side of the Raleigh anomaly. On reducing the size of the disks (same periodicity), a blue shift of single particle resonance and a smaller blue shift of the surface lattice resonance are observed.

Increasing the periodicity, in just one direction, of nanoantenna disk (diameter 250 nm) arrays from 800 nm to 1000 nm, showed polarization dependent red shift of the Raleigh anomaly's and hence resulting in red shift of the surface lattice resonance by radiative coupling.

Further, when the aspect ratio of the antennas is increased (keeping the volume same as that of disks and the electric field of incident light parallel to the longer axis), a red shift is observed, again depending on the polarization of the incident light. The far field coupling between the adjacent nanoantennas is confirmed due to the distant charge coupling in direction perpendicular to the oscillation.

Finally, the micro-photoluminescence measurements using PbS quantum dots embedded in PMMA to embed the nanoantenna samples, show similar trends as that for transmission. Decreasing size shows blue shift with reduction in intensity, while increasing the aspect ratio shows a red shift in PL intensity around the resonance frequency of PbS.

## 4. Overall Summary and Outlook

In this work, several strategies to control the dispersion of surface plasmons on gold layers and antennas have been explored. The experimental data were mainly compared with simple theoretical calculations based on effective medium theories and Mie theory which showed already good agreement with the experiment.

In the first part, the possibility to tune the SP dispersion towards the near IR is successfully explored by changing the porosity of metal. The tendency of a red shift of the dispersion was shown as a concept for nanoporous metals, it works in principle. However, porosities are not high enough to shift the limiting SP-frequency  $\omega_{sp}$  into near IR. Although, the limiting SP-frequency  $\omega_{sp}$  at the nanoporous Au/Si interface should shift to  $1.1\text{ eV}$  and coincide with the spectral range of silicon luminescence, an enhancement of the Si luminescence could not be clearly observed. To extend the surface plasmons resonances further to the IR and make it potentially attractive for applications in Si photonics, arrays of nanoantennas were investigated.

By changing size, periodicity and aspect ratio of Au-nanoantennas the tunability of localized surface plasmon resonances (LSPR) and surface lattice resonances (SLR) is investigated. A red shift of single particle resonances is seen by increasing the size of the Au-disks from  $150\text{ nm}$  to  $250\text{ nm}$ . Increasing the periodicity in one dimension showed the effect of the radiative coupling between the nanoantennas having a direct impact on the spectral position of the Rayleigh anomaly (RA), and hence, shifting the surface lattice resonance to the red side. Finally, the red shift of surface lattice resonance was shown for samples with higher aspect ratio for polarization along the long axis. These results were used in conjunction with PbS-quantum dots embedded in PMMA to investigate the luminescence enhancement connected with the surface lattice resonance. Indeed, 3.4 folds enhancement at wavelengths around  $1400\text{ nm}$  was observed and its dependence on the surface lattice resonance was confirmed by comparing the spectral shift in micro-photoluminescence spectra with the surface lattice resonance shift in transmission spectra for different nanoantenna arrays.

This study has shown that surface plasmon dispersion and resonances can be tuned effectively from the visible to the near infra red using nanoporosity and nanoantenna

arrays. This tunability might be the basis for the future combination of the areas of plasmonics with the field of Si-photonics.

**Outlook:** Basic principles for the tunability of dispersion relation have been successfully explained in this thesis, and they have worked in principle. But still there is lot of scope for further improvements.

For example, a possibility of continuing this work by carrying out polarization dependence of PL spectra for changing periodicity and aspect ratio samples would be good to understand which direction contributes more to the PL and how it grows with the transmission data. Furthermore, other coupling quantum dots and/or dyes which would have higher quantum efficiencies in the IR region should be used, to see if lasing is possible for nanoantenna arrays within the near IR.

1. Also, for more realistic experimentation with view towards Si waveguides, it would be good to work with Si and not glass. But with the knowledge of the results shown in this thesis, such structures can be put on oxidized Si waveguides. Such an arrangement is expected to couple the radiation fields into the Si waveguides.
2. Other idea would be to bring together the near and far field effects using double antennas together with radiative coupling. This is expected to give higher enhancement effects. A total enhancement like this, would create not just near fields, but also, hot spots for Raman detection.
3. Another aspect which has not been addressed in this thesis, is the influence of other metals with a more industrial application point of view. It is known that, Au has diffusion problems when directly coupled with Si. It has been estimated by Boltasseva [29] group that TiN could outperform the plasmonic properties of Au, so it would be really good for semiconductor industry applications while avoiding the Si poisoning. Nevertheless, the basic principles of physics from the work of this thesis would be still valid and can be easily extended to other plasmonic systems like TiN, Al doped ZnO, etc.

# Appendices

# A. Wave equation to surface plasmon equation

In absence of external charge and current the maxwell equations reduce to [7–9]:

$$\Delta X \Delta X E = -\mu_0 \left( \frac{\partial^2 D}{\partial t^2} \right); \quad (\text{A.1})$$

Using mathematical identities and remembering that due to absence of external field  $\Delta \cdot D = 0$ , and there is negligible change of dielectric profile  $\varepsilon = \varepsilon(r)$  over distances on the order of one optical wavelength, we get:

$$\Delta^2 E - \varepsilon/c \frac{\partial^2 E}{\partial t^2} = 0; \quad (\text{A.2})$$

This equation can be solved separately for regions of constant  $\varepsilon$ . A harmonic time dependency of electric field is assumed with  $E(r, t) = E(r)e^{(-i\omega t)}$  to yield the Helmholtz equation.

$$\Delta^2 E + k_0^2 \varepsilon E = 0; \quad (\text{A.3})$$

A one dimensional case (i.e.  $\varepsilon$  depends only on one coordinate) is studied here. The propagation of wave is along x-direction, and no spatial variation along y-direction, therefore,  $\varepsilon = \varepsilon(z)$ .

Propagating wave can be defines as  $E(x, y, z) = E(z)e^{(ik_x x)}$ , where  $\beta = k_x$  is the propagation constant corresponding to the wave vector in the direction of propagation.

$$\frac{\partial^2 E(z)}{\partial z^2} + (k_0^2 \varepsilon - k_x^2) E = 0; \quad (\text{A.4})$$

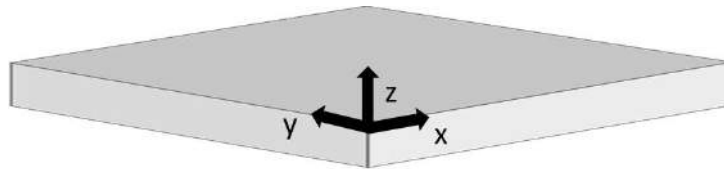


*Figure A.1.: 1D wave propagation geometry, with wave propagating along x-direction*

This equation gives the general solution of guided electromagnetic waves. Due to symmetricity, the different components of E and H can be found as

$$\frac{\partial^2 E_x}{\partial z^2} - \frac{\partial^2 E_z}{\partial x^2} = i\omega\mu_0 H_y; \quad \frac{\partial^2 H_x}{\partial z^2} - \frac{\partial^2 H_z}{\partial x^2} = -i\omega\varepsilon\varepsilon_0 E_y; \quad (\text{A.5})$$

These two equations are symmetric in x,y,z and their corresponding equations can be achieved by replacing x with y and y with z in rotation. The above equations can be simplified by introducing the two facts

- i. Wave propagation in x direction gives  $\frac{\partial}{\partial x} = ik_x$  and
- ii. Homogeneity in y-direction gives  $\frac{\partial}{\partial y} = 0$ .

The solutions hence would show two sets of self consistent solutions with different polarization properties of propagating waves.

## A.1. TM or P modes

These modes are defined as  $E_x, E_z$  and  $H_y \neq 0$ , the governing equations reduce for TM modes to

$$E_x = -i \frac{1}{\omega\varepsilon\varepsilon_0} \frac{\partial H_y}{\partial z}; \quad E_z = -\frac{k_x}{\omega\varepsilon\varepsilon_0} H_y; \quad (\text{A.6})$$

and hence the wave equation is

$$\frac{\partial^2 H_y}{\partial z^2} + (k_0^2 \varepsilon - k_x^2) H_y = 0; \quad (\text{A.7})$$

Considering, surface plasmon propagation at a single flat interface between a dielectric ( $\varepsilon_2, z>0$ ) and conducting half space ( $\varepsilon_1, z<0$ ). Then, the propagating wave solutions confined to the interface in TM solutions for  $z > 0$  are given from equation A.7

$$H_y(z) = A_2 e^{ik_x x - k_2 z}; \quad (\text{A.8a})$$

$$E_x(z) = -iA_2 \frac{k_2}{\omega\varepsilon_0\varepsilon_2} e^{ik_x x - k_2 z}; \quad (\text{A.8b})$$

$$E_z(z) = -A_1 \frac{\beta}{\omega\varepsilon_0\varepsilon_2} e^{ik_x x - k_2 z}; \quad (\text{A.8c})$$

## A. Wave equation to surface plasmon equation

---

For  $z < 0$ , and  $k_i = k_{z,i}$  ( $i = 1, 2$ ) is the component of wave vector perpendicular to the interface in the two media.

$$H_y(z) = A_1 e^{ik_x x - k_1 z}; \quad (\text{A.9a})$$

$$E_x(z) = -iA_1 \frac{k_1}{\omega \varepsilon_0 \varepsilon_1} e^{ik_x x - k_1 z}; \quad (\text{A.9b})$$

$$E_z(z) = -A_1 \frac{k_x}{\omega \varepsilon_0 \varepsilon_1} e^{ik_x x - k_1 z}; \quad (\text{A.9c})$$

Continuity of  $H_y$  and  $\varepsilon_i E_z$ ; and at interface

$$A_1 = A_2 \quad (\text{A.10a})$$

$$\frac{k_2}{k_1} = -\frac{\varepsilon_2}{\varepsilon_1} \quad (\text{A.10b})$$

Furthermore, the confinement of the wave to the surface means, that the real part of the dielectric properties between material interface are of opposite signs, i.e.  $Re[\varepsilon_1] < 0$  if  $\varepsilon_2 > 0$ .

Now, equation A.7 yields:

$$k_1^2 = k_x^2 - k_0^2 \varepsilon_1 \quad (\text{A.11a})$$

$$k_2^2 = k_x^2 - k_0^2 \varepsilon_2 \quad (\text{A.11b})$$

From equations A.10 and A.11, we get

$$k_x = k_0 \sqrt{\frac{\varepsilon_1 * \varepsilon_2}{\varepsilon_1 + \varepsilon_2}} \quad (\text{A.12})$$

where,  $\varepsilon_2$  is a complex entity, therefore,  $\beta$  is also complex. The above equations are for wave vector along x-direction. Similarly, solving for wave-vector along z-direction, we get

$$k_{zi} = k_0 \sqrt{\frac{\varepsilon_i^2}{\varepsilon_1 + \varepsilon_2}} \quad (\text{A.13})$$

where, i can be either 1 (metal) or 2 (dielectric), depending on the region of interest.

For Bound modes,  $k_{zi}$  should be imaginary with  $\varepsilon_1 + \varepsilon_2 < 0$

and  $k_{zi} = \pm \sqrt{(\varepsilon_i * k_0^2) - k_x^2} \Rightarrow |k_x| > k_0 * \sqrt{\varepsilon_i}$  where the + is for  $z < 0$  and - for  $z > 0$ .

Also,  $k_x$  should be real, so  $\varepsilon_1 < 0$  all this together gives a condition for bound surface plasmon mode as  $\varepsilon_1 < -\varepsilon_2$

## A.2. TE or S modes

In these modes  $H_x, H_z$  and  $E_y \neq 0$ , As above

$$\frac{\partial^2 E_y}{\partial z^2} + (k_0^2 \varepsilon - k_x^2) E_y = 0; \quad (\text{A.14})$$

For  $z > 0$ :

$$E_y(z) = A_2 e^{ik_x x - k_2 z}; \quad (\text{A.15a})$$

$$H_x(z) = -i A_2 \frac{k_2}{\omega \mu_0} e^{ik_x x - k_2 z}; \quad (\text{A.15b})$$

$$H_z(z) = A_2 \frac{k_x}{\omega \mu_0} e^{ik_x x - k_2 z}; \quad (\text{A.15c})$$

For  $z < 0$ :

$$E_y(z) = A_1 e^{ik_x x + k_1 z}; \quad (\text{A.16a})$$

$$H_x(z) = i A_1 \frac{k_1}{\omega \mu_0} e^{ik_x x + k_1 z}; \quad (\text{A.16b})$$

$$H_z(z) = A_1 \frac{k_x}{\omega \mu_0} e^{ik_x x + k_1 z}; \quad (\text{A.16c})$$

Continuity at the interface for  $E_y$  and  $H_x$  leads to  $A_1(k_1 + k_2) = 0$ . Also for the confinement condition to be fulfilled  $Re[k_1] > 0$  and  $Re[k_2] > 0$ , which is possible for  $A_1 = A_2 = 0$ . Therefore, no surface modes exist for TE polarization, and surface plasmon polaritons exist only for TM polarization.

## B. Dispersion relation in MATLAB

### B.1. Angle resolved simulation by Bruggeman and Maxwell-Garnett Model

#### Angle resolved simulation by Bruggeman Model

```
e3=1;
eair=1;
e1=2.25;
d=120;
ed=eair;
c=3*10^17; % vel of light in nm/s
g1=42*pi/180;
g2=60*pi/180;
s=1*pi/180;
theta=g1:s:g2;
hold on
%fid = fopen('e_per_lambda.txt','a+');
epsinfinity=1.53;lambdap=145;gammap=17000;A1=.94;
phi1=-pi/4;lambda1=468;
gamma1=2300;A2=1.36;phi2=-pi/4;lambda2=331;
gamma2=940;
for ii=1:340
lambdaa(ii)=200+ii*(1400-200)/340;
lambda=lambdaa(ii);
epsilon(ii)=epsinfinity-1/lambdap^2/(1/lambda^2+sqrt(-1)/gammap/lambda)+
A1/lambda1*((exp(sqrt(-1)*phi1)/(1/lambda1-1/lambda-sqrt(-1)/gamma1)+
(exp(-sqrt(-1)*phi1)/(1/lambda1+1/lambda+sqrt(-1)/gamma1))))+
A2/lambda2*((exp(sqrt(-1)*phi2)/(1/lambda2-1/lambda-sqrt(-1)/gamma2)+
(exp(-sqrt(-1)*phi2)/(1/lambda2+1/lambda+sqrt(-1)/gamma2))));
e2=epsilon(ii);
```

```

w=2*pi*c/lambda; % omega
f=0.5;% f=1 means 100 % pure gold
M=(3*f-1)*e2+(2-3*f)*e3;
v=(M^2)+8*e2*e3;
vol=imag(v^0.5);
%mol=imag(M);
if vol<0
    e2brug=(M-(v^0.5))/4;
else
    e2brug=(M+(v^0.5))/4;
end
kx=(w/c)*((e1)^0.5)*sin(g1); % +ve
kz1=(((w^2/c^2)*e1)-kx^2)^0.5; %(is real number)
kz2=(((w^2/c^2)*e2brug)-kx^2)^0.5; %(is a Complex no.)
kz3=(((w^2/c^2)*e3)-kx^2)^0.5; %(should be purely imaginary)
A=(1-((kz2*e1)/(kz1*e2brug)))-(1+((kz2*e1)/(kz1*e2brug))*
(kz3*e2brug-kz2*e3)/(kz3*e2brug+kz2*e3)*exp(2i*kz2*d);
B=(1+((kz2*e1)/(kz1*e2brug)))-(1-((kz2*e1)/(kz1*e2brug))*
(kz3*e2brug-kz2*e3)/(kz3*e2brug+kz2*e3)*exp(2i*kz2*d);
Hry =A/B;
y=abs(Hry);
x=lambda;
%fprintf(fid,'%E\n',x);
plot(x,y);
end
%fclose(fid);

```

## Angle resolved simulation by Maxwell-Garnett Model

```

d=60;% thickness of layer in nm
c=3*10^17; % vel of light in nm/s
e1=2.25; % epsilon for glass
eair=1;e3=eair;ed=eair; % epsilon value of air
t1=42*pi/180;
t2=57*pi/180;
s=1*pi/180;

```

## B. Dispersion relation in MATLAB

---

```
theta=t1;%:s:t2;
f=0.50;% percentage of air
hold on
epsinfinity=1.53;lambdap=145;gammap=17000;A1=.94;
phi1=-pi/4;lambda1=468;
gamma1=2300;A2=1.36;phi2=-pi/4;lambda2=331;
gamma2=940;
for ii=1:540
lambda(ii)=496.28+ii*(2000-496.28)/540;
lambda=lambda(ii);
epsilon(ii)=epsinfinity-
1/lambdap^2/(1/lambda^2+sqrt(-1)/gammap/lambda)+
A1/lambda1*((exp(sqrt(-1)*phi1)/(1/lambda1-1/lambda-sqrt(-1)/gamma1)+
(exp(-sqrt(-1)*phi1)/(1/lambda1+1/lambda+sqrt(-1)/gamma1))))+
A2/lambda2*((exp(sqrt(-1)*phi2)/(1/lambda2-1/lambda-sqrt(-1)/gamma2)+
(exp(-sqrt(-1)*phi2)/(1/lambda2+1/lambda+sqrt(-1)/gamma2)))));
egold=epsilon(ii);
e_ll=f*ear+(1-f)*egold;
e_per=egold*((1+f)*ear+(1-f)*egold)/((1-f)*ear+(1+f)*egold);
w=2*pi*c/lambda; % omega
for g=1:length(theta);
g1=theta(g);
kx=(w/c)*((e1)^0.5)*sin(g1);
kz3=((w^2/c^2)*ed-kx^2)^0.5;
kz2=((w^2/c^2)*e_per)-(e_per/e_ll)*kx^2)^0.5;
kz1 =(((w^2/c^2)*e1)-kx^2)^0.5; %(is real number)
A=(1-((kz2*e1)/(kz1*e_per)))- (1+((kz2*e1)/(kz1*e_per)))*
(kz3*e_per-kz2*e3)/(kz3*e_per+kz2*e3)*exp(2i*kz2*d);
B=(1+((kz2*e1)/(kz1*e_per)))- (1-((kz2*e1)/(kz1*e_per)))*
(kz3*e_per-kz2*e3)/(kz3*e_per+kz2*e3)*exp(2i*kz2*d);
Hry =A/B;
x=lambda;
y=abs(Hry);
plot(x,y);
end
```

## B.2. Wave vector by Bruggeman and Maxwell-Garnett Model

### Wave vector by Bruggeman model

```

%Defining variables
d=120;% thickness of layer in mm
c=3*10^17;% vel of light in mm/s %e1=2.25; % epsilon for Ge
e3=1; % epsilon value of Si 12.25
e4=1;
hold on
%fid = fopen('Au60min_x2.txt','a+');
epsinfinity = 1.53; lambdap = 145; gammap = 17000; A1 = .94;
phi1 = -pi/4; lambda1 = 468;
gamma1 = 2300; A2 = 1.36; phi2 = -pi/4; lambda2 = 331;
gamma2 = 940;
for ii = 1:300
lambdaa(ii) = 400 + ii * (1900 - 400) / 300;
lambda = 780; %lambdaa(ii);
epsilon(ii) = epsinfinity -
1/lambdap^2 / (1/lambda^2 + sqrt(-1)/gammap/lambda) +
A1/lambda1 * ((exp(sqrt(-1)*phi1)/(1/lambda1 - 1/lambda - sqrt(-1)/gamma1) +
(exp(-sqrt(-1)*phi1)/(1/lambda1 + 1/lambda + sqrt(-1)/gamma1)))) +
A2/lambda2 * ((exp(sqrt(-1)*phi2)/(1/lambda2 - 1/lambda - sqrt(-1)/gamma2) +
(exp(-sqrt(-1)*phi2)/(1/lambda2 + 1/lambda + sqrt(-1)/gamma2))));
e2 = complex(real(epsilon(ii)), imag(epsilon(ii)));
w = 2*pi*c/lambda;
    f = 0.5; % f=1 means 100 % pure gold
    M = (3*f - 1)*e2 + (2 - 3*f)*e4;
    v = (M^2) + 8*e2*e4;
    vol = imag(v^0.5);
    if vol < 0
        e2brug = (M - (v^0.5)) / 4;
    else
        e2brug = (M + (v^0.5)) / 4;
    end
end

```

## B. Dispersion relation in MATLAB

---

```
A=(e2brug*e3)/(e3+e2brug);
kx=(w/c)*(A^0.5)*10^3;

x=real(kx)
y=1240.7/lambda;
%fprintf(fid,'%E\n',x);
plot(x,y);
end
%fclose(fid);
```

## Wave vector by Maxwell-Garnett Model

```
ear=1;
f=0.5;%percentage of air
ed=ear;
c=3*10^17;% vel of light in nm/s
hold on
%fid = fopen('e_per_lambda.txt','a+');
epsinfinity = 1.53; lambdap=145; gammap=17000; A1=.94;
phi1=-pi/4; lambda1=468;
gamma1=2300; A2=1.36; phi2=-pi/4; lambda2=331;
gamma2=940;
for ii=1:340
lambdaa(ii)=200+ii*(1900-200)/340;
lambda=780;%lambdaa(ii);
epsilon(ii)=epsinfinity -
1/lambdap^2/(1/lambda^2+sqrt(-1)/gammap/lambda)+
A1/lambda1*((exp(sqrt(-1)*phi1)/(1/lambda1-1/lambda-sqrt(-1)/gamma1)+
(exp(-sqrt(-1)*phi1)/(1/lambda1+1/lambda+sqrt(-1)/gamma1))))+
A2/lambda2*((exp(sqrt(-1)*phi2)/(1/lambda2-1/lambda-sqrt(-1)/gamma2)+
(exp(-sqrt(-1)*phi2)/(1/lambda2+1/lambda+sqrt(-1)/gamma2))));
egold=epsilon(ii);
e_ll=f*ear+(1-f)*egold;
e_per=egold*(((1+f)*ear+(1-f)*egold)/((1-f)*ear+(1+f)*egold));
w=2*pi*c/lambda;% omega
A=ed-e_per;
```

```

B=ed-(e_ll*e_per/ed);
kx=(w/c)*((e_ll*A/B)^0.5);
kzd=(((w^2/c^2)*ed)-kx^2)^0.5;
kzm=(((w^2/c^2)*e_per)-(e_per/e_ll)*kx^2)^0.5;
%y=real(e_per);
y=1240.7/lambda;
x=real(kx)
%fprintf(fid,'%E\n',x);
plot(x,y);
end
%fclose(fid);

```

### B.3. Transmission Calculation

```

%Defining variables
clear all
d=120;% thickness of layer in mm
c=3*10^17;% vel of light in mm/s
e1=1;% epsilon for glass
e3=1;% epsilon value of air
t1=0;
theta=t1;
g1=theta;%:s:t2;
hold on
fid = fopen('Trans_Au46_y.txt','a+');
epsinfinity = 1.53; lambdap = 145; gammap = 17000; A1 = .94; phi1 = -pi/4;
lambda1 = 468; gamma1 = 2300; A2 = 1.36; phi2 = -pi/4; lambda2 = 331; gamma2 = 940;
for ii = 1:700
lambdaa(ii) = 300 + ii * (1800 - 300) / 700;
lambda = lambdaa(ii);
epsilon(ii) = epsinfinity - 1/lambdap^2 / (1/lambda^2 + sqrt(-1)/gammap/lambda) +
A1/lambda1 * ((exp(sqrt(-1)*phi1)/(1/lambda1 - 1/lambda - sqrt(-1)/gamma1) +
(exp(-sqrt(-1)*phi1)/(1/lambda1 + 1/lambda + sqrt(-1)/gamma1)))) +
A2/lambda2 * ((exp(sqrt(-1)*phi2)/(1/lambda2 - 1/lambda - sqrt(-1)/gamma2) +
(exp(-sqrt(-1)*phi2)/(1/lambda2 + 1/lambda + sqrt(-1)/gamma2))));
e2 = complex(real(epsilon(ii)), imag(epsilon(ii)));

```

## B. Dispersion relation in MATLAB

---

```
%for jj=1:100
%   theta(jj)=42+jj*(52-42)/100;
%for g=1:length(theta);
    w=2*pi*c/lambda; % omega
    f=0.5;% f=1 means 100 % pure gold
    M=(3*f-1)*e2+(2-3*f)*e3;
    v=(M^2)+8*e2*e3;
    vol=imag(v^0.5);
    %mol=imag(M);
    if vol<0
        e2brug=(M-(v^0.5))/4;
    else
        e2brug=(M+(v^0.5))/4;
    end
    RE=(real(e2brug))^2;
    IE=(imag(e2brug))^2;
    UN = RE + IE;
    n=(0.5* ( UN^0.5 + RE^0.5 ))^0.5;
    s=(0.5* ( UN^0.5 - RE^0.5 ))^0.5;
    t1=2*3.5/(3.5+n);
    t3=2*n/(1+n);
    g1=0;%theta(g);
    kx=(w/c)*((e1)^0.5)*sin(g1); % +ve
    %kz1 =(((w^2/c^2)*e1)-kx^2)^0.5; %(is real number)
    kz2 =(((w^2/c^2)*e2brug)-kx^2)^0.5; %(is a Complex no.)
    %kz3 =(((w^2/c^2)*e3)-kx^2)^0.5; %(should be purely imaginary)
    Int=(t1*t3*exp(-imag(kz2)*d))^2;
    x=lambda;%g1;
    y=Int;
    %axis([300 1800 0 0.2])
    %fprintf(fid,'%E\n',y);
    plot(x,y);
% end
end
%fclose(fid);
```

## Bibliography

- [1] E. Ozbay, "Plasmonics: merging photonics and electronics at nanoscale dimensions," *Science*, vol. 311, pp. 189–193, 2006.
- [2] C. N. R. Rao, A. Müller, and A. K. Cheetham, *The Chemistry of Nanomaterials: Synthesis, Properties and Applications*. Wiley-VCH Verlag GmbH, Germany, 2004.
- [3] K. D. Sattler, ed., *Handbook of Nanophysics: Functional Nanomaterials*. CRC Press, 2010.
- [4] J. W. Steed and P. A. Gale, eds., *Supramolecular Chemistry: From Molecules to Nanomaterials*, vol. 8. John Wiley & Sons Ltd, 2012.
- [5] V. I. Gavrilenko, *Optics of Nanomaterials*. Pan Stanford, 2010.
- [6] H. Wang, D. W. Brandl, P. Nordlander, and N. J. Halas, "Plasmonic nanostructures: artificial molecules," *Acc. Chem. Res.*, vol. 40, pp. 53–62, 2007.
- [7] B. A. E. Saleh and M. C. Teich, *Fundamentals of photonics*. John Wiley & Sons Inc, 2007.
- [8] S. A. Maier, *Plasmonics: Fundamentals and Applications*. Springer, 2007.
- [9] H. Raether, *Surface Plasmons on smooth and rough surfaces and on gratings*, vol. 111. Springer-Verlag, 1988.
- [10] S. A. Maier, P. G. Kik, H. A. Atwater, S. Meltzer, E. Harel, B. E. Koel, and A. A. G. Requicha, "Local detection of electromagnetic energy transport below the diffraction limit in metal nanoparticle plasmon waveguides," *Nat. Mater.*, vol. 2, no. 4, pp. 229 – 232, 2003.
- [11] T. Nikolajsen, K. Leosson, I. Salakhutdinov, and S. I. Bozhevolnyi, "Polymer-based surface-plasmon-polariton stripe waveguides at telecommunication wavelengths," *App. Phys. Lett.*, vol. 82, no. 5, pp. 668–670, 2003.
- [12] C. Reinhardt, A. Seidel, A. B. Evlyukhin, W. Cheng, and B. N. Chichkov, "Mode-selective excitation of laser-written dielectric-loaded surface plasmon polariton waveguides," *J. Opt. Soc. Am. B*, vol. 26, pp. B55–B60, 2009.
- [13] C. Reinhardt, A. Seidel, A. B. Evlyukhin, W. Cheng, R. Kiyan, and B. N. Chichkov, "Direct laser-writing of dielectric-loaded surface plasmon-polariton waveguides for the visible and near infrared," *Appl. Phys. A*, vol. 100, pp. 347–352, 2010.
- [14] S. R. K. Rodriguez, S. Murai, M. A. Verschuuren, and J. G. Rivas, "Light-emitting waveguide-plasmon polaritons," *Phys. Rev. Lett.*, vol. 109, no. 16, p. 166803, 2012.
- [15] S. Murai, M. A. Verschuuren, G. Lozano, G. Pirruccio, S. R. K. Rodriguez, and J. G. Rivas, "Hybrid plasmonic photonic modes in diffractive arrays of nanoparticles coupled to light emitting optical waveguides," *Opt. Express*, vol. 21, pp. 4250–4262, 2013.

- [16] C. Reinhardt, A. Evlyukhin, W. Cheng, T. Birr, A. Markov, B. Ung, M. Skrobogatiy, and B. Chichkov, "Bandgap-confined large-mode waveguides for surface plasmon-polaritons," *JOSA B*, vol. 30, pp. 2898–2905, 2013.
- [17] S. I. Bozhevolnyi, V. S. Volkov, E. Devaux, J. Y. Laluet, and T. W. Ebbesen, "Channel plasmon subwavelength waveguide components including interferometers and ring resonators," *Nature*, vol. 440, pp. 508–511, 2006.
- [18] D. J. Bergman and M. I. Stockman, "Surface plasmon amplification by stimulated emission of radiation: Quantum generation of coherent surface plasmons in nanosystems," *Phys. Rev. Lett.*, vol. 90, no. 2, p. 027402, 2003.
- [19] B. Steinberger, A. Hohenau, H. Ditlbacher, L. Stepanov, A. Drezet, F. R. Aussenegg, A. Leitner, and J. R. Krenn, "Dielectric stripes on gold as surface plasmon waveguides," *App. Phys. Lett.*, vol. 88, no. 9, p. 094104, 2006.
- [20] A. Alù and N. Engheta, "Tuning the scattering response of optical nanoantennas with nanocircuit loads," *Nat. Photonics*, vol. 2, no. 5, pp. 305–310, 2008.
- [21] J. B. Pendry, "Negative refraction makes a perfect lens," *Phys. Rev. Lett.*, vol. 85, no. 18, pp. 3966–69, 2000.
- [22] X. Zhang and Z. Liu, "Superlenses to overcome the diffraction limit," *Nat. Mater.*, vol. 7, pp. 435–441, 2008.
- [23] S. Kawata, Y. Inouye, and P. Verma, "Plasmonics for near-field nano-imaging and superlensing," *Nat. Photonics*, vol. 3, no. 7, pp. 388–394, 2009.
- [24] J. Homola, S. Yee, and G. Gauglitz, "Surface plasmon resonance sensors: review," *Sensor Acutat B- Chem*, vol. 54, no. 1, pp. 3–15, 1999.
- [25] A. I. Kuznetsov, A. B. Evlyukhin, M. R. Goncalves, C. Reinhardt, A. Koroleva, M. L. Arnedillo, R. Kiyam, O. Marti, and B. N. Chichkov, "Laser fabrication of large-scale nanoparticle arrays for sensing applications," *ACS Nano.*, vol. 5, no. 6, pp. 4843–4849, 2011.
- [26] R. W. Ziolkowski, "Propagation in and scattering from a matched metamaterial having a zero index of refraction," *Phys. Rev. E*, vol. 70, p. 046608, 2004.
- [27] A. Alù and N. Engheta, "Achieving transparency with plasmonic and metamaterial coatings," *Phys. Rev. E*, vol. 72, p. 016623, 2005.
- [28] J. B. Khurgin and A. Boltasseva, "Reflecting upon the losses in plasmonics and metamaterials," *MRS Bulletin*, vol. 37, pp. 768–779, 2012.
- [29] G. Naik, V. Shalaev, and A. Boltasseva, "Alternative plasmonic materials: Beyond gold and silver," *Adv. Mater.*, vol. 25, pp. 3264–3294, 2013.
- [30] C. Ji and P. Searson, "Fabrication of nanoporous gold nanowires," *Appl. Phys. Lett.*, vol. 81, no. 23, pp. 4437–4439, 2002.
- [31] Y. Ding, Y. J. Kim, and J. Erlebacher, "Nanoporous gold leaf: "ancient technology"/advanced material," *Adv. Mater.*, vol. 16, pp. 1897–1900, 2004.

- [32] M. Dixon, T. Daniel, M. Hieda, D. Smilgies, M. Chan, and D. Allara, "Preparation, structure, and optical properties of nanoporous gold thin films," *J. Am. Chem. Soc.*, vol. 23(5), pp. 2414–2422, 2007.
- [33] T. Fujita, L. Qian, K. Inoke, J. Erlebacher, and M. Chen, "Three-dimensional morphology of nanoporous gold," *App*, vol. 92, p. 251902, 2008.
- [34] J. Pendry, L. Martin-Moreno, and F. J. Gracia-Vidal, "Mimicking surface plasmons with structured surfaces," *Science*, vol. 305, pp. 847–848, 2004.
- [35] A. P. Hibbins, B. R. Evans, and J. R. Sambles, "Experimental verification of designer surface plasmons," *Science*, vol. 308, pp. 670–672, 2005.
- [36] M. L. Nesterov, D. Martin-Cano, A. I. Fernandez-Dominguez, E. Moreno, L. Martin-Moreno, and F. J. Gracia-Vidal, "Geometrically induced modification of the surface plasmons in the optical and telecom regimes," *Opt. Lett.*, vol. 35, no. 3, pp. 423–425, 2010.
- [37] A. K. Sarychev and V. M. Shalaev, *Introduction to Complex Mediums for Optics and Electromagnetics*, vol. PM123, ch. Optical Properties of Metal-Dielectric Films, pp. 397–420. SPIE Press, Oct 2003.
- [38] S. Bozhevolnyi and F. García-Vidal, "Focus on plasmonics," *New J. Phys.*, vol. 10, p. 105001, 2008.
- [39] S. I. Bozhevolnyi, *Plasmonic Nanoguides and Circuits*. Pan Stanford: Singapore, 2009.
- [40] U. Kreibig and M. Vollmer, *Optical properties of metal clusters*. Springer-Verlag, 1995.
- [41] A. Drezet, A. Hohenau, A. Stepanov, H. Ditlbacher, B. Steinberger, N. Galler, F. Aussenegg, A. Leitner, and J. Krenn, "How to erase surface plasmon fringes," *App. Phys. Lett.*, vol. 89, p. 091117, 2006.
- [42] A. Drezet, A. Hohenau, D. Koller, A. Stepanov, H. Ditlbacher, B. Steinberger, F. Aussenegg, A. Leitner, and J. Krenn, "Leakage radiation microscopy of surface plasmon polaritons," *Mat. Sc. Engg., B*, vol. 149, pp. 220–229, 2008.
- [43] J. Garnett, "Colours in metal glasses and in metallic films," *Phil. Trans. R. Soc. Lond.*, vol. 203, pp. 385–420, 1904.
- [44] D. Bruggeman, "Berechnung verschiedener physikalischer konstanten von heterogenen substanzen," *Ann. Phys. (Leipzig)*, vol. 416, pp. 636–664, 1935.
- [45] C. Bohren and D. Huffmann, *Absorption and scattering of light by small particles*. Wiley -Interscience, 1983.
- [46] T. C. Choy, *Effective Medium Theory: Principles and Applications*. Oxford University Press, 1999.
- [47] K. Busch and C. Soukoulis, "Transport properties of random media: An energy-density cpa approach," *Phys. Rev. B*, vol. 54, pp. 893–899, 1996.

- [48] Z. Hashin and S. Shtrikman, “A variational approach to the theory of effective magnetic permeability of multiphase materials,” *J. Appl. Phys.*, vol. 33, no. 10, pp. 3125–3131, 1962.
- [49] A. Kirchner, K. Busch, and C. Soukoulis, “Transport properties of random arrays of dielectric cylinders,” *Phys. Rev. B*, vol. 57, pp. 277–288, 1997.
- [50] J. Kanungo and J. Schilling, “Experimental determination of the principal dielectric functions in silver nanowire metamaterials,” *App. Phys. Lett.*, vol. 97, p. 021903, 2010.
- [51] A. J. Forty, “Corrosion micromorphology of noble metal alloys and depletion gilding,” *Nature*, vol. 282, pp. 597–598, 1979.
- [52] M. J. Aziz, S. G. Corcoran, J. Erlebacher, R. C. Newman, and K. Sieradzki, “Alloy corrosion,” *MRS Bull.*, vol. 24, no. 7, p. 24, 1999.
- [53] F. Yu, S. Ahl, A. M. Caminade, J. P. Majoral, W. Knoll, and J. Erlebacher, “Simultaneous excitation of propagating and localized surface plasmon resonance in nanoporous gold membranes,” *Anal. Chem.*, vol. 78, pp. 7346–7350, 2006.
- [54] J. Erlebacher, M. Aziz, A. Karma, N. Dimitrov, and K. Sieradzki, “Evolution of nanoporosity in dealloying,” *Nature*, vol. 410, pp. 450–453, 2001.
- [55] E. Hecht and A. Ganesan, *Optics*. Pearson Education, 2009.
- [56] Z. Shi, G. Piredda, A. C. Liapis, M. A. Nelson, L. Novotny, and R. W. Boyd, “Surface-plasmon polaritons on metal-dielectric nanocomposite films,” *Opt. Lett.*, vol. 34, pp. 3535–3527, 2009.
- [57] N. Sardana, F. Heyroth, and J. Schilling, “Propagating surface plasmons on nanoporous gold,” *J. Opt. Soc. Am. B*, vol. 29, no. 7, pp. 1778–1783, 2012.
- [58] P. B. Johnson and R. W. Christy, “Optical constants of the noble metals,” *Phys. Rev. B*, vol. 6, pp. 4370–4379, 1972.
- [59] E. D. Palik, ed., *Handbook of optical constants of solids*. Academic Press Handbook Series, 1985.
- [60] E. Fontana and R. Pantell, “Characterization of multilayer rough surfaces by use of surface-plasmon spectroscopy,” *Phys. Rev. B*, vol. 37, pp. 3164–3182, 1988.
- [61] A. Hohenau, J. Krenn, A. Drezet, O. Mollet, S. Huant, C. Genet, B. Stein, and T. Ebbesen, “Surface plasmon leakage radiation microscopy at the diffraction limit,” *Opt. Express*, vol. 19, no. 25, pp. 25749–25762, 2011.
- [62] K. T. Carron, W. Fluhr, M. Meier, A. Wokaun, and H. W. Lehmann, “Resonances of two-dimensional particle gratings in surface-enhanced raman scattering,” *J. Opt. Soc. Am. B*, vol. 3, p. 430, 1986.
- [63] S. Bozhevolnyi, I. Smolyaninov, and A. Zayats, “Near-field microscopy of surface-plasmon polaritons: Localization and internal interface imaging,” *Phys. Rev. B*, vol. 51, pp. 17916–17924, 1995.

- [64] V. G. Kravets, F. Schedin, and A. N. Grigorenko, “Extremely narrow plasmon resonances based on diffraction coupling of localized plasmons in arrays of metallic nanoparticles,” *Phys. Rev. Lett.*, vol. 101, p. 087403, 2008.
- [65] A. Ghoshal, *Plasmon enhanced near-field Interactions in surface coupled nanoparticle arrays for integrated nanophotonic devices*. PhD thesis, College of Optics and Photonics at the University of Central Florida Orlando, Florida, 2010.
- [66] J. Zuloaga and P. Nordlander, “On the energy shift between near-field and far-field peak intensities in localized plasmon systems,” *Nano Lett.*, vol. 11, no. 3, pp. 1280–1283, 2011.
- [67] B. Auguie and W. L. Barnes, “Collective resonances in gold nanoparticle arrays,” *Phys. Rev. Lett.*, vol. 101, p. 143902, 2008.
- [68] W. Zhou, M. Diridi, J. Y. Suh, C. H. Kim, D. T. Co, M. R. Wasielewski, G. C. Schatz, and T. W. Odom, “Lasing action in strongly coupled plasmonic nanocavity arrays,” *Nat. Nanotech.*, vol. 8, pp. 506–511, 2013.
- [69] H. Frohlich, “Long range coherence and energy storage in biological systems,” *Int. J. Quantum Chem.*, vol. II, pp. 641–649, 1968.
- [70] U. Kreibig, “Hundert jahre mie-theorie,” *Phys. Unserer Zeit*, vol. 39, no. 6, pp. 281–287, 2008.
- [71] G. Mie, “Beitrage zur optik tr uber medien, speziell kolloidaler metallosungen,” *Ann. Phys.*, vol. 25, no. 3, pp. 377–445, 1908.
- [72] L. J. Battan, *Radar observations of the atmosphere*. University of Chicago, 1973.
- [73] A. Trugler, *Optical properties of metallic nanoparticles*. PhD thesis, Institut fur Physik, Fachbereich Theoretische Physik Karl-Franzens-Universitat Graz, 2011.
- [74] U. Hohenester and A. Trugler, “MNPBEM: A Matlab toolbox for the simulation of plasmonic nanoparticles,” *Comp. Phys. Commun.*, vol. 183, pp. 370–381, 2012.
- [75] H. Hertz, “The forces of electrical oscillations treated according to maxwells theory,” *Nature*, vol. 39, no. 402, pp. 450–452, 1889.
- [76] J. A. Stratton and L. J. Chu, “Diffraction theory of electromagnetic waves,” *Phys. Rev.*, vol. 56, pp. 99–107, 1939.
- [77] S. Silver, ed., *Microwave Antenna Theory and Design*, vol. 19. IET, illustrated ed., 1949.
- [78] R. Chatterjee, *Antenna Theory and Practice*. John Wiley & Sons Inc, 1988.
- [79] J. Jackson, *Classical Electrodynamics*. Wiley, 3 ed., 1999.
- [80] R. P. Feynman, *The Feynman Lectures on Physics*. Addison Wesley, 2006.
- [81] N. Félidj, J. Aubard, G. Lévi, J. Krenn, M. Salerno, G. Schider, B. Lamprecht, A. Leitner, and F. Aussenegg, “Controlling the optical response of regular arrays of gold particles for surface-enhanced raman scattering,” *Phys. Rev. B*, vol. 65, no. 7, p. 075419, 2002.

- [82] S. L. Zou and G. C. Schatz, “Narrow plasmonic/photonic extinction and scattering line shapes for one and two dimensional silver nanoparticle arrays,” *J. Chem. Phys.*, vol. 121, no. 24, pp. 12606–12612, 2004.
- [83] A. Ghoshal and P. G. Kik, “Excitation of propagating surface plasmons by a periodic nanoparticle array: Trade-off between particle-induced near-field excitation and damping,” *App. Phys. Lett.*, vol. 94, p. 251102, 2009.
- [84] S. Zou, N. Janel, and G. C. Schatz, “Silver nanoparticle array structures that produce remarkably narrow plasmon lineshapes,” *J. Chem. Phys.*, vol. 120, p. 10871, 2004.
- [85] L. A. Sweatlock, S. A. Maier, and H. A. Atwater, “Highly confined electromagnetic fields in arrays of strongly coupled ag nanoparticles,” *Phys. Rev. B*, vol. 71, p. 235408, 2005.
- [86] B. Auguie, X. M. Bendana, W. L. Barnes, and F. J. G. de Abajo, “Diffractive arrays of gold nanoparticles near an interface: Critical role of the substrate,” *Phys. Rev. B*, vol. 82, p. 155447, 2010.
- [87] X. M. Bendana, G. Lozano, G. Pirruccio, J. G. Rivas, and F. J. G. de Abajo, “Excitation of confined modes on particle arrays,” *Opt. Express*, vol. 21, no. 5, pp. 5636–5642, 2013.
- [88] W. Rechberger, A. Hohenau, A. Leitner, J. R. Krenn, B. Lamprecht, and F. R. Aussenegg, “Optical properties of two interacting gold nanoparticles,” *Optics Comm.*, vol. 220, pp. 137–141, 2003.
- [89] K. H. Su, Q. H. Wei, X. Zhang, J. Mock, D. R. Smith, and S. Schultz, “Interparticle coupling effects on plasmon resonances of nanogold particles,” *Nano Lett.*, vol. 3, no. 8, pp. 1087–1090, 2003.
- [90] P. Nordlander, C. Oubre, E. Prodan, K. Li, and M. I. Stockman, “Plasmon hybridization in nanoparticle dimers,” *Nano Lett.*, vol. 4, no. 5, pp. 899–903, 2004.
- [91] A. Vallecchi, S. Campione, and F. Capolino, “Symmetric and antisymmetric resonances in a pair of metal-dielectric nanoshells: tunability and closed-form formulas,” *J. Nanophotonics*, vol. 4, p. 041577, 2010.
- [92] W. Barnes, A. Dereux, and T. W. Ebbesen, “Surface plasmon subwavelength optics,” *Nature*, vol. 424, pp. 824–830, 2003.
- [93] S. V. Zhukovsky, V. E. Babicheva, A. V. Uskov, I. E. Protsenko, and A. V. Lavrinenko, “Enhanced electron photoemission by collective lattice resonances in plasmonic nanoparticle-array photodetectors and solar cells,” *Plasmonics*, vol. 9, no. 2, pp. 283–289, 2014.
- [94] S. V. Zhukovsky, V. E. Babicheva, A. V. Uskov, I. E. Protsenko, and A. V. Lavrinenko, “Electron photoemission in plasmonic nanoparticle arrays: analysis of collective resonances and embedding effects,” *Appl. Phys. A*, vol. 116, pp. 929–940, 2014.
- [95] L. Rayleigh, “On the dynamical theory of grating,” *Proc. R. Soc. A*, vol. 79, pp. 399–415, 1907.

- [96] G. Vecchi, V. Giannini, and J. G. Rivas, “Shaping the fluorescent emission by lattice resonances in plasmonic crystals of nanoantennas,” *PRL*, vol. 102, p. 146807, 2009.
- [97] G. Vecchi, V. Giannini, and J. G. Rivas, “Surface modes in plasmonic crystals induced by diffractive coupling of nanoantennas,” *Phys. Rev. B*, vol. 80, p. 201401, 2009.
- [98] S. R. K. Rodriguez, A. Abass, B. Maes, O. T. A. Janssen, G. Vecchi, and J. G. Rivas, “Coupling bright and dark plasmonic lattice resonances,” *Phys. Rev. X*, vol. 1, p. 021019, 2011.
- [99] C. C. Tannoudji, J. D. Roc, and G. Grynberg, *Atom Photon Interactions*. Wiley VCH, New York, 2004.
- [100] L. Novotny, “Strong coupling, energy splitting, and level crossings a classical perspective,” *Am. J. Phys.*, vol. 78, no. 11, p. 1199, 2010.
- [101] S. Mukherjee, H. Sobhani, J. B. Lassiter, R. Bardhan, P. Nordlander, and N. J. Halas, “Fano shells nanoparticles with built in fano resonances,” *Nano Lett.*, vol. 10, no. 7, p. 2694, 2010.
- [102] N. Tsukada and T. Ogawa, “Competition of the longitudinal resonance and the transverse resonance,” *Phys. Lett. A*, vol. 45, no. 2, pp. 159–160, 1973.
- [103] B. G. McMillan, L. E. A. Berlouis, F. R. Cruickshank, D. Pugh, and P. F. Brevet, “Transverse and longitudinal surface plasmon resonances of a hexagonal array of gold nanorods embedded in an alumina matrix,” *Appl. Phys. Lett.*, vol. 86, no. 21, p. 211912, 2005.



# List of Figures

|       |  |    |
|-------|--|----|
| 2.1.  | Schematic of surface plasmons at metal-dielectric interface . . . . .  | 5  |
| 2.2.  | Dispersion relation of surface plasmons at metal-dielectric interface . . . .  | 6  |
| 2.3.  | Dispersion relation of gold by hypothetically increasing porosity [ $\epsilon_{Au}$ (bulk black), $0.5 \epsilon_{Au}$ (50% porous blue) and $0.3 \epsilon_{Au}$ (80% porous red)] i.e. increasing $\epsilon_{eff}$ (less negative value) of nanoporous gold. Showing a red shift with increasing porosity. . . . .   | 8  |
| 2.4.  | Effective-medium theories basic unit cell [40, 46] . . . . .   | 10 |
| 2.5.  | Bruggeman flux deviation through inclusion [46] . . . . .  | 11 |
| 2.6.  | 2D Maxwell-Garnett model for a columnar structure showing the directions of $\epsilon_{\perp}$ and $\epsilon_{\parallel}$ . . . . .  | 13 |
| 2.7.  | SEM images of the dealloyed nanoporous gold samples. All structure sizes are considerably smaller than the wavelength of visible light . . . . .   | 16 |
| 2.8.  | Real and imaginary parts of the dielectric constant of the dealloyed nanoporous gold film (red) and of the evaporated bulk gold film (black) determined by spectroscopic ellipsometric measurements. . . . .   | 18 |
| 2.9.  | Comparison of the dielectric constants determined by ellipsometry from figure. 2.8 with calculated values using the Bruggeman theory (a) Real part of the dielectric constant of the nanoporous gold and bulk gold film as received from ellipsometric data (red solid line and dash-dot black line, respectively) and calculated using Bruggeman effective medium model (green dashed line and blue dotted line, respectively) and corresponding (b) imaginary part of dielectric constant. . . . .   | 19 |
| 2.10. | SEM images of the hexaporous gold samples. All structure sizes are considerably smaller than the wavelength of visible light . . . . .   | 21 |
| 2.11. | Schematic of wave vectors and their components at Au-air interface inside a prism . . . . .  | 23 |
| 2.12. | (a) Kretschmann configuration; (b) Probing of dispersion relation by altering angle of incidence in Kretschmann configuration . . . . .  | 24 |
| 2.13. | Schematic (top view) of setup for angle resolved spectroscopy measurements   | 25 |
| 2.14. | FIB milled slit on bulk gold as seen with the CCD. . . . .   | 26 |
| 2.15. | Schematic showing the contact layers of FIB milled sample, which mounted on the immersion oil objective. It shows the leaked radiation for LRM. . .  | 26 |
| 2.16. | Leakage radiation microscopy setup: (a) Real plane imaging and (b) Fourier plane imaging. . . . .  | 27 |
| 2.17. | Angular resolved reflectivity spectra in Kretschmann configuration. The plotted curves represent the ratio of p-polarized reflection for (a) bulk gold film (b) dealloyed nanoporous gold film (c) $30 \text{ nm}$ hexaporous gold and (d) $55 \text{ nm}$ hexaporous gold normalized with p-polarized glass background. The values of the angles of incidence in the glass are the same for all curves. A dip in reflection occurs, which shifts to shorter wavelengths with increasing angle of incidence (marked by the crosses). This indicates the resonant excitation of propagating surface plasmons. . . . . | 30 |

|   |    |
|---|----|
| 2.18. Angular resolved reflectivity spectra in Kretschmann configuration. The plotted curves represent the ratio of s-polarized reflection for (a) bulk gold film (b) dealloyed nanoporous gold film (c) 30 nm hexaporous gold and (d) 55 nm hexaporous gold normalized with s-polarized glass background. The values of the angles of incidence in the glass are the same for all curves. No change in dip position is observed . . . . .  | 31 |
| 2.19. Angular resolved reflectivity spectra in Kretschmann configuration. The plotted curves represent the ratio of p-polarized/s-polarized reflection for (a) bulk gold film (b) dealloyed nanoporous gold film (c) 30 nm hexaporous gold and (d) 55 nm hexaporous gold. The values of the angles of incidence in the glass are the same for all curves. A dip in reflection occurs, which shifts to shorter wavelengths with increasing angle of incidence (marked by the crosses). This indicates the resonant excitation of propagating surface plasmons. . . . . | 32 |
| 2.20. Dispersion relation of bulk gold, dealloyed nanoporous gold, hexaporous 30 nm and 55 nm gold. The symbols show the experimental data and the continuous lines show the theoretically calculated data using effective medium theories. (Bruggeman model for bulk and dealloyed nanoporous gold and Maxwell-Garnett model for hexaporous gold). . . . .   | 33 |
| 2.21. Theoretically calculated reflectivity by two different methods: (a) Reflectivity vs wavelength graph for 45°, 54°, 57° and 60° angles of incidence and (b) Reflectivity vs theta at the wavelength minima obtained from graph (a). . . . .  | 35 |
| 2.22. Dispersion relation of propagating surface plasmons at the bulk gold film (black) and the dealloyed nanoporous gold film (red). Experimentally determined data are shown as symbols (squares or triangles), while dispersion curves determined from theoretical calculations are shown as lines. (a) For the theoretical calculations, the dielectric constants from the ellipsometric measurements are used from figure 2.8. (b) The theoretical calculations are based on effective dielectric constants determined by the Bruggeman formula. . . . .         | 37 |
| 2.23. Leakage radiation microscopy a) Real plane image and its data (symbols) fitted with exponential decay profiles (solid line) b) Fourier plane image and its corresponding intensity profile (symbol) fit with a system of Lorentzian peaks (solid lines). . . . .  | 39 |
| 2.24. Leakage radiation microscopy: Real plane image magnified view, (a) The magnified view of the intensity profile image and the corresponding (b) magnified exponential decay profile of bulk gold revealing the long and short range oscillations $\Lambda_{l,s}$ . . . . .   | 42 |
| 2.25. Dispersion relation of dealloyed nanoporous gold from results of Kretschmann configuration (green squares), theoretical values (green line) and Leakage radiation microscopy (red point) value. The light line (41.83°) and (45°, 50°, 57° and 60°) angle lines are also shown. The gray area depicts the full width at half maxima of theoretically determined values of the dip. . . . .  | 43 |
| 2.26. Dispersion relation of bulk gold, dealloyed nanoporous gold, hexaporous 30 nm and 55 nm gold with LRM values (shown as crosses). It shows good correspondence between the two different experimental methods. . . . .   | 44 |
| 2.27. Sample detection through gold and PL setup . . . . .  | 46 |

|  |    |
|--|----|
| 2.28. PL for Si, Au on Si and dealloyed nanoporous Au on Si. . . . .   | 47 |
| 2.29. Theoretically calculated simple first order transmission data of emission of Si passing through Au (blue) or dealloyed Au (red) into air. . . . .  | 48 |
| 2.30. (a) Theoretical dispersion relation for semi infinite layer of dealloyed nanoporous gold on Si, glass and air (b) Experimental PL result for Si, Bulk Au on Si and dealloyed nanoporous Au on Si. This shows a comparison between theoretical dispersion relation of SPs on dealloyed nanoporous Au on Si (red) with the experimental PL of dealloyed nanoporous Gold on Si (red). . . . . | 48 |
| 3.1. Extinction cross sections of Au sphere with diameters: (a) 150 nm (b) 250 nm and (c) 350 nm. The spectra is further decomposed into contributions from absorption and scattering cross section with the dipole and quadrupole modes. . . . .  | 57 |
| 3.2. Hertz dipole and its influence at a point $(r, \theta, \phi)$ defined in spherical coordinate system. . . . .   | 57 |
| 3.3. Interacting dipoles activated by light polarized along y-axis ( $E_y$ ). The interacting antennas (a) stacked in y-direction and (b) stacked in x-direction are shown [88]. . . . .   | 60 |
| 3.4. Hertz dipole radiation directions, showing the spherical nature of far-field transverse electromagnetic waves. . . . .  | 61 |
| 3.5. Schematic of sample preparation on glass substrate. The process steps include the PMMA processing layer (all steps explained in corresponding text), e-beam lithography, Au deposition and lift off process to get nanoantennas. . . . .  | 64 |
| 3.6. Light optical microscope images for (a) the sample with four antenna area arrangements and (b) a specific area of $300 \mu m \times 300 \mu m$ zoomed in. The sample marked as C250S900 is for disk shaped antennas with diameter 250 nm and a quadratic periodicity of 900 nm. . . . .   | 64 |
| 3.7. SEM images of disk shaped nanoantennas with diameters of (a) 175 nm and (b) 250 nm arranged quadratically with a period of 900 nm. The dark stripes are charging effects in SEM. . . . .  | 66 |
| 3.8. SEM images of Au antennas with same disk diameter of 250 nm. They are arranged with a period of 900 nm in x-direction and a period of (a) 800 nm , (b) 900 nm and (c) 1000 nm in y- direction. The dark stripes are charging effects in SEM. . . . .  | 67 |
| 3.9. SEM images of rectangular Au nanoantennas with dimensions (a) $245 nm \times 200 nm$ , (b) $285 nm \times 172 nm$ and (c) $345 nm \times 140 nm$ . The dark stripes are charging effects in SEM. . . . .  | 68 |
| 3.10. Schematic of the setup used for transmission measurements of nanoantenna samples . . . . .   | 70 |

|  |    |
|--|----|
| 3.11. Transmission data of nanoantenna arrays of 250 nm diameter, arranged quadratically with periodicity of 900 nm. (a) The black solid line shows the transmission measurement. A Lorentzian curve is fit to the spectrum and is shown in green to depict the extinction spectrum of a single Au-particle without any other effects. The grating effects are introduced at 1350 nm and 955 nm due to first order (1,0) and 2nd order (1,1) grating diffraction. (b) A finite element calculation (COMSOL) of the extinction of the same configuration in a restricted spectral range is shown as red line while black solid line is still the experimental transmission measurement. . . . . | 71 |
| 3.12. The (1,0) and (1,1) diffraction edges and the corresponding distances between the interacting antenna directions. . . . .  | 71 |
| 3.13. Experimental transmission measurements of 250 nm disk arrays for changing angle of incidence of light on the sample from 0° to 10°. . . . .  | 74 |
| 3.14. The dispersion plot of experimental values (squares) received from figure 3.13. This is superimposed on calculations from a simple Maxwell-Garnett layer model (solid black lines). . . . .  | 74 |
| 3.15. (a)Transmission measurements of nanoantenna arrays with increasing disk diameter from 150 nm to 250 nm. (b) Lorentzian curve fitting shows red shift in the corresponding single particle resonance (red crosses) and enhancement of surface lattice resonance peak (blue crosses). . . . .  | 76 |
| 3.16. Transmission measurements of Set 2: antennas with constant periodicity of 900 nm in x-direction and varying periodicity of 800 nm, 900 nm and 1000 nm in y-direction. (a)Transmission measurement for light polarized along x-direction and its corresponding (b) schematic for dipole-dipole resonance parallel to $E_x$ and the net coupling effect is seen in y-direction. (c)Transmission measurement for light polarized along y-direction and its corresponding (d) schematic for dipole-dipole resonance parallel to $E_y$ and the net coupling effect is seen in x-direction. . . . .  | 78 |
| 3.17. Optical measurements of Set 3: (a) Schematic for changing aspect ratio of antennas, keeping volume constant. The light polarization direction is along the shorter side i.e. x-direction. (b) Transmission measurement data showing a slight blue shift of SLR with increasing aspect ratio. . . .   | 80 |
| 3.18. Optical measurements of Set 3: (a) Schematic for the light polarization direction is along the longer side i.e. y-direction. (b) Transmission measurement data showing red shift of SLR with increasing aspect ratio. . . .  | 80 |
| 3.19. Photoluminescence of PbS quantum dots embedded in PMMA and spin coated on glass substrate. . . . .   | 83 |
| 3.20. Schematic of the $\mu$ -PL setup. . . . .  | 83 |
| 3.21. (a)Transmission measurement and corresponding (b) PL spectra of samples comprising of varying antenna diameters from 175 nm to 250 nm. The increase in size gives a red shift in transmission and PL peak position . . .   | 84 |
| 3.22. Disk 250 nm with quadratic periodicity of 900 nm are pumped with laser (a) The experimental peak position of the PL curve obtained from area of sample with (red) and without (black) nanoantennas is plotted . The last point shows the breakdown power. (b) The corresponding light optical image of the burnt sample after breakdown. . . . .   | 85 |

|  |    |
|--|----|
| 3.23. Comparison of discs with diameter of $250\text{ nm}$ with rectangular antennas of increasing aspect ratio from $245\text{ nm} \times 200\text{ nm}$ to $285\text{ nm} \times 172\text{ nm}$ .<br>(a) Transmission measurement for $E_y$ polarization; (b) the corresponding PL spectra of all three samples. A red shift is observed with increasing aspect ratio and (c) Transmission measurement for $E_x$ polarization. . . . | 87 |
| A.1. 1D wave propagation geometry, with wave propagating along x-direction .   | 92 |

## List of Tables

|      |   |    |
|------|---|----|
| 2.1. | Effect of dealloying times on percentage of gold . . . . .  | 16 |
| 2.2. | Overview of all the continuous film samples that are used for study of propagating surface plasmons . . . . . | 22 |
| 2.3. | Values of $L_{spp}$ from LRM . . . . .  | 41 |
| 2.4. | Values of $(k_x)_r$ from LRM and theoretical calculations . . . . .   | 41 |
| 2.5. | Comparison of oscillation period with respect to Hohenau et al. [61] . . . .                                  | 42 |
| 3.1. | Overview of fabricated Au nanoantennas samples . . . . .  | 65 |
| 3.2. | Enhancement Ratio values of sample's with varying disk diameter . . . .                                       | 85 |

# Acknowledgment

First of all, I express my sincere gratitude to my supervisor Prof. Dr. Jörg Schilling, for giving me the opportunity to work on my thesis, in his group. He has been a constant pool of great ideas and has motivated me on each step to work ahead. He was at the forefront, to tackle each hurdle of this thesis work, and a constant support to bring together this thesis. I will be indebted to his patience and humor, which have rescued me from peril more times than I can recall.

I am very grateful to Dr. Christian Bohley for his constant supporting calculations and also guidance for theoretical calculations in this thesis.

I would like to thank Prof. Carsten Reinhart (LZH) for his kind support and for collaboration.

I am thankful to Dr. Vadim Talalaev, Dr. Paul-Tiberiu Miclea and (Dr.) Tobias Birr for their guidance and support in construction of setups during the course of thesis.

I thank Dipl.-Ing. Claudia Stehr, Dr. Frank Heyroth, Dr. Bodo Fuhrmann, Diplomphys. Sven Schlenker, Diplomphys. Frank Syrowatka and Dr. Martin Schade, plus other members of IZM staff for their kind cooperation in technical measurements and insightful discussions.

Thanks to Dr. Stefan Schweizer ( $\mu MD$ ), Dr. Benjamin Gesemann, Dr. Alexander Sprafke, Dr. Martin Otto and Ms. Daniela Schneevoigt for having fruitful discussion on experimental part of this thesis.

Special thanks to (Dr.) Peter Nolte for his constant support in experimentation, theory, acquisition, set-up, material etc.etc. My thesis would not be possible without a greathearted person like him.

I cannot be more indebted by the continuous and selfless work done by Dr. Kerstin Mitzschke, Dr. Annett Weltrowski and Ms. Doreen Rawald, to make my duration of thesis work at Halle easy and homely.

I would like to thank Andreas Cismak and Jan Schischka for their patience during FIB milling. I would also thank Fraunhofer Institute IWMH for the same.

I would also thank the International Max Planck Research School for Science and Technology of Nanostructures and the Federal Ministry for Education and Research for their financial support under project number FKZ:03Z2HN12, within the Centre for Innovation Competence SiLi-nano®.

Moreover, I would like to thank all my group members (especially Dr. Charlotte Pfau, Dr. Christian Passlick, Ms. Victoriia Rutckaia) and IMPRS colleagues (especially (Dr.) A. Davydov, (Dr.) A. Senichev (IRM) and (Dr.) F. Tandetzky) who were not just colleagues but friends, for creating a friendly and healthy environment to conduct my thesis work.

I thank all other people who made this thesis possible, if I might have forgotten to mention.

Last but not the least, I would like to thank my in-laws, for their constant support and encouragement. I would like to thank my husband (Dr. Vipin Chawla) for being a constant inspiration to my work. A person who has lifted my spirits during my blues and his constant love, and being there for me in sickness and in health. I would like to express my heartfelt gratitude to my parents Ms. Renu and Dr. S.K. Sardana. They are the light of my life, my rock and my safe place. This work was possible only because of their time, energy and motivation. My parents helped me learn to contextualize my dreams into reality and I thank them for their support at each step of my life.

# Curriculum vitae / Lebenslauf

## Personal Data

**Name:** Neha  
**Surname:** Sardana  
**Address:** H. No. 2189, Sector 22-C, Chandigarh, India  
**D.O.B. and Place:** 05 June 1986 in Lucknow, India  
**Marital Status:** Married

## Educational / Professional Details

| <b>Year</b>                   | <b>Degree/ Designation and Institution</b>  |
|-------------------------------|---|
| <b>July 2014 - ongoing</b>    | <b>Scientist B</b><br>Indian Institute of Nano Science and Technology, Mohali, India                                    |
| <b>April 2011 - June 2014</b> | <b>PhD Student</b><br>Dispersion Control of Surface Plasmons<br>IMPRS - ZIK SiLi Nano, MLU, Halle, Germany              |
| <b>2009 - 2011</b>            | <b>Masters</b><br>Materials and Manufacturing Engineering<br>Technical University of Denmark (DTU), Denmark             |
| <b>2005 - 2009</b>            | <b>B.Tech</b><br>Metallurgical and Materials Engineering<br>Indian Institute of Technology Roorkee (IIT Roorkee), India |
| <b>2003</b>                   | <b>HSC, AP Board (XII)</b><br>Ratna junior college, Hyderabad (A.P.), India   |
| <b>2001</b>                   | <b>SSC, CBSE (X)</b><br>Army School, Secunderabad (A.P.), India   |

Halle (Saale), den March 2015

(Neha Sardana)

## List of Publications

1. N. Sardana, T. Birr, S. Schlenker, C. Reinhardt and J. Schilling; Surface plasmons on ordered and bicontinuous spongy nanoporous gold; New Journal of Physics, 16 (6) (2014).
2. M. Schade, B. Fuhrmann, C. Bohley, S. Schlenker, N. Sardana, J. Schilling and H. S. Leipner; Regular arrays of Al nanoparticles for plasmonic applications; Journal of Applied Physics 115 (8) (2014).
3. N. Sardana, F. Heyroth and J. Schilling; Propagating surface plasmons on nanoporous gold; Journal of the Optical Society of America B 29 (7) (2012).
4. N. Sardana, V. Talalaev, C. Bohley, F. Heyroth, G.Schmidt and J. Schilling; Luminescence enhancement in the near infra-red due to nanodisk array resonances; submitted.

Halle (Saale), den March 2015

(Neha Sardana)

## **Eidesstattliche Erklärung**

Hiermit erkläre ich an Eides statt, dass ich die vorliegende Dissertation eigenständig und ausschließlich unter Zuhilfenahme der angegebenen Quellen und ohne unzulässige Hilfe Dritter angefertigt habe. Den benutzten Werken wörtlich oder inhaltlich entnommene Daten, Fakten und Konzepte sind unter Angabe der entsprechenden Quellen als solche gekennzeichnet. Diese Arbeit wurde bisher weder im In- noch Ausland in gleicher oder ähnlicher Form in einem anderen Prüfungsverfahren vorgelegt. Eine Anmeldung der Promotionsabsicht habe ich an keiner anderen Fakultät einer Universität oder Hochschule beantragt.

Halle (Saale), den März 2015

(Neha Sardana)